RECOVERY OF LITHIUM FROM AQUEOUS SYSTEM USING MANGANESE OXIDE ADSORBENT WITH DEVELOPED ELECTROSPUN MAT SUBSTRATE

A Thesis Submitted to
the Graduate School of Engineering and Sciences of
İzmir Institute of Technology
in Partial Fulfillment of the Requirements for the Degree of

MASTER OF SCIENCE

in Chemical Engineering

by
Berk AKGÜN

July 2023
İZMİR

We approve the thesis of **Berk AKGÜN**

Examining Committee Members:

Assoc. Prof. Dr. Özgenç EBİL
Department of Chemical Engineering, İzmir Institute of Technology

Prof. Dr. Ahmet Emin EROĞLU
Department of Chemistry, İzmir Institute of Technology

Asst. Prof. Çınar ÖNCEL
Department of Metallurgical and Materials Engineering, Muğla Sıtkı Koçman University

20 July 2023

Assoc. Prof. Dr. Özgenç EBİL
Supervisor, Department of Chemical Engineering
İzmir Institute of Technology

Prof. Dr. Mustafa M. DEMİR
Co-Supervisor, Department of Materials Science and Engineering
İzmir Institute of Technology

Prof. Dr. Erol ŞEKER
Head of the Department of Chemical Engineering

Prof. Dr. Mehtap EANES
Dean of the Graduate School of Engineering and Sciences

ACKNOWLEDGEMENTS

First and foremost, I am immensely grateful to my advisor, Assoc. Prof. Dr. Özgenç Ebil, and my co-advisor, Prof. Dr. Mustafa M. Demir, for their guidance, support, and invaluable expertise throughout the research process. Their insightful advice, constructive feedback, and unwavering encouragement have been instrumental in shaping the direction and quality of this thesis. Moreover, I would also like to extend my heartfelt appreciation to Prof. Dr. Mustafa M. Demir for his valuable input, mentorship, and assistance. His expertise and guidance have greatly enriched my research experience and contributed to the success of this thesis.

I am also thankful to the rest of my thesis defense committee, Prof. Dr. Ahmet Emin Eroğlu and Asst. Prof. Çınar Öncel for their valuable suggestions and comments.

Besides, I am grateful to the European Research and Innovation Program for funding this research through the "CRM-geothermal: Raw materials from geothermal fluids: occurrence, enrichment, extraction" project. Their financial support has provided the necessary resources and opportunities to carry out this study and achieve meaningful results.

I would especially like to thank Demir Lab Research group member Seyra Toprak for her support, assistance, and friendship throughout my master's studies.

I would also like to thank IZTECH Materials Research Center (MAM) for their contribution to the analysis of this thesis.

I would like to express my heartfelt gratitude to my beloved family, my father, Serkan Akgün, and my mother, Bahar Akgün, for their unwavering belief in me and their constant support and encouragement. They have always been by my side, accompanying me throughout this journey.

Last but not least, I would like to extend my special thanks to my beloved Gizem Oğuzlu, who has always been there for me, providing unwavering support and motivating me to give my best.

ABSTRACT

RECOVERY OF LITHIUM FROM AQUEOUS SYSTEM USING MANGANESE OXIDE ADSORBENT WITH DEVELOPED ELECTROSPUN MAT SUBSTRATE

Lithium is used in many fields due to its high energy density and unique electrochemical properties. Recently, there has been a strong increase in demand for lithium, so the extraction of lithium from natural water resources has become a remarkable research topic. One of the most effective methods of separating lithium from natural water sources is adsorption using lithium ion-sieve adsorbents. However, the powdered nature of the adsorbents makes them challenging to process. Recent studies have focused on developing adsorbents using different polymeric materials as substrates. In the thesis, as a new approach, flexible and free-standing polyurethane electrospun mat substrates were produced and combined with λ-MnO_2 to extract lithium from aqueous systems, and their lithium extraction performance was investigated.

After the fabricated mats and λ-MnO_2 powder were characterized, the deposition process was performed, and filtration studies were carried out in synthetic lithium solution. Optimum conditions for lithium extraction for a sample volume of 10 mL were found as an adsorbent amount of 200 mg, and 200 mg/L initial Li^+ concentration, and pH 12. In addition, lithium extraction performances have been improved by stacking mats and multi-stage filtration processes. Lithium extraction reached 76.6% when a 400 mg/L lithium solution and an 8-step filtration were used. Lithium extraction experiments were performed with salt lake brine containing high concentrations of various ions and showed that these ions reduced the lithium extraction. In the study, PU electrospun mats for λ-MnO_2 powder were found to be a promising substrate for lithium extraction from aqueous systems.

ÖZET

GELİŞTİRİLEN ELEKTROSPUN MAT SUBSTRAT İLE MANGAN OKSİT ADSORBAN KULLANARAK LİTYUMUN SULU SİSTEMDEN GERİ KAZANIMI

Lityum, yüksek enerji yoğunluğu ve benzersiz elektrokimyasal özellikleri nedeniyle birçok alanda kullanılmaktadır. Son zamanlarda, lityum talebinde güçlü bir artış olmuştur. Bu nedenle lityumun doğal su kaynaklarından çıkarılması dikkate değer bir araştırma konusu haline gelmiştir. Lityumu doğal su kaynaklarından ayırmanın en etkili yöntemlerinden biri lityum iyon elek adsorbanları kullanılan adsorpsiyondur. Bununla birlikte, adsorbanların toz halindeki yapıları, onları işlemeyi zor hale getirir. Son çalışmalar, substrat olarak farklı polimerik malzemeler kullanan adsorbanların geliştirilmesine odaklanmıştır. Tezde, yeni bir yaklaşım olarak, esnek ve serbest duran poliüretan elektrospun mat substratlar üretilip λ-MnO_2 ile birleştirilerek sulu sistemlerden lityum çıkarılmış ve lityum giderim performansları incelenmiştir.

Üretilen matlar ve λ-MnO_2 tozunun karakterizasyonu yapıldıktan sonra biriktirme işlemi gerçekleştirilmiş ve sentetik lityum çözeltisinde filtrasyon çalışmaları yapılmıştır. Hacmi 10 mL olan numune için lityum gideriminin optimum koşulları pH 12, adsorbent miktarı 200 mg ve başlangıç lityum konsantrasyonu 200 mg/L olarak belirlenmiştir. Ayrıca, matların istiflenmesi ve çok aşamalı filtrasyon işlemleri ile lityum giderme performansları iyileştirilmiştir. 400 mg/L lityum solüsyonu ve 8 aşamalı filtrasyon kullanıldığında lityum giderimi %76,6'ya ulaştı. Lityum giderme deneyleri, çeşitli iyonların yüksek konsantrasyonlarını içeren tuz gölü tuzlu suyu ile de gerçekleştirildi ve bu iyonların lityum giderimini azalttığı görüldü. Çalışmada, λ-MnO_2 tozu için PU elektrospun matların sulu sistemlerden lityum giderimi için umut verici bir substrat olduğu bulundu.

TABLE OF CONTENTS

LIST OF FIGURES

LIST OF TABLES

CHAPTER 1

INTRODUCTION

Lithium is a metal with a very high energy density by weight and high electrochemical potential besides being light and reactive.[1–3] Due to these desirable properties, it is used in various fields such as ceramic and glass, lubricating greases, air treatment, continuous casting mold, polymer production, and aluminum production, especially in Li-ion batteries.[4] In recent years, the demand for lithium has increased significantly due to the increasing applications of lithium-ion batteries in portable electronics, power tools, and electric vehicles. The demand for lithium is expected to grow exponentially, reaching 7.5 million tons per year by 2100 with the use of electric vehicles predicted to increase further in the future.[5] It is necessary to obtain lithium quickly and efficiently from lithium sources to meet this increasing demand. The extraction of lithium from lithium reserves by mining is both an environmentally harmful and unsustainable process, as the reserves will be depleted. For this reason, research on lithium recovery from natural water resources has increased in recent years.[6]

Various techniques such as evaporation, precipitation, solvent extraction, ion exchange, membrane, and adsorption are used for the recovery of lithium from natural water resources. Among these methods, adsorption is the most promising that has high selectivity for lithium besides being sustainable, cost-effective, technically feasible, and eco-friendly.[7,8] Lithium manganese oxide (LMO) type lithium ion-sieve (LIS) adsorbents are the most common with its high lithium selectivity and adsorption capacity. Spinel type λ-MnO_2 ion-sieve with certain crystal sites that could only permit lithium ions to place has been extensively studied in recovering lithium ions from natural water resources.[9]

Nanofibers are fibrous structured materials with diameters ranging from 1 to 1000 nanometers.[10] To fabricate nanofibers, both natural and synthetic polymers with high molecular weights that are wholly and readily soluble in specific solutions and conditions are used.[11] High porosity, high surface area, good permeability, high encapsulation efficiency, high chemical and thermal stability, controllable morphology, and advanced physical and mechanical properties of nanofibers make them unique materials.[12]

Therefore, nanofibers are used in various applications of drug delivery, water filtration, biomedical application, energy storage, and protective clothing. Nanofibers are produced by methods such as bicomponent extrusion, phase separation, template synthesis, drawing, melt-blowing, electrospinning, and centrifugal spinning. Electrospinning is the most propitious among these methods with its simplicity, flexibility, and cost-effectiveness.[13]

Electrospinning is a technique used to fabricate polymer fibers with diameters ranging between nanometers and micrometers. It has become a widely researched method in recent years with its ability to produce nanofibers with controllable pore structure and higher surface area, work with a wide variety of polymers, processability, and control the nanofiber composition.[14,15] Electrospun nanofibers were produced by applying a potential difference to a polymer solution or melt in a typical electrospinning procedure. Furthermore, nanofibers are not only made from synthetic and natural polymers but also nanoparticles loaded into polymers, in addition to metals and ceramics.[16] Some parameters affect the various properties and structures of the produced electrospun fiber. These are process, solution, and ambient parameters; applied voltage, tip to collector distance (TCD), flow rate, syringe diameter, concentration, molecular weight, viscosity, surface tension, relative humidity, and temperature.[17]

In the thesis, as a new approach, flexible and free-standing polyurethane (PU) electrospun mat substrates were fabricated and used by combining with λ-MnO_2 to extract lithium from aqueous systems. This study focused on lithium extraction from salt lake brine as part of a study aimed at lithium recovery from natural water sources. In the first step, structural characterization of λ-MnO_2 powder was carried out using XRD, SEM, and DLS methods, as well as structural characterization of PU electrospun mats using SEM, TGA, DSC, and AFM methods. Afterward, experiments were conducted using synthetic lithium solutions to examine the lithium extraction performance of PU electrospun mats with λ-MnO_2. Then, experiments were carried out using salt lake brine to see the lithium extraction performance of λ-MnO_2 and PU electrospun mats in natural brines.

CHAPTER 2

LITERATURE REVIEW

2.1. Electrospinning Process

The electrospinning process principally relies on the fundamental that electrostatic forces surmount the surface tension of the polymer solution droplet.[18] Electrospinning method is carried out at room temperature and atmospheric conditions. Horizontal and vertical are common electrospinning setups at present (Figure 2.1). The standard electrospinning setup includes a high-voltage power supply, a syringe pump, an electrically conducting spinneret, and a grounded collecting plate. An electric field is created between the needle tip and collector when a specific voltage is applied, starting the spinning process. Charges build up at the liquid's surface at the spinneret's tip while the pump maintains the solution's steady flow. After a while, the electrostatic repulsion becomes greater than the surface tension of the liquid droplet. Thus, the droplet forms a structure called Taylor cone. The charged liquid jet ejects toward the collector once the Taylor cone has formed. The solvent evaporates at the gap between the spinneret tip and collector, and the polymer remains at the collector.[19]

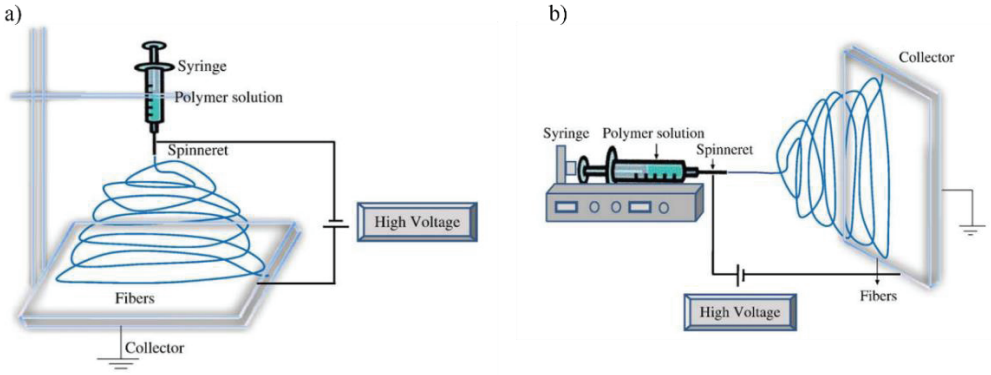

Figure 2.1. Illustrations of electrospinning setups; (a) vertical setup and (b) horizontal setup[20]

2.2. Electrospinning Parameters

Numerous variables, commonly categorized as solution, process, and environmental parameters, control the electrospinning process. Process parameters contain applied voltage, tip to collector distance (TCD), and feeding or flow rate while solution parameters contain concentration, viscosity, conductivity, molecular weight, and surface tension. Each of them has a substantial effect on the morphology and diameter of the produced electrospun mat. Therefore, nanofibers with desired fiber morphology and diameter can be obtained by appropriately adjusting these parameters.[21–24] Additionally, the humidity and temperature of the ambient that have a significant effect on the morphology and diameter of electrospun nanofibers are environmental parameters.[25–28]

2.2.1. Solution Parameters

2.2.1.1. Concentration

The electrospinning method is based on the uniaxial stretching of charged polymer jet that is influenced by the concentration of the solution. Therefore, a minimum solution concentration is necessary to produce fiber.[29] Polymer chains cannot form entanglements that provide the formation of fibers and polymer jets become droplets at low concentrations. Solutions with higher concentration are necessary to obtain stable polymer jets forming fibers. Consequently, the electrospun nanofibers cannot be formed at a lower concentration on a collector.[23,30,31] Moreover, beads that are defects formed at low concentrations disturb the unique characteristic of electrospun fibers and decline the surface area to volume ratio. When the solution concentration is increased, fibers without beads are observed.[23,32,33] Also, shapes of the electrospun fibers change with concentration. Straight, curly and wavy structures of fibers were observed in the study of Demir et al.[14] Several research have been conducted to investigate the relationship between solution concentration and average fiber diameter. Larger fiber diameters are obtained with increasing concentrations. This relationship between average fiber diameter

and concentration is explained as a power law relationship (Figure 2.2). Increasing concentration decelerates jet and fiber stretching, so thicker fibers are formed.[14,21,23,34]

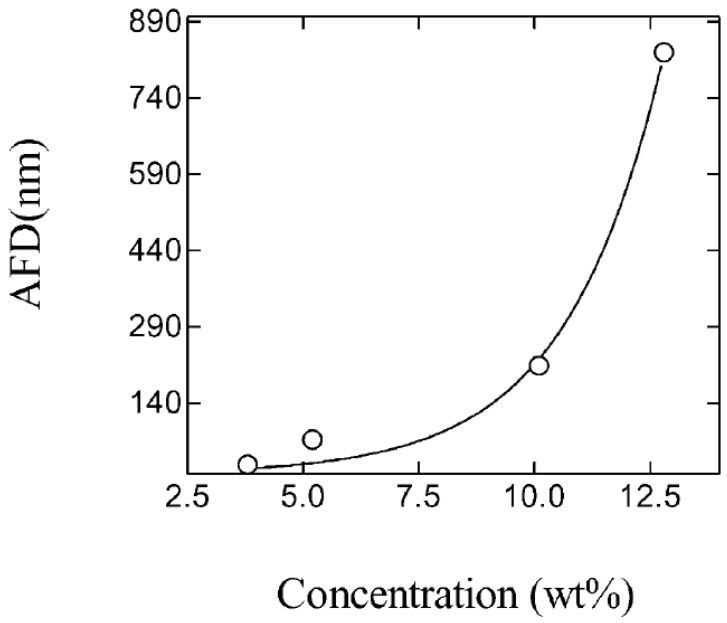

Figure 2.2. Power law relationship between average fiber diameter (AFD) and concentration[14]

2.2.1.2. Viscosity

The viscosity of solution has a significant impact on the fiber diameter and morphology. The concentration of the solution has a powerful relationship with the viscosity of the solution. Viscosity affects the size and morphology of fibers in the same way as concentration. Unceasing fiber formation cannot be obtained at low viscosities, while the ejection of polymer jets is challenging at high viscosities.[15,35] Surface tension is high when the viscosity of the solution is low. Due to the high surface tension, the solution jet that normally forms a nanofiber cannot keep its original shape at the tip and instead creates a small drop among the fibers. Thus, the bead appearance occurs in place of the formation of the fiber. Moreover, formed fibers have thinner diameters at low viscosities.[23,30] The number of beads declines, and the diameter of the fibers gets thicker

as the solution viscosity increases.[36] Also, fiber structure becomes more uniform with high viscosity.[35]

2.2.1.3. Conductivity

Since the viscous polymer solution is being stretched as a result of the charges repelled on its surface, one of the key characteristics in the electrospinning process is the solution conductivity. When the solution conductivity is higher, more charges can be made.[33] Conductivity of solution mostly depends on the polymer, solvent, and existence of ionizable salts.[15] Solution with poor conductivity prevents electrospinning since the surface of the droplet is not charged enough to create a Taylor cone. When the solution conductivity reaches a critical level, it forms a Taylor cone by increasing the charge on the surface of the droplet.[29] Moreover, stretching of the polymers happens strongly in high conductivity solutions, so the fiber diameter decreases and bead-free uniform fibers forms.[30,37]

2.2.1.4. Molecular Weight

Viscosity, surface tension, conductivity, and dielectric strength are rheological and electrical properties significantly influenced by the polymer's molecular weight.[38] The structure of electrospun fiber is affected by this essential solution parameter, and large molecular-weight polymer solutions are utilized in electrospinning because they provide the required viscosity for fiber formation.[15] For low molecular weight polymer solutions, the surface tension causes the jet's radius to decrease, resulting in the formation of a nanofiber between droplets, so the stable beads-on-string structure is formed. As a result, the number of beads and droplets decrease while the spacing between beads grow and the fiber diameter becomes more uniform as the molecular weight increase.[39]

2.2.1.5. Surface Tension

The surface tension appears to be more closely related to solvent compositions, while it is seldom affected by the concentration of the solution. Surface tensions may vary depending on the solvent. Due to the solution's high surface tension, the jets' instability and the formation of sprayed droplets typically hinder the electrospinning process. If all other parameters are held constant, surface tension typically dictates the upper and lower borders of the electrospinning process. Surface tension of a solution can affect the development of droplets, beads, and fibers. Solution with low surface tension can provide electrospinning to happen at a lower electric field. When the surface tension of the solution decreases, bead-free fibers are formed.[15,38,40]

2.2.2. Process Parameters

2.2.2.1. Tip to Collector Distance (TCD)

The morphology and diameter of fibers can be controlled by arranging tip to collector distance (TCD), which is another instrumental parameter of the electrospinning process. At this distance, solvent in polymer solution evaporates, and merely solid fiber remains on the collector. Deposition time and evaporation rate, which are directly related to TCD, affect the morphology and diameter of nanofibers. The optimal TCD provides solidification and complete extension of polymer jets that lead to the production of firm fibers.[21,29] Several studies were made to see the effect of the TCD on fiber size, and these studies resulted in fiber diameter decreases as the TCD increases. Moreover, beads formation and defects in fiber morphology are observed with the TCD decline.[17,21,37,41] Contrary to these studies, it was observed that TCD has no significant effect on fiber size in some studies.[23,36,42]

2.2.2.2. Applied Voltage

Applied voltage to the polymer solution is an essential parameter in the electrospinning process. Fiber creation doesn't happen until the threshold voltage is reached. This voltage produces the required charges on the solution and the electric field, which starts the electrospinning process. The threshold voltage has a proportional relationship with the concentration of the solution. Higher electrical forces are needed to surmount the surface tension and the viscoelastic force stretching the fiber as the concentration rises.[14] There is some disagreement over how applied voltage behaves during the electrospinning process. It was suggested that thin-diameter fibers and a few beads form at low voltages while more beaded fibers form with increasing applied voltage. Moreover, a further increase in voltage results in obtaining larger fiber diameters.[35] Other studies showed that fiber diameters get thinner as the applied voltage increases. Electrostatic and repulsive forces increase when the high voltage is applied, which causes enhancement of the tensile force on the polymer jet, so fiber diameter decreases.[17,21,22]

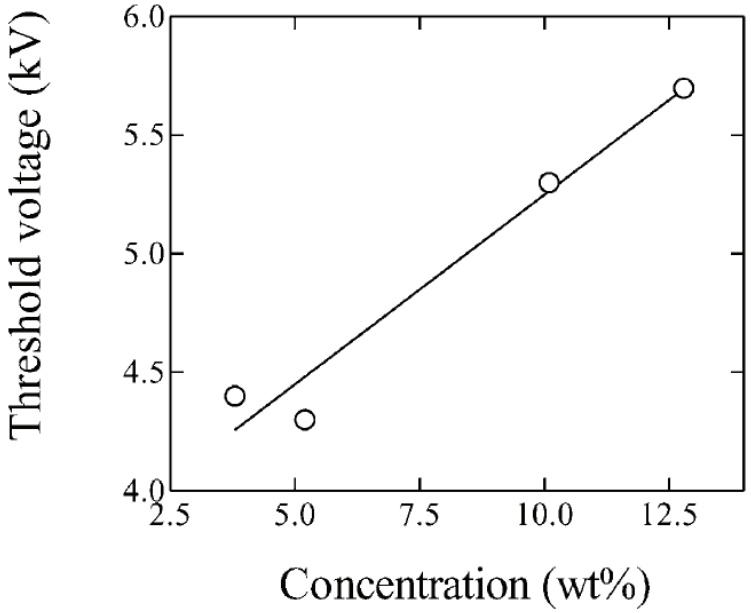

Figure 2.3. Relationship between threshold voltage and concentration[14]

2.2.2.3. Flow Rate

The velocity of the polymer jet and the transfer rate of fiber are affected by flow rate of the solution leaving syringe. Electrospun fiber's morphology and diameter change with this crucial parameter. As the solvent will have more time to evaporate, a lower flow rate is suitable.[43] The optimum flow rate should be determined based on the polymer system. Beads may occur due to the lack of a sufficient drying period before reaching the collector if the flow rate increases beyond a certain point. Moreover, an increase in flow rate results in an excessive amount of polymer being deposited on the collector quickly, which leads to the conjunction of fibers.[43–45] Some researchers have examined the effect of flow rate on fiber size. With an increase in polymer flow rate, the fiber diameter enhances, and the morphological structure may also change barely.[35,36]

2.2.3. Environmental Parameters

2.2.3.1. Temperature and Humidity

There are environmental parameters in addition to solution and processing parameters, such as humidity and temperature. Studies have been done to look at how environmental parameters affect the structure of fibers. Interestingly, the temperature has the same effects on the structure of the resulting nanofibers at lower and higher temperatures than moderate temperatures. The first effect is a decline in the evaporation rate of solvent with lower temperatures. As a result, the polymer jet continues to lengthen and harden over a longer period of time, and fibers with thin diameters are formed. Secondly, the rigidity of electrospun fibers is influenced by temperature. Higher temperatures allow the polymer chains more ability to move, which lowers the viscosity of the fluid. Viscous forces and surface tension of the polymer solution resist the stretching of the polymer jet. When the solution viscosity decreases at higher temperatures, stretching resistance is reduced. Thus, thinner fibers are formed because of higher stretching rates.[27,28]

Humidity manages the solidification of the polymer jet that affects the structure of the electrospun fibers. Nevertheless, it also depends on the chemical structure of the polymer. Fiber diameters get thinner with increasing humidity, and after a further increase, bead formation is observed. Moreover, tiny pores occur on the fibers' surface by increasing humidity, and pores merge with a further rise of humidity.[46,47] The evaporation rate of the solvent enhances at low humidity so that the solvent may evaporate at the tip of the spinneret. Therefore, the polymer remains at the tip of the spinneret and clogs it.[48]

2.3. Role of Solvent in Electrospinning

Dissolving polymer entirely in an appropriate solvent is the first and most crucial part of electrospinning, and it has a substantial impact on its spinnability. Moderate boiling point is a property that a solvent need to have because the volatility of a solvent can be estimated from its boiling point.[15] Volatile solvents are usually desirable because of their high evaporation rates that provide evaporation of solvent and formation of fibers on the collector. However, solvents with very low boiling points are not preferred because of the drying effect on the polymer jet at the needle. It results in clogging at the tip of the needle and prevents the process. On the other hand, less volatile solvents are not favored since they cannot dry completely during the flight of the polymer jet.[29] Bead formation on fibers is observed as a result of the deposition of nanofibers containing solvent on the collector.[49] Additionally, the solvent is crucial in producing porous nanofibers when the polymer is dissolved in two solvents. Phase separation occurs because of the various evaporation rates of the solvents that provide the production of porous electrospun nanofibers.[50] Porous electrospun nanofibers were obtained by differing the compositions of solvents dimethylformamide (DMF) and tetrahydrofuran (THF) in studies made.[30,36] Conductivity and dipole moment of the solvent are essential besides the volatility of the solvent. Ethyl acetate, DMF, THF, methyl ethyl ketone, and 1,2-dichloroethane were found suitable for the electrospinning process, among the other various solvents because of their conductivity and dipole moment values.[51]

2.4. Polymers Used in Electrospinning

Various polymers can be utilized in electrospinning to create fine nanofibers that can be employed for many purposes. Natural polymers, synthetic polymers, and mixtures of both have been used in many studies depending on the area of use.[15] In some studies, proteins and polysaccharides have also been used in electrospinning.[52,53]

Various polymers have recently been used to produce nanofiber electrospun in many biomedical fields. Natural polymers typically reveal better biodegradability, biocompatibility and low antigenicity than synthetic polymers in biomedical applications. Collagen, chitosan, gelatin, silk fibroin, cellulose, alginate, hyaluronic acid, and fibrinogen are examples of common natural polymers.[15] In tissue engineering, collagen, a well-known biopolymer, is frequently used as a component of skin substitute materials and wound dressings. This is explained by its unique biological and physical characteristics, which include actions on fibroblasts and keratinocytes that promote proliferation and hemostasis.[54] It was successfully electrospun from a variety of fluoroalcohol-based solvents, including ethanol in water solutions and 1,1,1,3,3,3-hexafluoro-2-propanol (HFP) and 2,2,2-trifluoroethanol (TFE).[55] However, fluoroalcohol accelerates native structure denaturation and lowers the denaturation temperature of non-collagenous proteins. Thus, a loss of 45% of collagen has been observed.[56]

Synthetic polymers provide numerous benefits compared to natural polymers since they can reveal better mechanical properties and spinnability. Furthermore, they readily degrade into a wider variety of solvents. Electrospinning has been used to create nanofiber electrospun from a variety of synthetic polymers, including polyacrylonitrile (PAN), polycaprolactone (PCL), polyvinyl alcohol (PVA), polyethylene oxide (PEO), poly(lactic acid) (PLA), poly(glycolic acid) (PGA), polyurethane (PU) and polystyrene (PS).[54] PVA is commonly used in producing fibers due to its excellent physical and mechanical properties, such as high tensile strength, flexibility, and biocompatibility. The optimal electrospinning parameters for fabricating the most uniform PVA fiber mats depend on the specific properties of the PVA solution used.[42] PS is made from monomer styrene and is commonly used in various applications. PS nanofibers can be electrospun straight from single or multiple solvent solutions. The type of solvent solution utilized has an impact on the morphology of the electrospun fibers, with certain solvents producing grooves that were more obvious than others.[32]

Electrospinning polyurethane solutions can successfully produce ultra-fine elastic fibers with submicron diameters, and fiber diameter increases as the third power of solution concentration, with viscosity and temperature being the dominant factors among other solution properties.[14] Due to its chemical stability, mass transport, superior mechanical capabilities, and outstanding nanofiber-forming characteristics, polyurethane is frequently used to construct a nanofiber.[57] Most polyurethanes share the urethane group, but unlike thermosetting polymers, which melt when heated, thermoplastic polyurethanes (TPUs) are simple to employ in manufacturing processes (Figure 2.4).

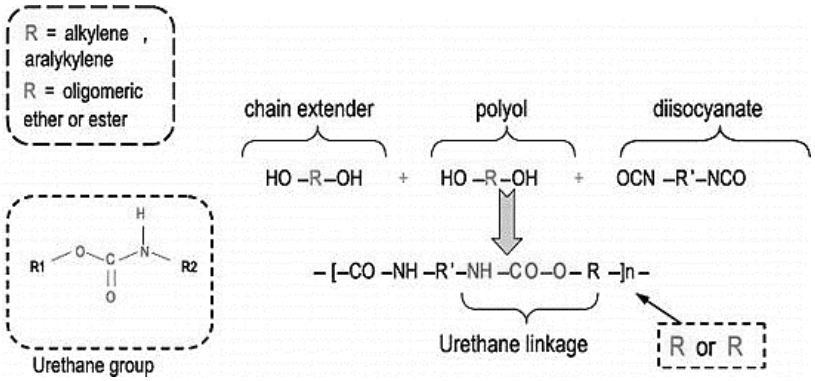

Figure 2.4. Thermoplastic Polyurethane[37]

The main difference between PU and TPU is that TPU is more elastic and has better abrasion resistance than PU.[37] One of the segmented block copolymers made up of both hard and soft segment blocks is the TPU. While the hard segments are formed from short-chain diols, the soft-segment blocks are created using long-chain polyester or polyether polyols. The distinctive characteristics of linear TPUs can be assigned to their elongated molecular structure.[58]

2.5. Applications of Electrospun Mats

Electrospinning is a polymer processing technique that has been employed for producing and arranging nanofibers of various materials, broadening the scope of

potential uses in fields like biomedical, environmental protection, nano sensors, electronics/optics, and protective clothing. Electrospun nanofibers have a wide range of applications in the biomedical field including use as tissue engineering scaffolds, wound healing, drug delivery systems, filters, affinity membranes, enzyme immobilization, healthcare, biotechnology, environmental engineering, defense and security, energy storage and generation.[15] Several patents have been granted in the US for fabrication methods and techniques used in various application fields. Based on the analysis of the patent data, it appears that around two-thirds of all electrospinning applications are in the medical field. Of the remaining patents, half focus on filtration applications, with the other half covering a variety of other uses.[59]

Electrospun nanofibers are also used in filtration applications in addition to their many prospective uses in the biological field. Heavy metal ions that are harmful to the environment and health and valuable ions can be found in the water resources due to many industrial processes. According to several researchers, electrospun nanofibers outperform conventional materials in surface-to-length ratio and interconnected porosity in removing metal ions from water.[60–62] Besides its sole usage, electrospun nanofibers can be combined with adsorbent nanoparticles to enhance the adsorption performance.[63]

Electrospun nanofibers are widely used as substrates in various applications due to their high surface area, small fiber diameter, porous structure, mechanical properties, and versatility. Polyvinylidene fluoride (PVDF) electrospun nanofibers used as substrate to improve mechanical properties of forward osmosis membranes. Moreover, using PVDF enhanced the performance of forward osmosis.[64] Polyurethane nanofiber substrates improved characteristics such as waterproofness and breathability when used for the electrospun nanofiber web-layered fabric systems.[65] The PAN nanofiber was used as a substrate for its high surface area to volume ratio, allowing thin and defect-free layers deposition. PAN substrate provides a gradually structured nanofiber membrane that can be used as a substrate for fabricating high-performance composite membranes.[66]

2.6. Lithium Supply and Demand

Lithium, one of the most abundant elements on earth, is a light and reactive metal that plays a crucial role as the main constituent in lithium-ion batteries, one of the most

promising types of high-energy-density storage. Moreover, its high electrode potential makes it electrochemically active and has a higher specific heat capacity than other solid elements.[4,67] Due to these critical features, it is used in many application areas, especially lithium-ion batteries. Recently, electric vehicles have been getting more attention to decrease the hazardous effects of fossil fuel vehicles causing global warming. The best option for electrical storage batteries for electric vehicles is rechargeable lithium-ion batteries, which offer more charging cycles, a less memory effect, and a great energy density relative to other types of batteries. Thus, lithium is widely used to produce rechargeable lithium-ion batteries to store electrical energy. Consequently, there is a crucial increase in demand for lithium.[68] Nations will need about 60 times more lithium for electric vehicle batteries and energy storage by 2050, due to the estimation of the European Commission. Therefore, lithium was listed for the first time as critical raw material with the decision of the European Commission in 2020.[69]

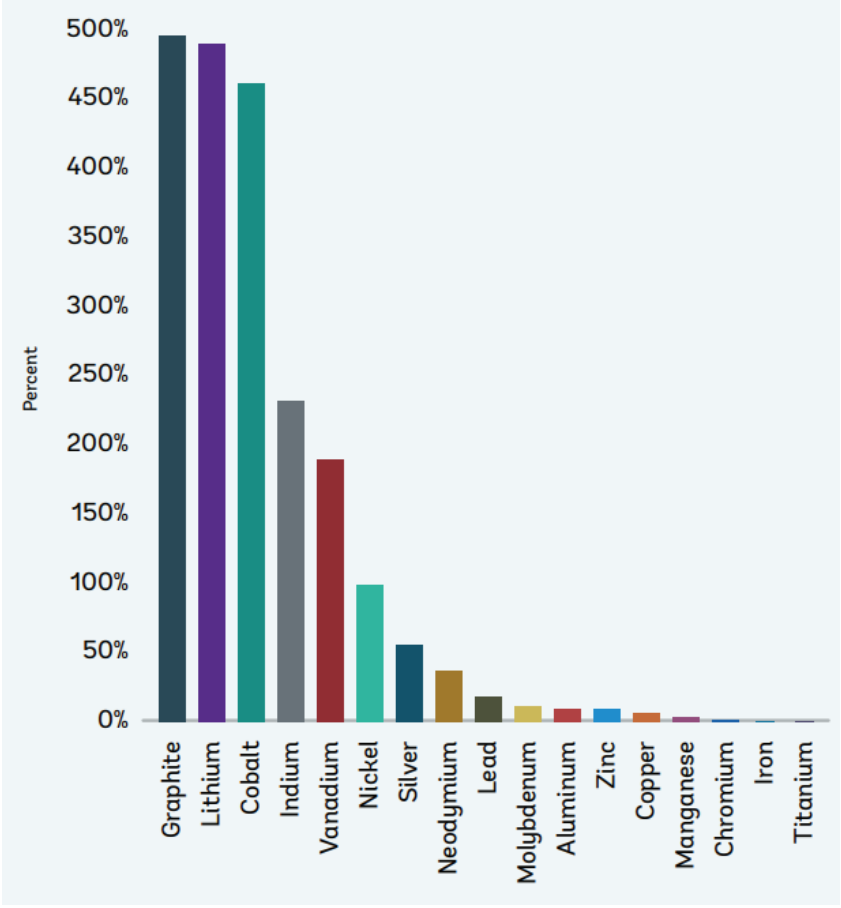

Figure 2.5. 2050 annual demand from energy technologies as percentage of 2018 production[70]

The two main minerals used commercially for lithium extraction are lithium carbonate and lithium hydroxide. The demand for these products increased by around 30% in the years 2020–2021, but prices extraordinarily increased by about 300%.[6] Rising demand would cause lithium production to rise from 447 thousand tons lithium carbonate equivalent (LCE) in 2018 to over 2 million tons (LCE) in 2050, constituting an increase of 488% (Figure 2.5).[70] Another study forecasts that the global demand for lithium is expected to increase by a factor of 5 due to the growing electric vehicle market over the next decade. This will result in a surge from the current production level of 316 thousand tons LCE to 1790 thousand tons LCE in 2030.[1]

2.7. Application Areas of Lithium

Lithium is used in a variety of applications across different sectors due to its special characteristics and adaptability. The United States Geological Survey evaluated the global market size of lithium for these various industries (Figure 2.6).

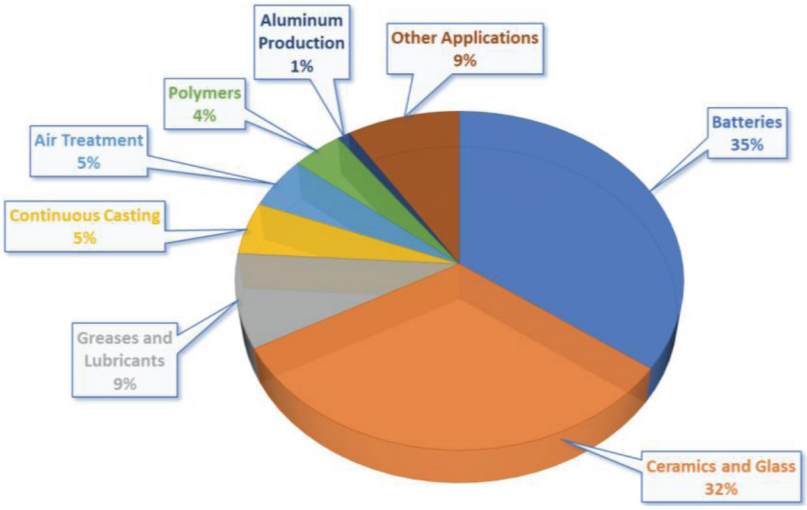

Figure 2.6. Distribution of global lithium end-uses for various applications[2]

Rechargeable lithium-ion batteries, which power many gadgets from smartphones and laptops to electric vehicles, are one of its main applications.[2] A cathode, an anode, a

separator, an electrolyte, and two current collectors make up a conventional lithium-ion battery. $LiCoO_2$ (LCO), $LiMn_2O_4$ (LMO), $LiFePO_4$ (LFP), and $LiNiMnCoO_2$ (NMC) are generally used as cathodes, while graphite is used as anode. The battery is charged and discharged with the generation of electrons and current flow formation of lithium ions between the cathode and anode. Electrolytes, comprising $LiPF_6$, $LiBF_4$, and $LiClO_4$ in solvents, provide lithium ions to move by creating conductive pathways.[71]

Lithium-ion batteries are the favored technology for powering EVs and other portable electronic devices due to their superior cycle life and longer life, high specific energy (230 Wh/kg), high power density (12 kW/kg), and great charging and discharging efficiency.[72] The number of devices using lithium-ion batteries is increasing continuously. It is estimated that the market share of electric vehicles will exceed the percentage of vehicles using fossil fuels. More lithium-ion batteries will need to be produced for electric cars as well as renewable energy generation systems. Consequently, the demand for lithium-ion batteries is expected to rise dramatically in the coming years.[9]

Glass and ceramics, which had a share of 32% in total production in 2016, are the second largest sector in the lithium market.[2] Lithium is known to improve various properties of glass and ceramic products; for example, it reduces shrinkage while increasing the mechanical strength of thin ceramics. Moreover, it can lower heating temperatures that require lithium, thereby shortening cycle times and increasing production. In the production process of ceramic glazes and porcelain enamels, lithium is mainly used as Li_2CO_3, often used as a flow agent to coat the ceramic body.[73] In the glass industry, lithium improves color fastness, gloss, and resistance. In addition, spodumene concentrate can also be used as a fluxing agent in glazes, often in combination with other lithium minerals such as lepidolite, amblygonite, and petalite. The lithia (Li_2O) content of 4.0% to 7.25% lowers the melting temperature and thus saves energy in the production process. Manufactured lithia glazes are also known to have higher chemical resistance, less air trapping, and lower viscosity, therefore being less rejected products.[74]

Greases and lubricants are another application area of lithium. In producing greases, significant amounts of lithium hydroxide are used. Lithium hydroxide reacts with 12-hydroxy stearic or other fatty acids. Lithium stearate extends outwardly in interlocked spirals while the lithium binds to the metal, and the long-chain multi-hydroxylated end of the stearate molecule forms a matrix or spongy gel lubricant that holds the petroleum-based oil and supports the wear surface.[75] Lithium-based greases have the advantage of

maintaining lubricating properties over a wide temperature range and providing good water resistance.[74]

Lithium is also used in many sectors besides lithium-ion batteries, ceramics, and grease. In continuous casting, Li_2O is used as a melting agent to lower the melt viscosity. As another application, in air treatment, lithium bromide is used as an absorbent in industrial absorption coolers that do not contain chlorofluorocarbons.[74] Inorganic styrene-butadiene rubber and polybutadiene rubber are produced using polymerization processes, and the organic lithium compound n-butyl lithium is utilized as an initiator. Li_2CO_3 is used as an electrolyte additive in aluminum production. It lowers the melting point while enhancing the bath's electrical conductivity.[73]

2.8. Lithium Resources

Lithium resources are divided into two separate categories, solid and liquid resources. Solid resources are mineral ores and clays, and liquid resources are brines like salt lakes, seawater, and geothermal.

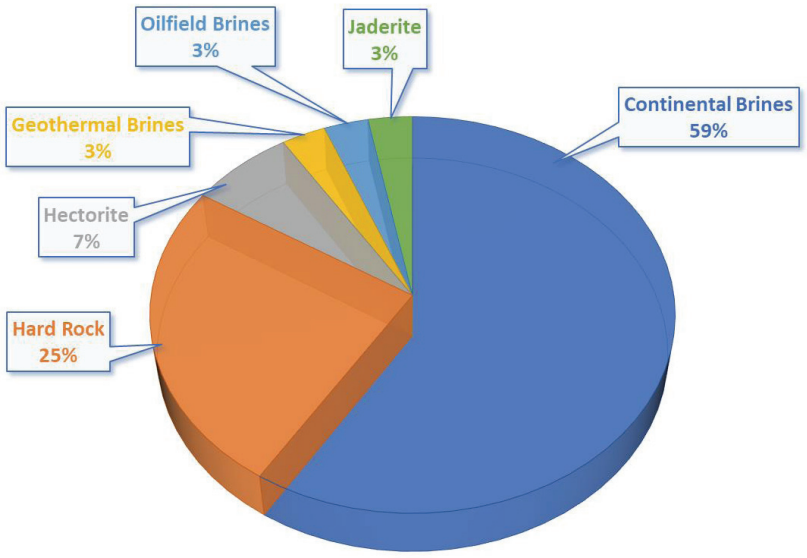

Figure 2.7. Distribution of lithium resources[2]

The distribution of lithium across different resources is depicted in the Figure 2.7. The majority (59%) of lithium resources are found in continental brines, followed by hard rock (25%) hectorite (7%), geothermal brines (3%), oilfield brines (3%), and jaderite (3%).[2] According to ongoing research around the world, lithium resources have increased significantly, and over 89 million tons have been discovered by 2021. On the other hand, production increased by 21% in 2021 and reached approximately 100,000 tons.[76]

2.8.1. Mineral Ores and Clays

Only a few of the approximately 131 known lithium minerals have economic importance and have been examined to utilize their lithium values. These minerals are eucryptite, lepidolite, spodumene, jaderite, hectorite, amblygonite, petalite, and zinnwaldite, with various lithium content (Table 2.1).[77] Australia produces the most lithium from minerals worldwide, primarily from spodumene.[75] Lepidolite was formerly employed as a source of lithium but has since lost its significance because of its high fluorine level. Petalite is frequently used in making glass due to its high iron content.[78] Mining recovery rates generally range from 60% to 70%, but a specific process is required to convert the produced lithium into a marketable form.[77]

Table 2.1. Widely used lithium-containing minerals[77]

Mineral	Lithium Content (%)
Eucryptite	5.51
Lepidolite	3.58
Spodumene	3.73
Jaderite	0.53
Hectorite	3.16
Amblygonite	3.44
Petalite	2.09
Zinnwaldite	1.59

As a result of the analysis by various organizations, it is predicted that some critical elements will potentially face rapidly increasing demand and therefore increasing prices in the coming decades. This rapid increase in demand may be adequately and sustainably met by investigating alternative sources for resource recovery. Alternatively, the second primary reason for the increased interest in extracting minerals from brines is the environmental danger it poses to all living things as a result of traditional mining applications. A study made in 2017 found that mining companies dump almost 2 billion pounds of toxic waste into water supplies, revealing a severe threat to all living things.[6] Therefore, it is clear that traditional land-based mining should be minimized over time to maintain a cleaner environment in the long term.

2.8.2. Brines

A promising resource for reclaiming rich minerals that can meet growing industrial demand and reduce environmental deterioration is the abundance of brine reservoirs around the world. Due to their high concentrations, salt lakes and geothermal brine are presently important sources for the extraction of several minerals.[6] Between 50 and 75 percent of the world's lithium production comes from brine resources.[79] Brines are foreseen to become a more significant resource source of lithium than minerals (Figure 2.8).

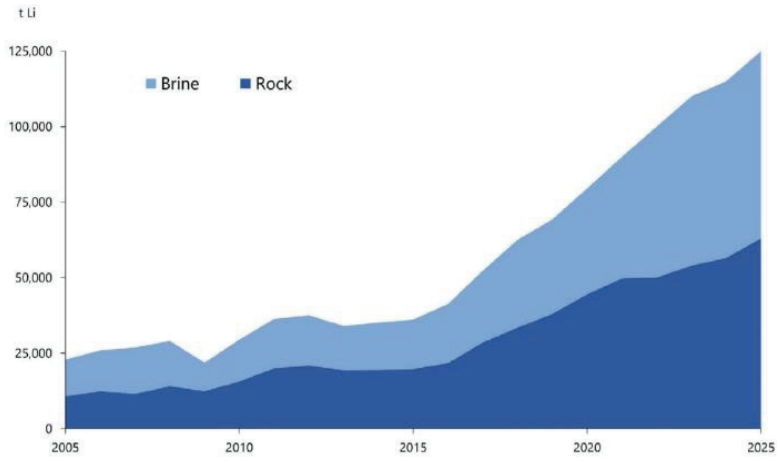

Figure 2.8. Global lithium production by resources[1]

Brine extraction would be more eco-friendly and economically viable than extraction from ores. The major resources of lithium-containing brine worldwide and their lithium composition are listed in Table 2.2.

Table 2.2. Lithium concentrations in brines[3,83]

Deposit Name	Country	Lithium (wt%)
Salar de Atacama	Chile	0.157
Maricunga	Chile	0.092
Uyuni	Bolivia	0.0321
Cauchari	Argentina	0.062
Olaroz	Argentina	0.09
Hombre Muerto	Argentina	0.062
Rincon	Argentina	0.034
Silver Peak	USA	0.03
Great Salt Lake	USA	0.006
Bonneville	USA	0.0057
Salton Sea	USA	0.022
Searles Lake	USA	0.0083
Smackover	USA	0.038
Clayton Valley	USA	0.0163
East Taijinar	China	0.085
Fox Greek	Canada	0.01
Ayvacık Tuzla	Türkiye	0.0038
Ezine Kestanbol	Türkiye	0.0012
Lake Tuz	Türkiye	0.0303
Çan Karaılıca	Türkiye	0.0001

While the lithium concentration of brines varies between 100 – 1000 mg/L, the typical lithium content in seawater is only 0.17 mg/L. Therefore, salt lake and geothermal brines are the most promising water sources for industrial-scale lithium extraction.[80] However, in addition to Li^+, salt lake brines typically contain great amount of Mg^{2+} and other ions (Na^+, Ca^{2+} and K^+). Lithium must be separated from other co-occurring ions in

salt lake brines to produce high-purity lithium products. Li^+ and Mg^{2+} are more challenging to separate than other ions because of their similar chemical makeup and ionic radius.[81] Li^+ has an ionic radius of 0.79 Å, while Mg^{2+} has an ionic radius of 0.72 Å [1]. It is known that brines with a low Mg^{2+}/Li^+ ratio make it simpler to collect lithium due to their relatively high lithium content. In brines with a high Mg^{2+}/Li^+ ratio, effective Mg^{2+} and Li^+ separation requires a more expensive, rigorous method . Therefore, research continues to determine how to recover lithium from salt lake brines with high Mg^{2+}/Li^+ ratios.[82]

2.9. Lithium Recovery from Brines

Lithium extraction from brines has been the subject of in-depth study, and a number of methods, including evaporation, precipitation, solvent extraction, ion exchange, membrane, and adsorption, have been created and thoroughly investigated.[84] To extract lithium from brine with a high Mg^{2+}/Li^+ ratio and low Li^+ concentration, the adsorption method offers important environmental and economic benefits, among other techniques. This process provides a high recovery rate, high selectivity to lithium, ease of operation, and low energy consumption, using inorganic adsorbents with a high affinity toward lithium ions.[8]

2.9.1. Evaporation

Evaporation is one of the widely used techniques in the industry standard for lithium recovery from salt lake brines and is also accepted for seawater.[85] This is usually achieved by pumping the brine into large evaporation ponds and evaporating the brine with sunlight and wind, enriching the concentration of lithium and other dissolved elements (Figure 2.9). As the concentration increases, the less soluble salts halite (NaCl), calcium sulfate ($CaSO_4 \cdot 2H_2O$), carbonates ((Ca, Mg, Fe)CO_3), carnallite ($KCl \cdot MgCl_2 \cdot 6H_2O$) or biscophyte ($MgCl_2 \cdot 6H_2O$) precipitation takes place.[86] The final brine, rich in lithium chloride, is then sent to the treatment plants once the salts have been

collected. Finally, precipitation of high-purity lithium carbonate (99.5–99.9%) takes place with the addition of sodium carbonate.[87] Commercial-grade lithium carbonate, the primary raw material for producing desired lithium compounds or lithium metal, is obtained by additional chemical processes.[6] The total production cost of the simple and inexpensive evaporation process is 2,000–5,700 US$/t lithium carbonate equivalent.[5] However, the evaporation method is time-consuming, it cannot be applied in all geographies depending on the climates, and the changing brine composition is a major factor in this process.[6] On the other hand, this process, which leads to high consumption of fresh water, causes drought danger to the areas where the facilities are located in Chile.[88] The researchers focus on "non-evaporative" technologies for lithium extraction due to these drawbacks of the evaporation process.

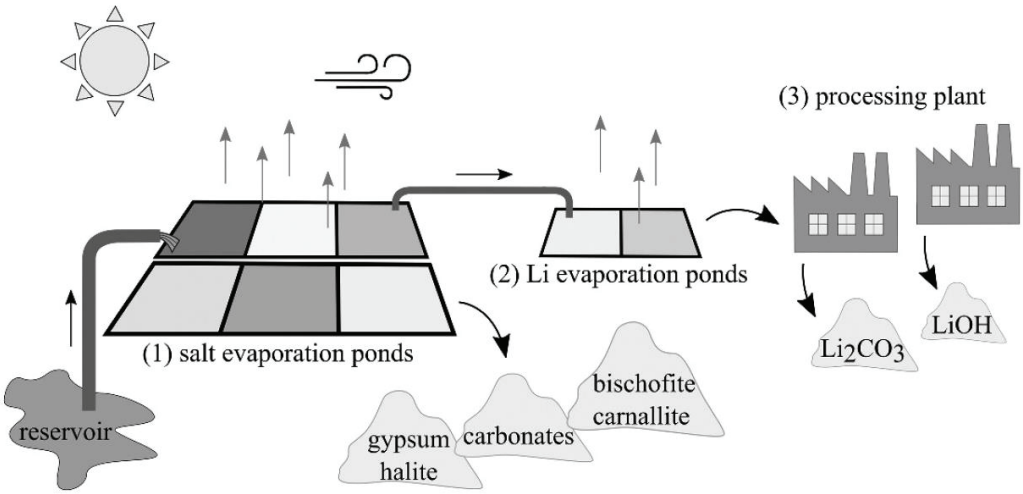

Figure 2.9. Evaporation process of brines[86]

2.9.2. Precipitation

Methods based on precipitation are often straightforward and favored in the industry since they are inexpensive. The process of extraction through precipitation relies on diminishing the solubility of dissolved species, leading to the formation of chemical compounds. Factors such as pH, temperature, redox, impurities, and concentration of precipitant affect precipitation. Several precipitation methods are available for natural

brine systems, such as carbonate and aluminate precipitation and borate and phosphate co-precipitation.[84] Epstein et al.[89] reported the first successful experiments using aluminum chloride at the ideal pH and temperature to precipitate lithium as lithium aluminate from dead sea brine. Precipitation of lithium also as lithium carbonate in brine, was reported in the work of An et al.[85] using a multistage precipitation process.

Researchers have suggested several precipitation strategies depending on the relative Mg^{2+}/Li^{+} ratio in brine since the co-precipitation of magnesium is the main problem with lithium precipitation.[6] In brines with a low Mg^{2+}/Li^{+} ratio (less than 6), "carbonate precipitation" is commonly used. In this process, magnesium is precipitated by calcium oxide first, and then sodium carbonate is added to precipitate lithium as lithium carbonate.[90] "Aluminate precipitation" and "Mg precipitation" methods are used to recover lithium in brine sources, which have a high Mg^{2+}/Li^{+} ratio, usually naturally occurring. In the aluminate precipitation method, aluminum hydroxide is formed by adding aluminum chloride and sodium hydroxide, and thus lithium selectively precipitates as lithium aluminate. This more environmentally sustainable method enabled the efficient recovery of lithium from high Mg^{2+}/Li^{+} brines.[91,92] Although precipitation is one of the oldest approaches used to recover lithium from brine sources, it is still favored due to its scalability and inexpensiveness. However, the precipitation process can add additional chemicals or reagents to the brine and cause environmental pollution if these are not appropriately managed. The disposal of precipitated solids or by-products can also present challenges. Therefore, crucial attempts must be made to increase energy efficiency and minimize the environmental effect due to the use of chemical reagents.[6]

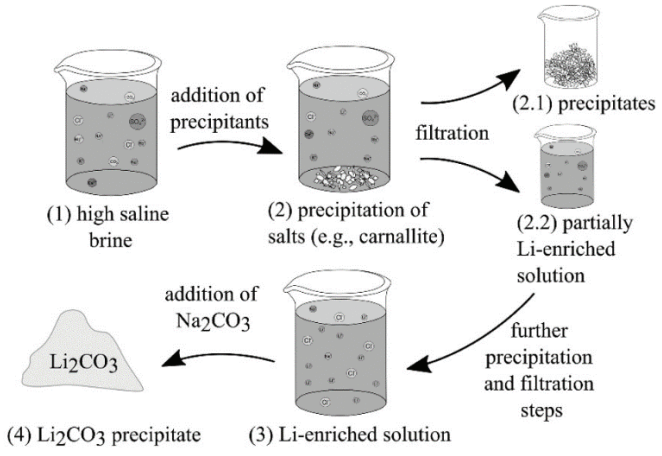

Figure 2.10. Precipitation process for brines[86]

2.9.3. Solvent Extraction

Another practical method for recovering lithium from brine is solvent extraction, often known as "liquid-liquid extraction" or "chemical extraction," chosen due to its low cost and high product yield. Through organic solvents, considerable volumes of lithium chloride can be dissolved, while undesirable salts can be removed in a targeted manner.[92] The most commonly used and extensively studied extractant in the solvent extraction method to extract lithium selectively is tributyl phosphate (TBP). For instance, it has been discovered that an extraction technique using TBP/kerosene and $FeCl_3$ is effective for recovering lithium from brine sources with a high Mg^{2+}/Li^{+} ratio. In this system, TBP serves as an extractant of neutral organophosphorus, and kerosene serves as a diluent. In order to recover lithium, $FeCl_3$ aids in the co-extraction procedure.[93] According to Harvianto et al.[94], an extraction technique based on thenoyltrifluoroacetone, trioctylphosphine oxide, and kerosene was utilized to extract lithium from seawater and concentrated seawater at various aqueous-to-extraction volume ratios. The extraction efficiency remained higher for seawater than for concentrated seawater but declined as the aqueous-to-extraction volume ratio increased. Shi et al.[95] proposed a different approach to remove ions such as Ca^{2+} and Mg^{2+} in brine using di-(2-ethylhexyl) phosphoric acid (D2EHPA) to recover lithium. Ca^{2+} and Mg^{2+} were extracted from the solution using multistage centrifugal extractors at rates of 99.05% and 98.48%, respectively, while lithium loss was kept under control at 5.22%. Although solvent extraction has a high product yield, the intensive use of organic solvents as solvents causes corrosion of process equipment and environmental pollution. Consequently, it is crucial to improve technologies for the sustainable extraction of lithium from water resources.[96]

2.9.4. Ion Exchange

The ion exchange process for lithium extraction from brines involves the use of ion exchange resins to selectively remove lithium ions from the brine solution. The process works based on the principle of ion exchange, where the resin material is designed

to attract and bind specific ions while releasing others. In the case of lithium extraction, the ion exchange resin is typically chosen to have a high affinity for lithium ions. The brine solution is passed through a column or bed containing the resin material. As the brine flows through the resin, the lithium ions in the solution are attracted to the resin and bind to its surface, effectively removing them from the solution.[6,86]

Both synthetic resins and natural zeolites are employed in the ion exchange process. Natural zeolites are preferred due to their cost-effectiveness and ability to selectively remove metals. The phosphorus-containing cationic exchange resins are mainly used for the preconcentration of thorium, lanthanides, and uranium.[97] Hérès et al.[98] studied the selective extraction of rare earth metals by using cationic exchange resins. Uranium and thorium extraction was achieved. However, there are drawbacks associated with this process, such as metallic impurities at relatively high concentrations and limitations in large-scale implementation. Additionally, synthetic resins can be expensive.[98,99]

2.9.5. Membranes

Membranes with nanostructured pore sizes ranging from sub-nanometers to several nanometers have aroused great interest in lithium recovery. Due to its benefits, including improved energy efficiency, simplicity of use, and continuous processing, this technology is promising.[100] Nanofiltration (NF) and electrodialysis (ED) have emerged as the most popular procedures at all scales for lithium extraction from brine at the pilot and commercial levels, despite other membrane-based technologies being examined in the laboratory. The main reasons for this are their moderate cost, low environmental impact, and higher selectivity. However, as with other recovery methods, the high Mg^{2+}/Li^{+} ratio in brine remains a challenge making the selective recovery of lithium on magnesium difficult.[101,102]

Ions are filtered via membranes with differing preferences for monovalent and divalent ions in a process known as nanofiltration. The membranes can be made of polymers, ceramics, or mixtures of ceramic and polymers.[103] It is required to dilute the brine before it comes into contact with the membranes to make it easier to separate monovalent Li^{+} ions from divalent ions like Mg^{2+} or Ca^{2+}. The significance of brine

dilution in lowering the osmotic pressure on the membranes has been emphasized in some research.[104,105] Furthermore, Sun et al.[106] found that membrane selectivity is negatively impacted by temperature increases above 18–20°C. This is explained by an increase in osmotic pressure, a decrease in solution viscosity, and modifications to membrane pore size. Wen et al.[102] and Somrani et al.[104] have demonstrated that nanofiltration is ineffective for separating Li^+ from high Mg^{2+} and B^+ brines. Furthermore, it is incapable of separating Li^+ from Na^+ ions.

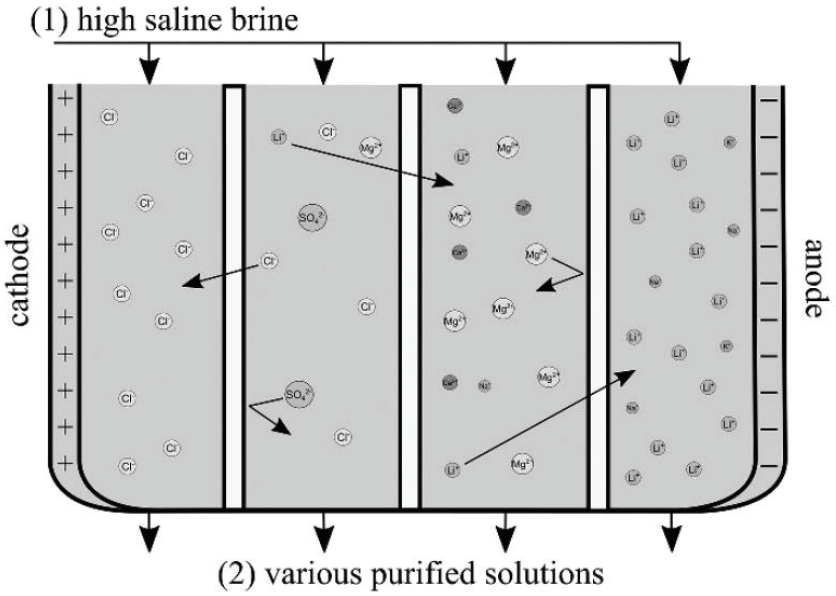

Figure 2.11. Electrodialysis membrane process[86]

The process of electrodialysis makes use of the different rates of monovalent and divalent cation diffusion caused by an electric current. A cathode, an anode, and an electrolyte medium are three requirements for performing electrodialysis.[87] The electrodes are subjected to redox processes that involve the inclusion of Li^+ ions as a result of the supplied electric current. In a manner similar to electrolysis, the anode removes Li^+ ions from the aqueous solution. However, electrodialysis sequentially separates the ions using semi-permeable membranes, purifying the recovered solution.[105] Brines with elevated salinity levels can serve as both the electrolyte and the source of lithium. Additionally, brines containing complex chemical compositions, such as those with high ratios of magnesium to lithium, can be treated by the electrodialysis process.

The semipermeable membrane in Figure 2.11 separates lithium and magnesium ions. The presence of sulfate ions enhances the recovery of lithium.[107] It is crucial to carefully regulate the voltage to prevent the deposition of contaminants, such as sodium and magnesium ions, on the electrodes.[108]

2.9.6. Adsorption

The adsorption process, a surface phenomenon, involves the adherence of molecules or ions from a gas or liquid to the surface of a solid material. When the fluid and adsorbent contact, the solute molecules attract to the surface of the adsorbent and accumulate on the surface, forming a thin layer or film. The solute being adsorbed is known as adsorbate, and the solid on which it is held is known as an adsorbent.[109]

Various mechanisms have been presented for the extraction of heavy metals by adsorption. The adsorption process can be divided into two basic mechanisms depending on the type of attraction between adsorbate and adsorbent. First, there is physical adsorption or physisorption, which occurs as a result of van der Waals forces, dipole interactions, and hydrogen bonding forces. In this mechanism, metal ions from the solution are transferred to the surface of the adsorbent and have an opposing surface charge. As a result, metal ions are effectively removed from the solution, crossing the boundary layer and binding to the adsorbent surface.[109] Another mechanism is chemical adsorption or chemisorption, which occurs due to electrostatic attraction resulting from covalent bonding. The material being adsorbed and the adsorbent, which has undergone particular chemical changes to form surface functional groups, interact chemically during chemisorption. These functional groups improve the adsorbed substance's binding, making it more tightly bound and requiring more energy to release.[110]

The adsorption process from the aqueous phase onto an adsorbent can be divided into three stages: (1) External diffusion, at this step, the molecules or ions of the adsorbate in the bulk solution approach the surface of the adsorbent and traverse the liquid film surrounding the adsorbent particle. (2) Internal diffusion; the adsorbate ions or molecules enter the adsorbent structure to adsorb all of the internal adsorbing sites completely. (3) The process of ions or molecules adhering to adsorption sites in the pore wall or adsorbent surface; at this point, the adsorption process may be chemical, physical, or both.

2.10. Lithium Recovery by Adsorption

The cost-effectiveness of the adsorption method, its environmentally friendly advantages, and the selective extraction of lithium resources from high Mg^{2+}/Li^{+} containing salt lake brines make it an excellent candidate for removing lithium from brines.[3,4,9] In recent years, there has been significant research on using manganese and titanium-based adsorbents to separate lithium from brine sources selectively. Specifically, delithiated manganese and titanium-based adsorbents obtained through the acid treatment of lithium-containing oxides have been the subject of extensive study.[111,112] Manganese-based adsorbents are more popular adsorbents for lithium owing to their remarkable regeneration performance, high lithium adsorption capacities, and superior lithium selectivity.[9]

2.10.1. Manganese Oxides

Manganese oxides possessing tunnel and layered crystal structures represent a diverse group of porous materials, ranging from ultramicroporous to mesoporous structures. Due to their remarkable cation exchange and molecular adsorption properties, these manganese oxides find applications in various fields such as catalysts, absorbents for toxic metals, ion sieves, molecular sieves, artificial oxidases, components in dry cells, inorganic pigments in ceramics, electrodes for lithium, magnesium, and sodium electrochemical batteries, as well as electrodes for supercapacitors.[113] Manganese oxides typically carry a negative surface charge, enabling them to adsorb metal ions effectively. This property allows them to play a crucial role in influencing and regulating the concentration, species, and chemical behavior of metals in water. Consequently, manganese oxides can be utilized as adsorbents for the extraction of lithium from water.[114]

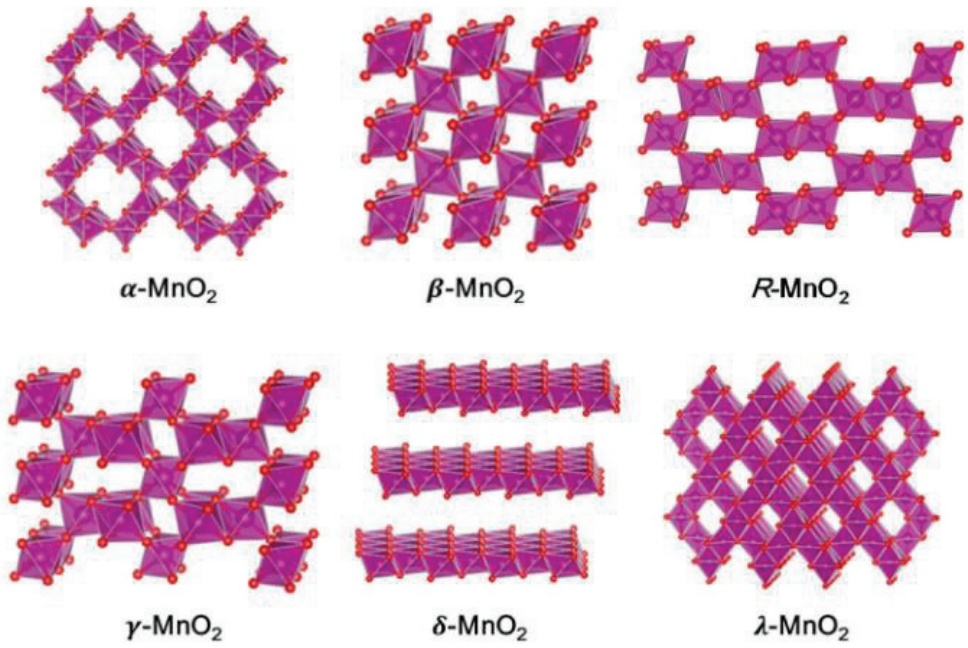

Figure 2.12. Crystal structures of MnO_2 polymorphs[115]

The majority of the structural frameworks of manganese oxides are composed of MnO_6 octahedral units that are interconnected through corner and edge-sharing.[116] Manganese oxides exhibit diverse morphologies and crystallographic structures, encompassing a range of forms such as the α-MnO_2 (2×2 tunnel or hollandite), β-MnO_2 (1×1 tunnel or pyrolusite), γ-MnO_2 (mix of 2×1 and 1×1 tunnels or nsutite), δ-MnO_2 (layered or birnessite), λ-MnO_2 (3-dimensionalpores or spinel), and R-MnO_2 (2×1 tunnel or ramsdellite) polymorphs (Figure 2.12). Crystallographic data of these major manganese oxide polymorphs are given in Table 2.3. The different polymorphs possess unique atomic configurations, leading to the presence of diverse types of pores or tunnels within their crystal structures. The occurrence of polymorphism results from the distinct manners in which the MnO_6 octahedral architectural units are interconnected, either through corner-sharing or edge-sharing, leading to variations in the structures of chains and tunnels.[113] This specific arrangement of atoms contributes to a significant range of selectivity toward various ions and electron transfer kinetics.[115]

Table 2.3. Crystallographic data of some manganese dioxide[113]

Polymorph	Mineral	Crystal Symmetry	Lattice Parameters (Å)	Features
α-MnO_2	Hollandite	Tetragonal	a=9.96; c=2.85	(2 × 2) tunnel
β-MnO_2	Pyrolusite	Tetragonal	a=4.39; c=2.87	(1 × 1) tunnel
γ-MnO_2	Nsutite	Complex Tunnel	a=9.65; c=4.43	(1×1)/(1×2)
δ-MnO_2	Birnessite	Rhombohedra	a_{hex}=2.94; c_{hex}=21.86	(1 × ∞) layer
λ-MnO_2	Spinel	Cubic	a=8.04	(1 × 1) tunnel
R-MnO_2	Ramsdellite	Orthorhombic	a=4.53; b=9.27; c=2.87	(1 × 2) tunnel

2.10.1.1. Lithium Manganese Oxide Type Lithium-Ion Sieves

The lithium-ion sieve (LIS) is an adsorbent designed explicitly for lithium ions, offering several advantages, such as low toxicity, affordability, excellent chemical stability, and a high capacity for Li^+ uptake. Due to these favorable characteristics, it is regarded as a highly promising adsorbent for lithium ions.[117–119] LIS can be categorized into two primary types of adsorbents as the spinel lithium manganese oxide (LMO) type and the lithium titanium oxide (LTO) type. LMO-type lithium-ion sieve is known for its rapid adsorption rate and exceptional selectivity towards lithium, while LTO-type lithium-ion sieve is recognized for its minimal dissolution loss and extended recyclability.[4] The LMO-type lithium-ion sieve is a more favored lithium adsorbent because of its high lithium selectivity, significant lithium adsorption capacities, and great regeneration performance.[67]

An ion-sieve adsorbent is an inorganic material that introduces template ions into an inorganic compound through redox or ion exchange reactions. The compound oxide is obtained through a heating process, where the template ions are then removed from their crystal positions using an eluent, leaving behind vacant crystal sites. These inorganic materials possess well-defined crystal sites that can only accommodate ions with smaller or equal ionic radii compared to the target ion structure. This property enables them to accept template ions and achieve an optimal crystal configuration selectively. As a result, these template ions exhibit a reliable screening and memory effect, allowing them to adsorb target ions even in the presence of multiple ions. This phenomenon is known as

the "ion-sieve effect." In the case LIS, only lithium ions can occupy the vacancies due to their smaller ion radius compared to other metal ions (Figure 2.13).[4,7,9]

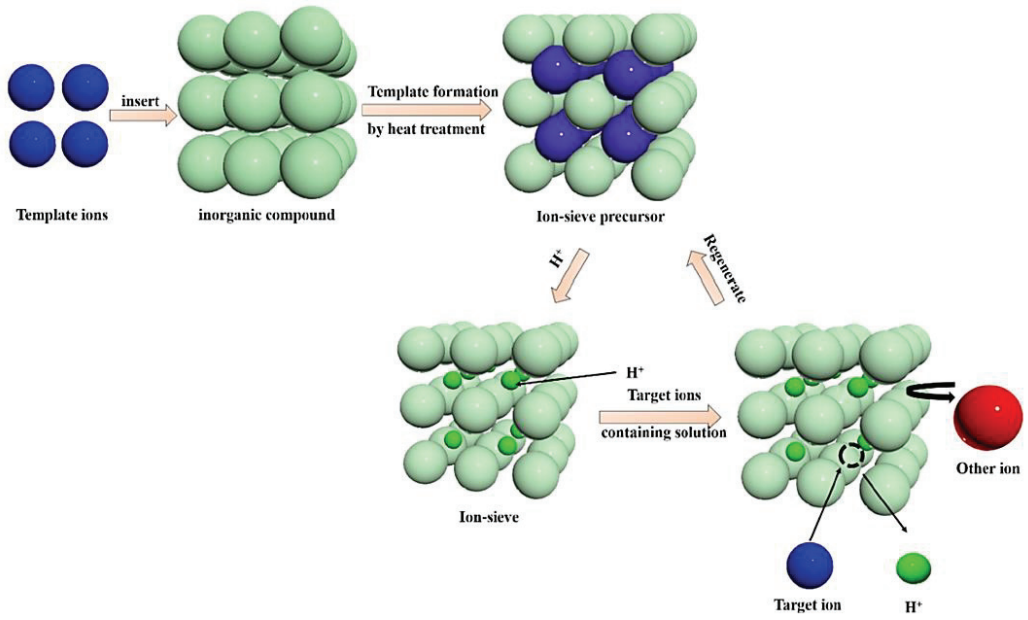

Figure 2.13. Illustration of Ion-sieve preparation and the ion sieve effect[9]

Due to their exceptional affinity for Li^+ ions, spinel-type hydrous manganese oxides (λ-MnO_2) have been extensively investigated as lithium adsorbents.[120] The majority of LMO-type ion-sieves have been produced by subjecting the corresponding LMO precursors, such as $LiMn_2O_4$, $Li_{1.33}Mn_{1.67}O_4$, $Li_{1.6}Mn_{1.6}O_4$, and $Li_4Mn_5O_{12}$, to acid treatment. This treatment results in the substitution of nearly all Li^+ ions with protons, forming lithium-ion sieves.[121] The structure and performance of the ion sieve are significantly influenced by the morphology of the precursor. The spinel lattice structure and framework of the lithium-ion sieve provide it with high selectivity, capacity, and excellent memory characteristics. The memory effect of the exchange sites can be attributed to two factors: the similarity in ionic radius and the approximate energy of dehydration. Ions larger than Li^+ (0.074 nm), such as Na^+ (0.102 nm), K^+ (0.138 nm), and Ca^{2+} (0.100 nm), are unable to occupy the sites within the ion sieve. Even for Mg^{2+} (0.072 nm), which has a similar ionic radius to Li^+, it requires higher energy for dehydration ((ΔG_h^o) Mg^{2+} = -1980 kJ/mol) compared to ((ΔG_h^o) Li^+ = -475 kJ/mol) in order to enter these sites.[122]

Chitrakar et al.[8] conducted novel research in developing manganese-based adsorbents, specifically focusing on selectively capturing lithium. Their study involved the synthesis of adsorbents based on manganese oxide for the efficient recovery of lithium from brine. As a precursor, they utilized $LiMnO_2$ to create a delithiated oxide adsorbent with a chemical composition of $Li_{1.6}Mn_{1.6}O_4$. Over three days, the adsorbent demonstrated a remarkable ability to capture lithium from seawater, achieving a high capacity of 40 $mg \cdot g^{-1}$ and a recovery rate exceeding 80%. Zandvakili et al.[123] carried out a study on the recovery of lithium from Urmia Lake using LMO-type ion-sieve. Their research demonstrated that a lithium recovery rate exceeding 90% could be achieved.

CHAPTER 3

EXPERIMENTAL

3.1. Materials

Polyester-based thermoplastic polyurethane (TPU) Ravathane® was purchased from Ravago (Türkiye) and used as received without any further purification. N,N-Dimethylformamide (DMF, 99.0%, ISOLAB, Germany) and Tetrahydrofuran (THF, ≥99.0%, Sigma-Aldrich, USA) were used to dissolve the TPU. The λ-MnO_2 powder was purchased from Xiamen Acey (China) as the adsorbent material for lithium adsorption. Lithium chloride (LiCl, ≥99.0%) was supplied from Carlo Erba (Italy) and used as received without any further purification. Hydrochloric Acid (HCl, Fuming 37%, ISOLAB, Germany) and Sodium Hydroxide (NaOH, ≥97.0%, Sigma-Aldrich, USA) were used for pH adjustment of lithium solutions. Salt lake brine was collected from Lake Tuz (Türkiye) to be used in lithium extraction experiments.

3.2. Fabrication of PU Electrospun Mats

PU was dissolved in DMF and THF to obtain a PU solution. The polymer solution was stirred in a magnetic stirrer overnight. PU solutions were prepared at PU concentrations of 14, 16, 18, 20, 22, 25, 30, and 35 wt% with DMF:THF ratios (v/v) of 3:0, 2:1, 1:1, 1:2, and 0:3 to observe the effect of PU concentration and DMF:THF ratio on the structure of electrospun fibers and determine the optimal concentration and solvent ratio. PU electrospun mats were fabricated by the electrospinning method (Figure 3.1). PU solution was loaded into a 10 mL plastic syringe with a metal needle. After the syringe was placed on the syringe pump, positive and negative electrodes of the high-voltage power supply were attached to the metal needle and collector, respectively. The electric field between the needle tip and the collector was formed by applying voltage, and the

electrospinning process started. While 15 kV voltage was applied to solutions with different PU concentrations and DMF:THF ratios, tip to collector distance and flow rate were kept constant at 10 cm and 0.5 $mL \cdot h^{-1}$, respectively. Moreover, 5, 10, 15, and 20 kV voltage values and 0.5, 1, 1.5, and 2 $mL \cdot h^{-1}$ flow rates were applied to examine the effects of flow rate and voltage while keeping PU concentration and DMF:THF ratios constant. During the electrospinning processes, the temperature and relative humidity of the environment were 25±2 ºC and 45±1%, respectively. Electrospun fibers were collected on aluminum foil. After solvent evaporation, the PU electrospun mats were separated from the aluminum foil.

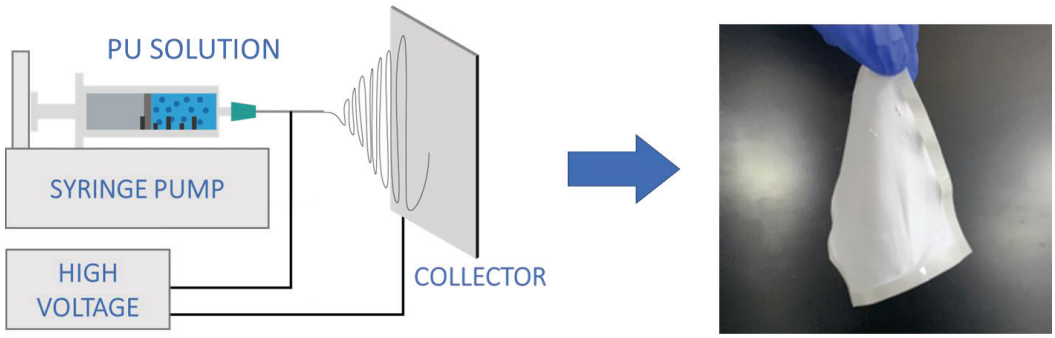

Figure 3.1. Fabrication process of PU electrospun mats.

3.3. Characterization of PU Electrospun Mats

The structure and spinnability of PU solutions due to solution concentration and solvent ratio were first examined in a light microscope (Olympus BX53, Japan). The morphology of the PU electrospun mats was examined by using a scanning electron microscope (SEM, FEI Quanta 250 FEG, USA). The electrospun mats on the aluminum foil were cut into $1cm^2$ dimensions and coated with gold using a SPI-Module Sputter Coater (SPI Supplies, USA). A phase diagram was created showing the effect of PU concentration and solvent ratio on fiber structure according to fiber properties and bead formation. The distribution of fiber diameters and the average diameters of nanofibers were determined using ImageJ software (National Institutes of Health, USA). A hundred different points were measured for each sample image, and the data were organized using

OriginPro software (OriginLab Corporation, USA). Moreover, PU electrospun nanofiber was observed with an atomic force microscope (AFM, Bruker-MMSPM Nanoscope 8, USA) in an air medium using the tapping mode to determine segments of the polymer.

3.4. Characterization of λ-MnO_2

The morphology of the λ-MnO_2 adsorbent was examined by using an SEM (FEI Quanta 250 FEG, USA). Particle size and zeta potential values of the λ-MnO_2 were measured by dynamic light scattering (DLS, Malvern Nano-ZS, UK). The crystalline structure and phases present in the λ-MnO_2 powder were determined using an X-ray diffractometer (XRD, Philips X'Pert Pro, Netherlands). The sample underwent scanning in the 2θ range of 10° - 80° at a scanning rate of 0.08° per second.

3.5. Deposition of λ-MnO_2 on Electrospun Mats

Deposition of λ-MnO_2 on the produced PU electrospun mats was carried out by vacuum-assisted deposition on them. Firstly, specific amounts of λ-MnO_2 powder were mixed in pure water according to the amount desired to be deposited on PU electrospun mats. The mixture was mixed by using a vortex mixer (ISOLAB, Germany) to obtain a good λ-MnO_2 dispersion. Vacuum filtration apparatus (MilliporeSigma, USA) was used for the vacuum-assisted deposition process (Figure 3.2).

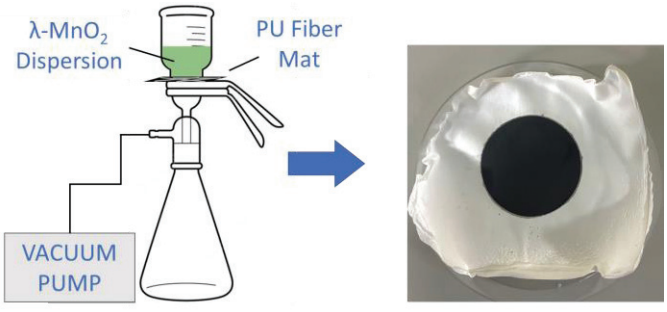

Figure 3.2. Deposition process of λ-MnO_2 on the produced PU electrospun mats.

The fabricated PU electrospun mat was put on the glass filtering head and fixed by placing the filtering cup on it. A certain amount of λ-MnO_2 dispersion was poured into the filtering cup, and vacuum-assisted deposition was made using a vacuum pump (KNF Neuberger, Germany). PU electrospun mats deposited with λ-MnO_2 were placed in a desiccator to dry for use in filtration experiments. Moreover, the vacuum-assisted deposition procedure was also applied to common woven fabrics to compare the λ-MnO_2 retention performance of PU electrospun mats with fabrics.

3.6. Characterization of λ-MnO_2 Deposited PU Electrospun Mats

The structure of the λ-MnO_2 deposited PU electrospun mat was examined by using an SEM (FEI Quanta 250 FEG, USA). Thermal properties of λ-MnO_2 deposited PU electrospun mats were investigated by thermogravimetric analysis (TGA, Perkin Elmer Diamond TG/DTA, USA) between the temperature ranges of 25-610°C under a nitrogen atmosphere at a heating rate of 10°C·min^{-1}. The derivative thermogravimetry (DTG) results were obtained by taking the temperature derivative of mass loss at a constant heating rate. Dynamical scanning calorimeter (DSC, Perkin Elmer, USA) analysis from 55°C to 120°C under a nitrogen atmosphere at a heating rate of 10°C·min^{-1}.

3.7. Lithium Extraction Experiments

Filtration experiments with λ-MnO_2 deposited PU electrospun mats were performed using a vacuum filtration apparatus (MilliporeSigma, USA) to observe lithium extraction performance. Synthetic lithium (Li^+) containing solutions with various concentrations were prepared by dissolving LiCl in deionized water. The λ-MnO_2 deposited PU electrospun mat was put on the glass filtering head and fixed by placing the filtering cup on it. A certain amount of synthetic Li^+ solution was poured into the filtering cup, and vacuum-assisted deposition was made using a vacuum pump (KNF Neuberger, Germany). After filtration, Li^+ concentration in the filtrate and the initial solution before filtration were measured by a flame photometer (Sherwood Model 410, UK). The

parameters, including λ-MnO_2 amount, initial Li^+ concentration, solution pH, and fiber diameter were investigated. Moreover, the filtration process was made as multi-stage filtration and by using stacked λ-MnO_2 deposited PU electrospun mats. The lithium extraction percentage (R%) of λ-MnO_2 deposited the mats is calculated by Equation 3.1.

$$R\% = \frac{C_0 - C_e}{C_0} \times 100 \tag{3.1}$$

Where C_0 is the initial Li^+ concentration in solution (mg/L); C_e is the Li^+ concentration of the solution after the filtration process (mg/L).

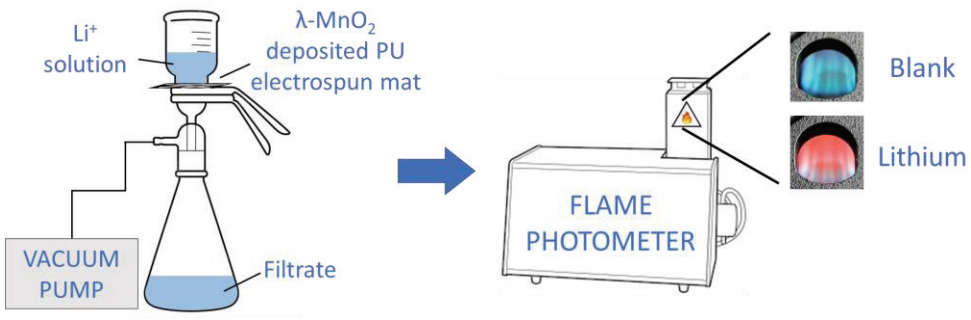

Figure 3.3. Schematic representation of lithium extraction experiments.

3.7.1. Sample Preparation

The preparation of synthetic Li^+ solutions was done at certain concentrations. To create a 200 mg/L Li^+ solution, a sample containing 244.3 mg of LiCl was dissolved in 200 mL of deionized water. The 200 mg/L stock solution was diluted to create other concentrations. The pH adjustment of Li^+ solutions was made using 1 M HCl and 1 M NaOH solutions. For the 100 mL 1 M HCl solution, 50 mL deionized water was added to a 100 mL volumetric flask; after 8.3 mL of 37% HCl (12 M) was added, it was completed with deionized water up to 100 mL. For the 100 mL 1 M NaOH solution, 50 mL deionized water was added to a 100 mL volumetric flask; after 4 g of NaOH pellets (40 g/mol) was added, it was completed with deionized water up to 100 mL. While making pH

adjustments, the pH values of Li^+ solutions were measured by pH meter (WTW pH 7110, Germany).

3.7.2. Miscellaneous Parameters

λ-MnO_2 Amount: To examine the effect of the λ-MnO_2 amount deposited on PU electrospun mats on Li^+ extraction performance, 35, 75, 145, 200, and 265 mg of λ-MnO_2 were deposited on PU electrospun mats. 10 mL of 200 mg/L Li^+ solutions at 12 pH were filtered with each λ-MnO_2 deposited PU electrospun mat. The Li^+ solution was also filtered with PU electrospun on which λ-MnO_2 was not deposited.

Initial Li^+ concentration: Li^+ solutions with concentrations of 50, 100, 150, 200, and 250 mg/L were prepared, and the pH of each solution was adjusted to pH 12. An aliquot of 10 mL of each Li^+ solution was filtered with 200 mg λ-MnO_2 deposited PU electrospun mats to study the effect of initial Li+ concentration on Li^+ extraction performance.

Solution pH: To investigate the impact of solution pH on Li^+ extraction performance of λ-MnO_2 deposited PU electrospun mats, 10 mL of 200 mg/L Li^+ solution with different pH values of 4, 6, 8, 10, and 12 were filtered with 200 mg λ-MnO_2 deposited PU electrospun mats. Droplets of solutions containing 1 M NaOH and 1 M HCl were used to modify the pH.

Fiber Diameter: To investigate the effect of the fiber diameter of PU electrospun mats on Li^+ extraction performance, 200 mg of λ-MnO_2 were deposited on PU electrospun mats with an average fiber diameter of 550, 620, 690, and 750 nm. An aliquot of 10 mL of solution containing 200 mg/L Li^+ at pH 12 were filtered through each λ-MnO_2 deposited PU electrospun mat having different fiber diameters.

3.7.3. Stacked λ-MnO_2 Deposited PU Electrospun Mats

Various numbers of λ-MnO_2 deposited PU electrospun mats were used as stacked layer by layer for the filtration process to enhance extraction performance. An aliquot of

10 mL of 200 mg/L Li^+ solutions at 12 pH and 200 mg λ-MnO_2 deposited PU electrospun mats were used in each filtration. Experiments were done with 1, 2, 3, 4, and 5 layers of λ-MnO_2 deposited PU electrospun mats.

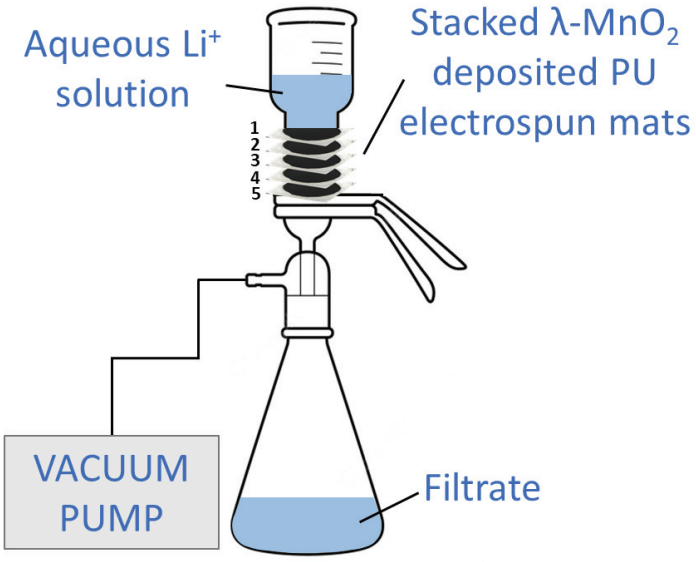

Figure 3.4. Schematic representation of the lithium extraction with stacked mats.

3.7.4. Multi-Stage Filtration

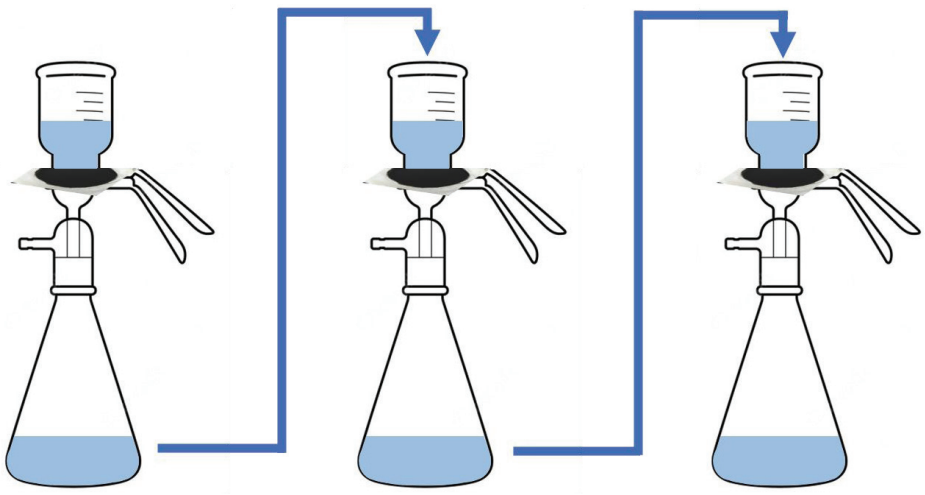

Figure 3.5. Schematic representation of multi-stage filtration.

Multi-stage filtration was applied as another method to increase Li^+ extraction performance. The solution was consecutively filtered with 200 mg λ-MnO_2 deposited PU electrospun mats. The filtrate in the previous filtration process was used as the feed of the subsequent filtration (Figure 3.5). The first filtration process was started with 10 mL of 200 mg/L Li^+ solutions at 12 pH. Cumulative Li^+ extraction was examined at the end of the fifth filtration. Moreover, this method was repeated using Li^+ solutions with 100, 200, 300, and 400 mg/L concentrations to observe the extraction at various initial Li^+ concentrations.

3.7.8. Salt Lake Brine

Filtration experiments were conducted with salt lake brine to assess the lithium extraction performance of λ-MnO_2 deposited PU electrospun mats in aqueous systems containing multiple ions. To examine the effect of the λ-MnO_2 amount deposited on PU electrospun mats on Li^+ extraction performance, 50, 100, 150, and 200 mg of λ-MnO_2 were deposited on PU electrospun mats. An aliquot of 10 mL of salt lake brine was filtered with each λ-MnO_2 deposited PU electrospun mat. The salt lake brine was also filtered with PU electrospun, on which λ-MnO_2 was not deposited. The ICP-OES method was used to measure the concentrations of Li^+, Na^+, Mg^{2+}, Ca^{2+}, K^+, and Sr^{2+} in the salt lake brine.

CHAPTER 4

RESULTS AND DISCUSSION

4.1. Characterization of PU Electrospun Mats

PU was dissolved in DMF and/or THF at various concentrations (14, 16, 18, 20, and 22 wt%). In addition to using pure DMF or THF solvents, mixtures of DMF and THF with volume ratios of 2:1, 1:1, and 1:2 were also used. Solutions were electrospun at an electric field of 0.67 $kV \cdot cm^{-1}$ (applied voltage: 10 kV and TCD: 15 cm). Various structures were examined in the light microscope to determine the spinnability of polymer solutions. Light microscope images of the PU electrospun mats fabricated at several concentrations in the pure and binary solvent mixtures are presented in Figure 4.1.

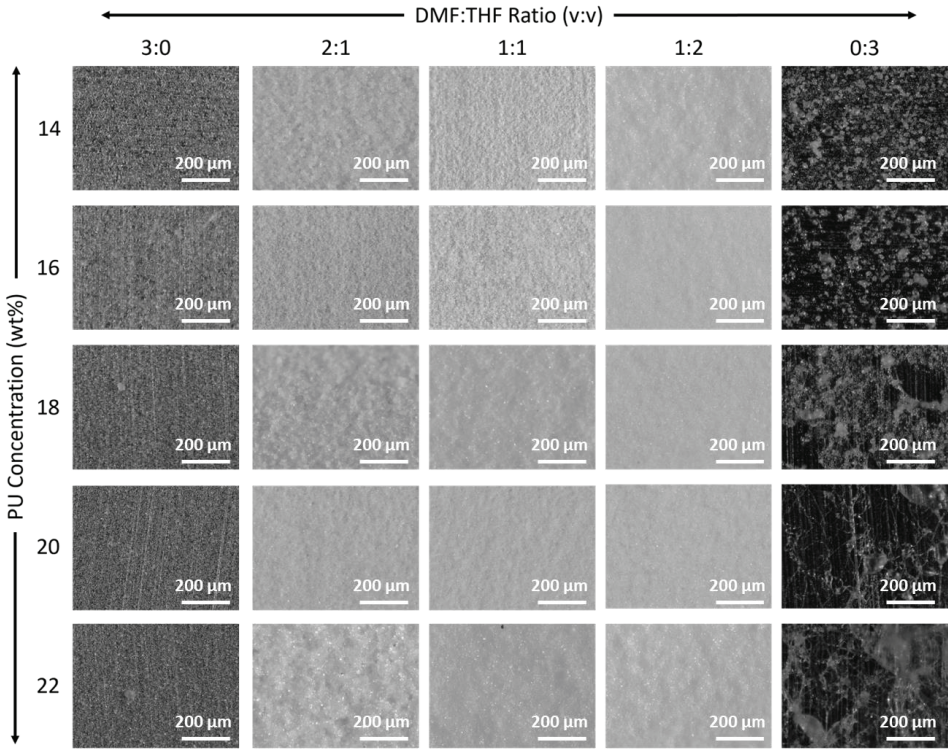

Figure 4.1. Light microscope images of the PU fibers with respect to various solvent compositions and PU solution concentrations.

The first column of the light microscope images depicts the electrospun fibers obtained from neat DMF (DMF:THF = 3:0) at various PU concentrations. The black background, rarely seen in the images, represents aluminum foil. This point suggests that there is no effective spinning and no fiber formation on the aluminum foil. The same result is more evident in the last column of light microscope images showing electrospun fibers from pure THF (DMF:THF = 0:3) at different PU concentrations. Vapor pressure values, which determine the volatility of solvents, directly affected the spinnability of the solutions. The low volatility DMF (vapor pressure = 0.4 kPa) prevented the nanofiber from drying during jet flight. On the other hand, the high volatility THF (vapor pressure = 18.9 kPa) caused the polymer jet to dry very quickly and caused occlusion at the needle tip. However, this was not observed when DMF and THF were mixed in specific proportions, as seen in the middle columns of the light microscope images. All surfaces of aluminum foils were covered entirely with fibers. The findings align with previous results in the literature, which indicate that mixing solvents with high and low volatilities enhance the spinnability of the solution and help prevent clogging.[124,125] Furthermore, it was observed that the electrospinning process was unstable and often interrupted when THF was used as a single solvent in the study of Liu et al.[32] After preliminary examination by light microscope, PU electrospun fibers were examined by SEM.

Figure 4.2 shows scanning electron microscopy (SEM) images of the PU electrospun mats produced using various concentrations both in pure solvents and binary solvent mixtures. In the SEM images, the effect of poor spinnability on the structure can be clearly seen when only one solvent is used independent of the chemistry of the solvent. It is seen that in the solution formed with pure DMF in the first column, especially at low concentration (14 wt%), merely polymer droplets are formed. As the concentration increases, the polymer chains may undergo aggregation. In the last column, it has been observed that sparse bead chains are formed due to clogging at the needle tip in fiber structures using pure THF. As the PU concentration increased, the fiber formation between the beads increased. The fibers thickened and became prominent, but the beads in the structures also grew at this rate at concentrations of 20 and 22 wt%. When the systems in which DMF and THF were used as a binary mixture were examined, the use of DMF at a ratio of 2:1 caused intense bead formations; only very fine fiber formations were seen between the beads at 22 wt%. Fibers formed between the beads with equal use of solvents (DMF:THF = 1:1) were also observed at lower concentrations. In the solvent mixture where the ratio for THF is higher (DMF:THF = 1:2), the bead distribution

decreased, and the fiber diameters increased as the concentration increased. These findings are consistent with the findings reported in previous studies. Ki et al.[23] and Rwei et al.[31] examined the impact of polymer concentration on the structure of electrospun fibers. They observed that the solution was only sprayed at lower concentrations, and no fiber formation occurred. Even when the concentrations were increased, although fibers were obtained, many beads and droplets formed.

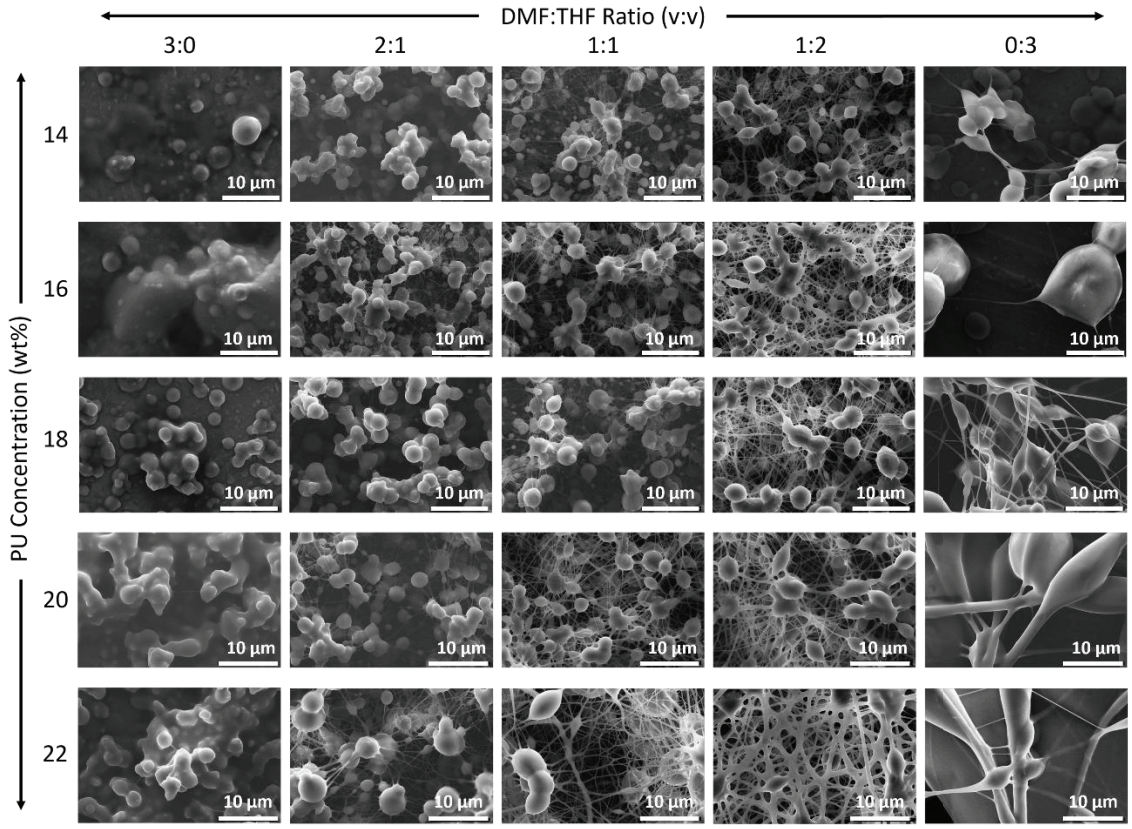

Figure 4.2. SEM images of the PU fibers with respect to various solvent compositions and PU solution concentrations.

The results showed that when the PU concentration was increased, the fiber formation increased, and the number of beads lessened. Therefore, additional solutions were prepared at concentrations of 25%, 30%, and 35% by weight. In addition, since there was no proper spinning process when DMF and THF were used purely, these solutions were prepared with binary mixtures of DMF and THF (2:1, 1:1, and 1:2 by volume). SEM

images of the fabricated electrospun fibers are shown in Figure 4.3. The resulting images proceeded in parallel with the nanofiber structures in the previous results of this study. As the PU concentration increased, the beads decreased, and the thickness of the fibers increased. However, large beads were formed in the fibers produced with the solvent mixture in which DMF was used excessively (DMF:THF = 2:1). Beads were also observed in fibers fabricated from a mixture of DMF and THF in equal amounts (DMF:THF = 1:1). Bead-free electrospun nanofiber structure was produced in a 1:2 solvent (DMF:THF = 1:2) system with a 30 and 35 wt% PU concentration.

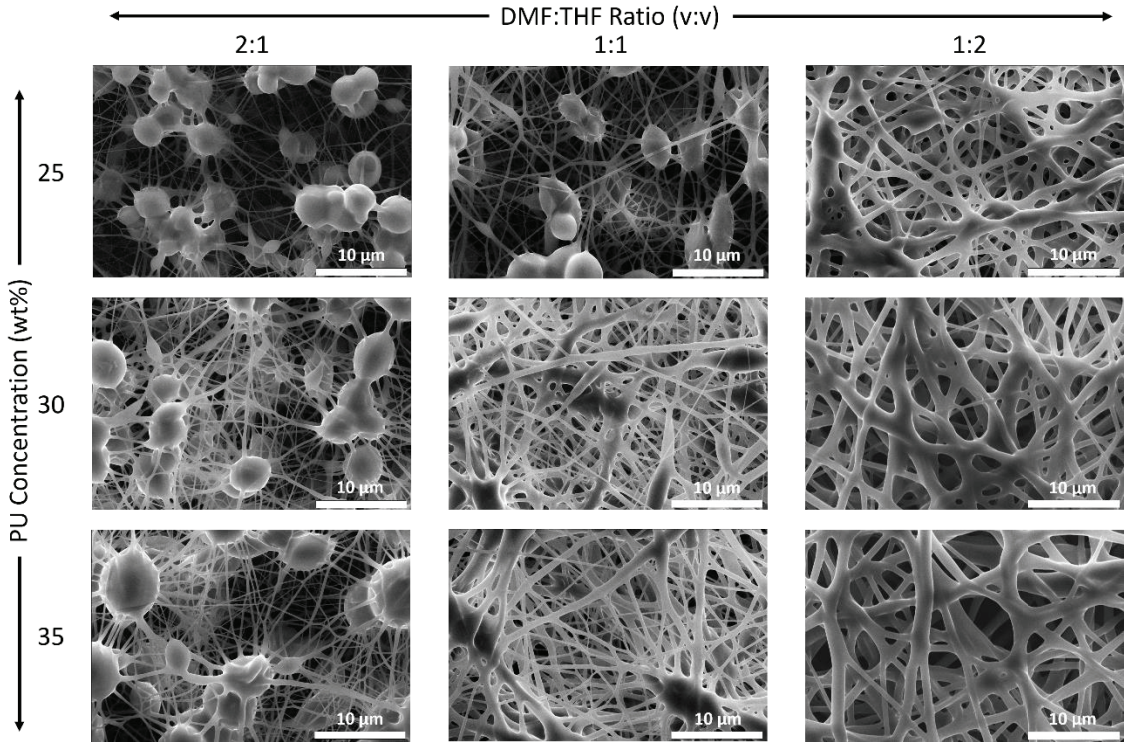

Figure 4.3. SEM images of the PU fibers with respect to various solvent compositions and PU solution concentrations.

Considering the comprehensive data shown in Figure 4.2 and Figure 4.3, it is possible to design a representation illustrating the different structures of the fibers, which are influenced by the solvent composition and polymer solution concentration. Figure 4.4 shows a phase diagram of PU fiber morphology concerning both parameters. The boundaries were established by making estimations based on the SEM images. Bead

chains were observed from the 10 and 15 wt% PU concentrations in neat THF, 1:2, and 1:1 solvent by volume. At these PU concentrations, polymer droplets were formed in pure DMF and a 2:1 solvent (DMF:THF = 2:1) system. PU fibers fabricated from DMF-rich systems showed polymer aggregation and large beads at 15 to 35 wt% concentrations. On the other hand, at the same concentration values, fiber formation was observed in systems where THF was used at higher rates. However, bead-free and smooth fibers were fabricated with a 1:2 solvent (DMF:THF = 1:2) system at 30 and 35 wt% PU concentrations. For this reason, the solvent ratio (DMF:THF) for the fibers to be produced in the rest of the study was determined as 1:2 by volume and the PU concentration as 30% by weight.

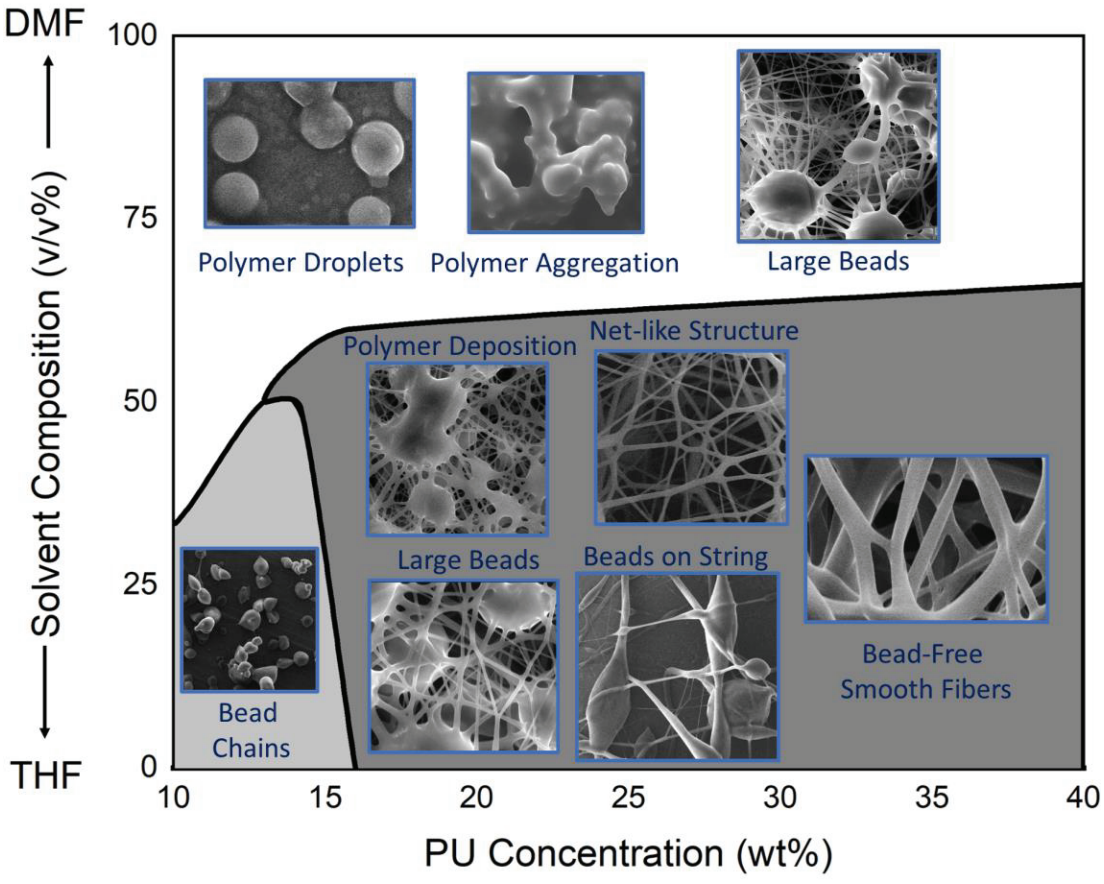

Figure 4.4. Fiber morphology dependence on DMF:THF composition and PU solution concentration.

Average fiber diameters (AFD) of electrospun fibers produced in a 1:2 solvent (DMF:THF = 1:2) system at various PU concentrations were determined from SEM images. Average fiber diameters were 180±12, 290±19, 426±15, 729±23, and 928±24 nm for 15, 20, 25, 30, and 35 wt% PU concentrations, respectively. The variation of average fiber diameters depending on the concentration is shown in Figure 4.5. As the solution concentration increases, the fibers become thicker. Higher polymer concentration may increase entanglement and chain interactions in solution, resulting in the formation of thicker fibers. The relationship between the average fiber diameter and solution concentration follows a power law pattern (AFD = [Concentration]^2). The results obtained are in agreement with the studies in literature. Various studies have observed that AFD increases as concentration increases, and they have a power law relationship.[14,23,126]

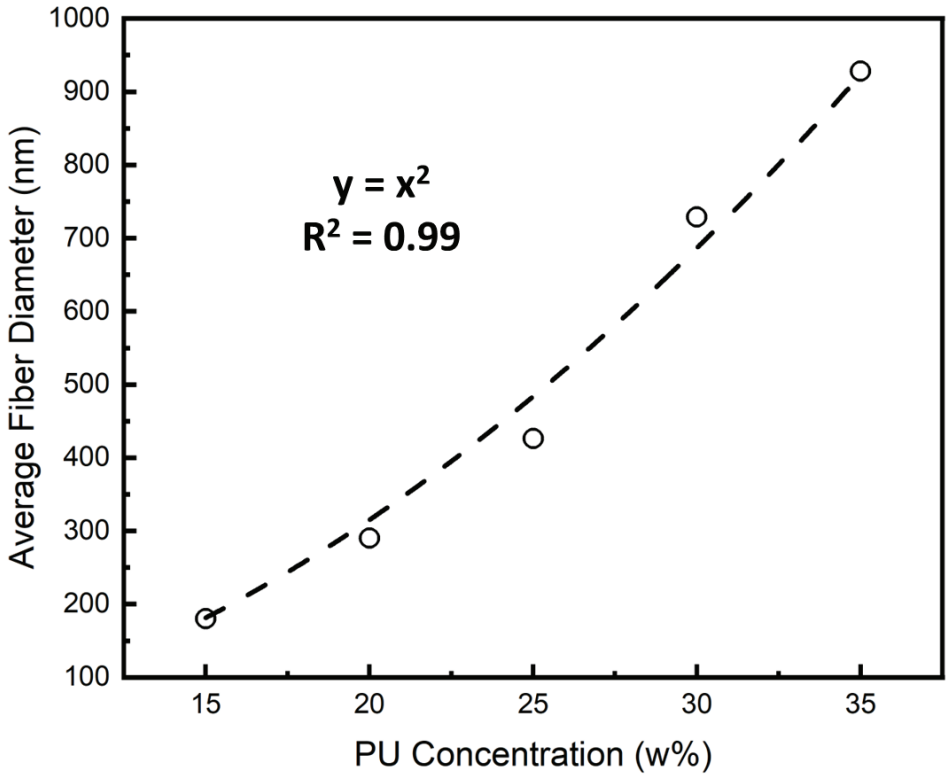

Figure 4.5. The variation of AFD depending on the concentration.

After investigating the effects of solvent composition and PU concentration on fiber structure and AFD, the influences of electrospinning parameters, flow rate and tip

to collector distance (TCD), on AFD were examined. PU concentration was kept constant at 30 wt%, solvent ratio 1:2 by volume, TCD 15 cm, and applied voltage at 10 kV, while the flow rate was varied between 0.5 and 2 $mL \cdot h^{-1}$. Figure 4.6 illustrates the SEM micrographs and AFD of electrospun fibers. Average fiber diameters were 729, 696, 628, and 582 nm for flow rates of 0.5, 1, 1.5, and 2 $mL \cdot h^{-1}$, respectively. As the flow rate increased, the AFD of fibers decreased, and bead formation increased. The decrease in AFD with an increase in flow rate contrasts with the results in the literature. Fibers produced at a higher solution flow rate exhibited larger diameters.[35,36] Due to the higher flow rate, the highly charged nanofiber is incompletely dried during the flight between the needle tip of the jet and the collector, resulting in the formation of beads. These findings are consistent with the ones reported in studies of Yuan et al[43] Wannatong et al.[44], and Zuo et al.[45]

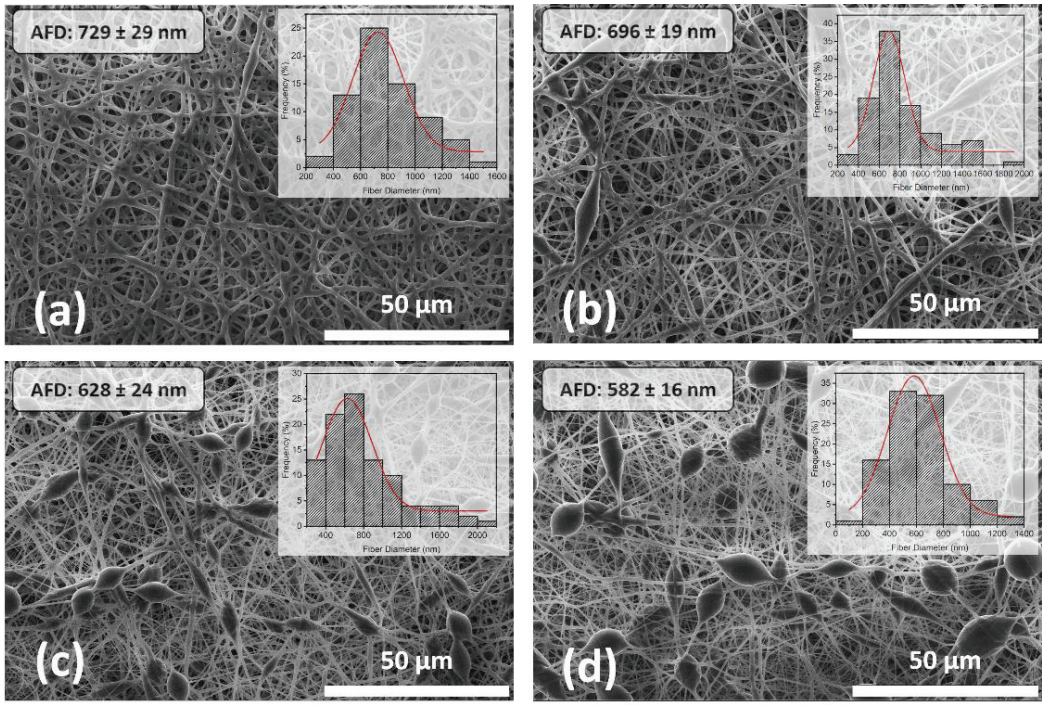

Figure 4.6. SEM images and AFD of PU fibers fabricated with flow rates of (a) 0.5, (b) 1, (c) 1.5, and (d) 2 $mL \cdot h^{-1}$.

In order to examine the TCD effect on morphology and AFD of fibers, PU concentration was kept constant at 30 wt%, solvent ratio 1:2 by volume, flow rate 0.5

mL·h^{-1}, and applied voltage at 10 kV, while the TCD was varied between 5 and 20 cm. SEM images and AFDs of electrospun fibers are shown in Figure 4.7. Average fiber diameters were 905±51, 865±57, 729±29, and 563±35 nm for TCD of 5, 10, 15, and 20 cm, respectively. As the TCD increased, AFD of fibers decreased. Moreover, beads were formed when the TCD was reduced to 5 cm. When the distance is shortened, the necessary time for solvent evaporation cannot be achieved. Thus, thicker fibers and bead formations were observed as the distance got shorter. These results align with the results reported in the existing literature. Matabola et al.[41] and Wang et al.[127] conducted research on the influence of the TCD and found that when the distance is kept short, it leads to the formation of defective and large-diameter nanofibers, whereas increasing the distance results in a decrease in nanofiber diameter.

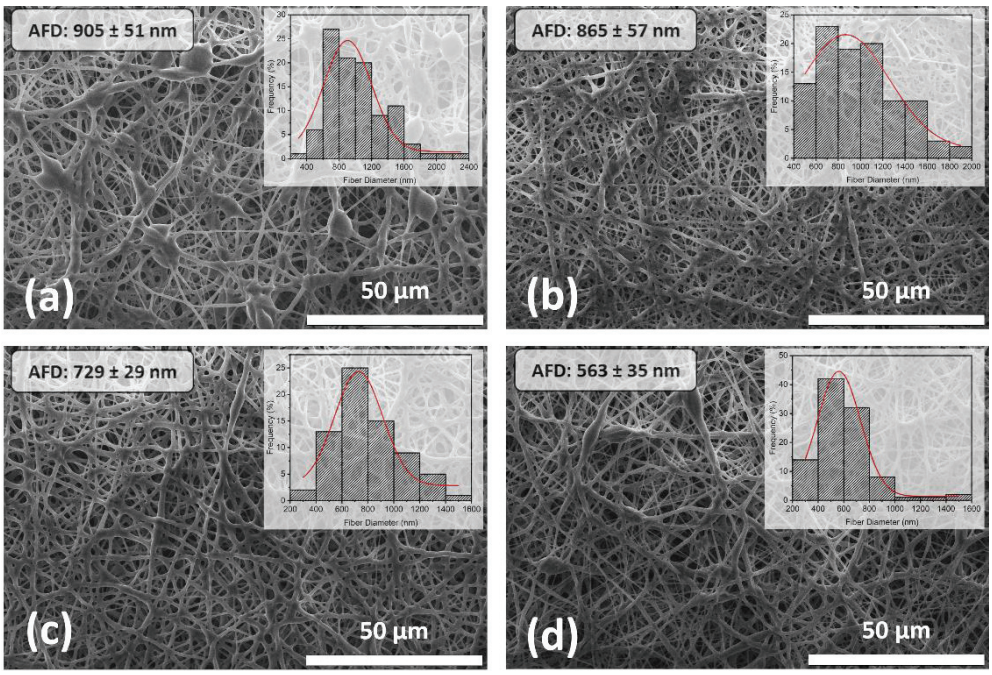

Figure 4.7. SEM images and AFDs of PU fibers with TCD of (a) 5, (b) 10, (c) 15, and (d) 20 cm.

The TPU cast film and the TPU electrospun fiber were produced using a TPU solution with a solvent ratio of 1:2 (DMF:THF = 1:2) and a concentration of 30 wt% to investigate the structure of the produced mats using AFM. The AFM phase images of TPU film and fiber are shown in Figure 4.8. The dark contrast in AFM was observed in

the soft segments, while the bright contrast was seen in the hard segments, assuming that the contrast difference was primarily influenced by the stiffness of the sample. Soft and hard segment domains in rodlike shapes were randomly distributed. These randomly oriented rodlike structures had an average size of 200±10 nm in length and 25±2 nm in width. This examined phase separation of the TPU has been observed in previous literature studies.[128,129] Terban et al.[129] studied the distribution of hard and soft segments in TPU and reported structures with an average width of 27 nm and a length of more than 200 nm. Moreover, dark and light areas indicating the hard and soft segments of TPU fiber were also observed in the fiber. However, the rodlike shapes seen in the film were not formed in the fiber. The fabricating process of the materials may have caused this difference. Stretching or spinning during fiber formation may have disrupted the formation of rodlike domains by changing the arrangement and orientation of the polymer chains.

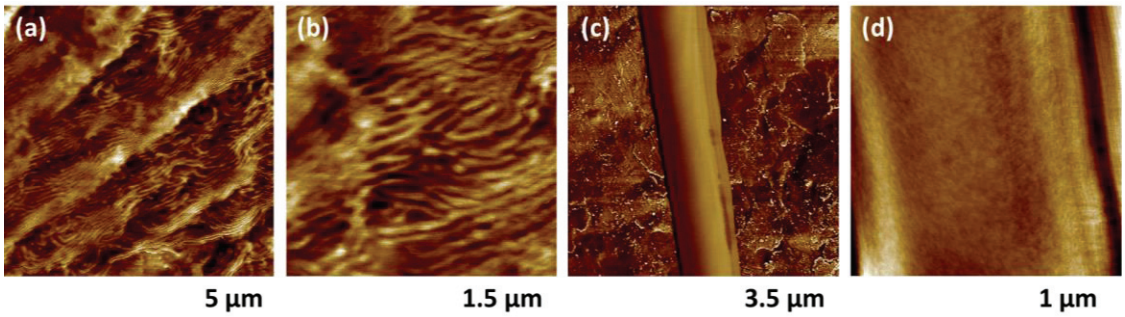

Figure 4.8. AFM phase images of TPU film with scan size of (a) 5 and (b) 1.5 µm and fiber with scan size of (c) 3.5 and (d) 1 µm.

4.2. λ-MnO_2 Characterization

SEM analysis was conducted to examine the morphology of the λ-MnO_2 powder (Figure 4.9). The presence of significant aggregation in the structure is not unexpected, considering the tendency of solid powder particles to agglomerate due to attractive forces between them. λ-MnO_2 materials consist of octahedral spinel granules with smooth

surfaces. The primary particles of the aggregates have a submicron diameter spherical shape.

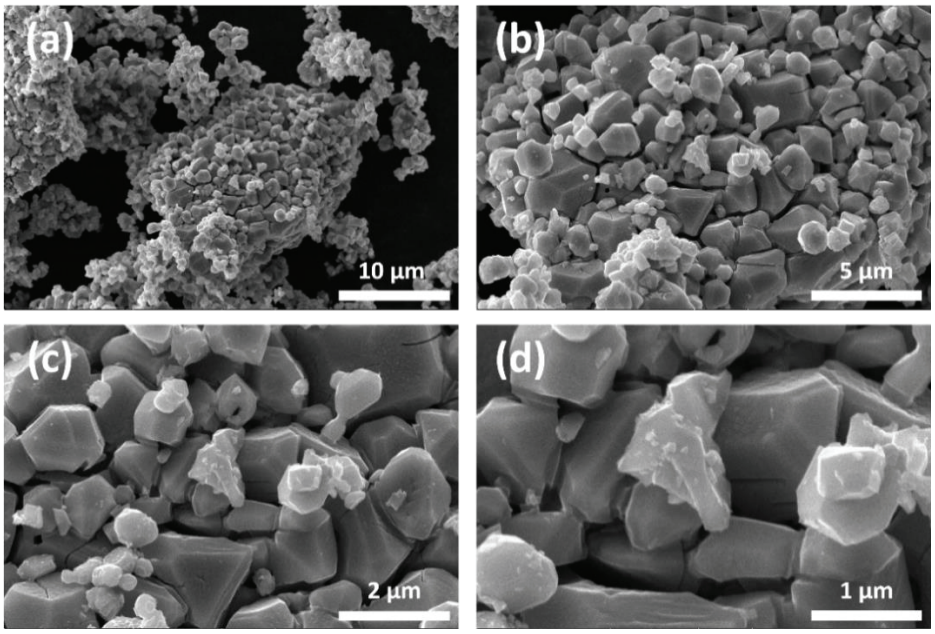

Figure 4.9. SEM images of the λ-MnO_2 powder at (a) 10000, (b) 25000, (c) 50000, (d) 100000 magnifications.

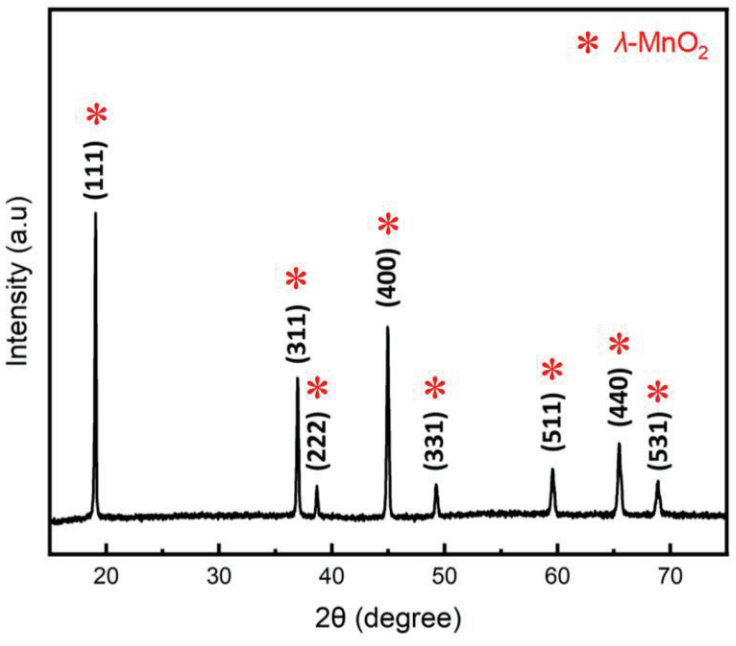

Figure 4.10. XRD patterns of the λ-MnO_2.

XRD pattern of the λ-MnO_2 powder was investigated to obtain structural information (Figure 4.10). The XRD analysis indicated that the observed reflections correspond to the crystalline structure of λ-MnO_2. The diffraction signals observed at an angle of 18.9°, 36.9°, 38.7°, 44.9°, 49.3°, 59.6°, 65.5°, and 68.9° likely correspond to the spinel (λ-MnO_2) phase with (111), (311), (222), (400), (331), (511), (440) and (531) planes, respectively. Spinel (λ-MnO_2) is a polymorph of MnO_2 with a cubic structure.[113] The XRD pattern of λ-MnO_2 is consistent with the results of several studies reported in the literature. For example, Noerochim et al.[130] and Li et al.[131] observed the XRD pattern of λ-MnO_2 in their study and obtained diffraction peaks at the same angles and planes as obtained in this study.

The size distribution of λ-MnO_2 nanoparticles was determined using the dynamic light scattering (DLS) technique. A piece of powder nearly 1 mg of λ-MnO_2 was dispersed in 10 mL of deionized water to obtain the ideal range of sample concentration. Figure 4.11 shows the particle size distribution of λ-MnO_2 nanoparticles. The average particle size diameter was measured to be 525±7 nm.

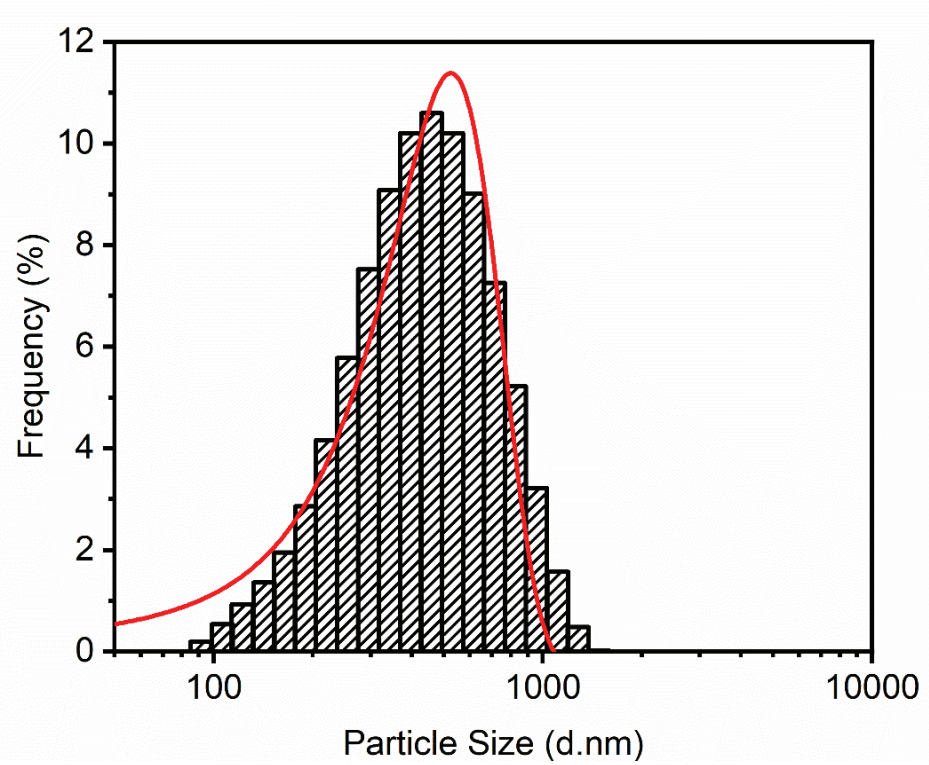

Figure 4.11. Particle size distribution of λ-MnO_2.

The zeta potential of the λ-MnO_2 was measured at different pH levels to understand further the factors influencing sorption at the pH values examined. The zeta potential measurements were conducted following the procedure outlined in the study by Zhang et al.[132] An aliquot of 10 mg of λ-MnO_2 dispersion was prepared with 100 mL of a 1 mmol/L NaCl solution. The pH of the dispersion was then adjusted within 2 to 12 using 0.1 M HCl and NaOH solutions. Figure 4.12 illustrates the changes in zeta potential values across the pH range of 2-12. The results indicated that an increase in pH led to a rise in the negative charge of the particles. This enhanced negative charge may result in a stronger attraction between the particles and the positively charged lithium ions, potentially leading to higher sorption efficiency. This finding is consistent with previous research. Zhang et al.[132] conducted zeta potential measurements on various MnO_2 polymorphs, including λ-MnO_2, at different pH values. Their observations revealed that the surface zeta potentials of all sorbents decreased as a result of the continuous deprotonation effect of surface hydroxyl groups. The isoelectric point of λ-MnO_2 was found as 2.9, similar to the value reported in the existing literature.[132]

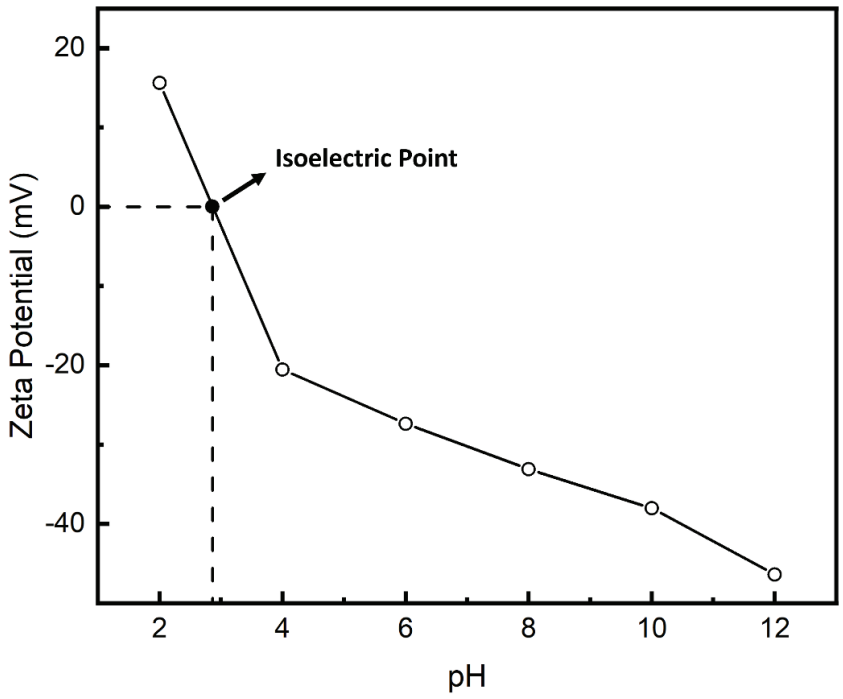

Figure 4.12. Zeta potential of λ-MnO_2 at different pH values.

4.3. Deposition of λ-MnO_2 on Electrospun Mat

The vacuum-assisted deposition procedure was applied to PU electrospun mats and common woven fabrics to compare the λ-MnO_2 retention performance of PU electrospun mats with fabrics. The structures of woven fabrics and PU electrospun before λ-MnO_2 deposition were compared with SEM images (Figure 4.13).

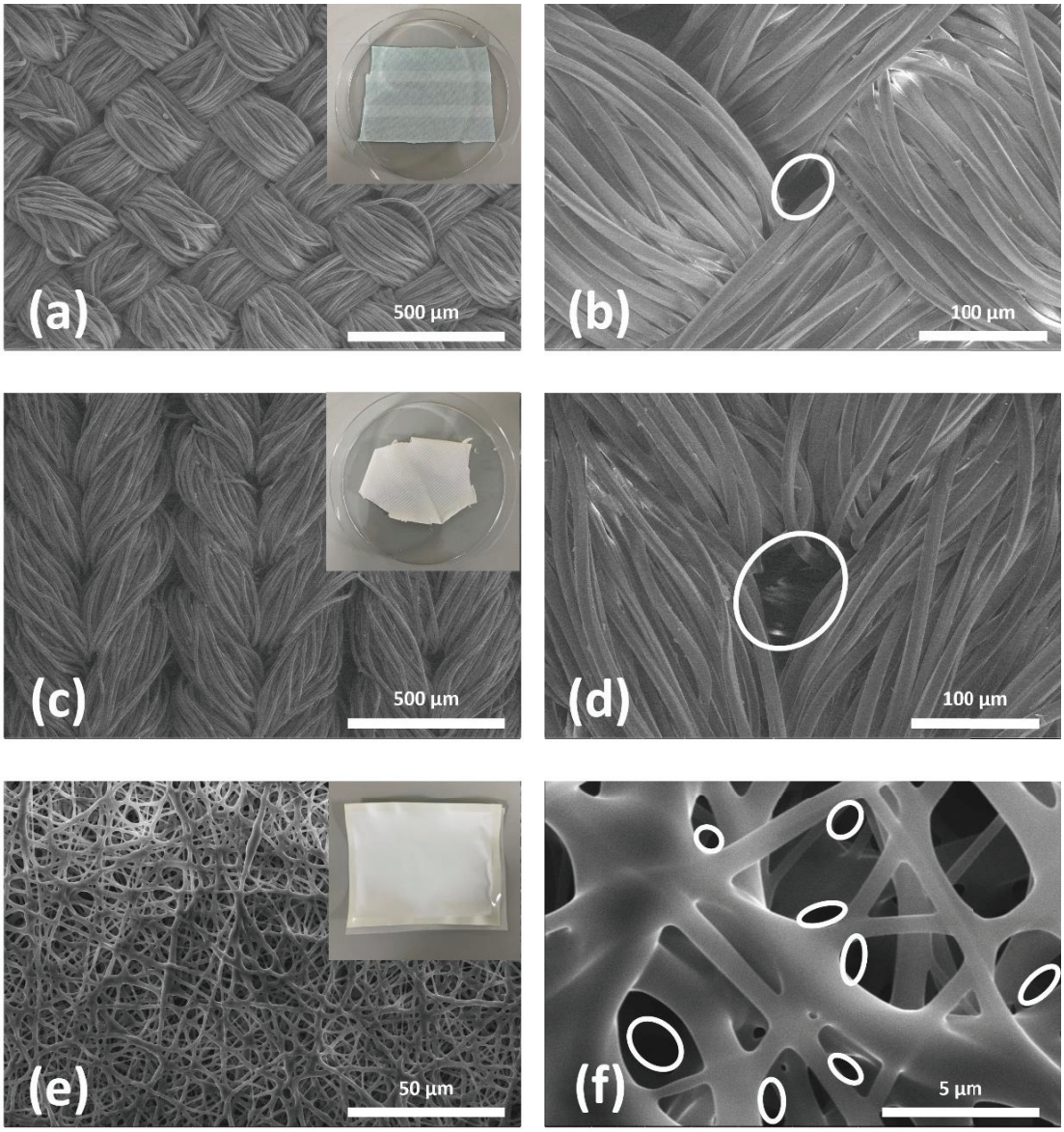

Figure 4.13. SEM images of (a, b, c, d) fabrics and (e, f) electrospun mat.

Since fabrics are woven, they have interstice spaces between weaves, while electrospun mat has interfibrillar spaces between fibers. Areas of interstice and interfibrillar spaces are shown by white circles. Areas of interstice of fabrics and interfibrillar spaces of the electrospun mat were measured by using ImageJ software as 1280, 4400, and 0.185 μm^2, respectively. The interstice areas of fabrics are larger than the interfibrillar areas of electrospun mats due to differences in the manufacturing processes and structural characteristics. Fabrics are typically made by weaving or knitting yarns together, resulting in larger open spaces between the yarns. On the other hand, electrospun mats are composed of randomly deposited nanofibers, which form a dense network with smaller interstitial spaces between the fibers. Therefore, this significant difference between interstice and interfibrillar space is an expected result.

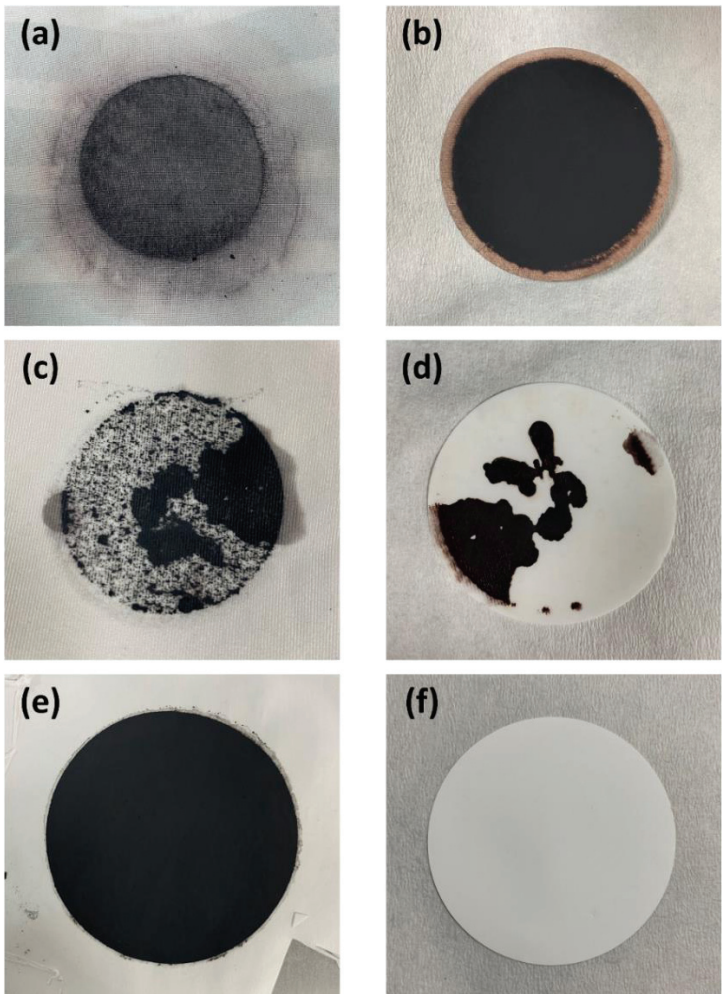

Figure 4.14. Images of (a, c) fabrics, (e) electrospun mat and (b, d, f) filter papers after λ-MnO_2 deposition.

To investigate the λ-MnO_2 retention performance of PU electrospun mats and fabrics, it aimed to deposit an equal amount (100 mg) of λ-MnO_2 into all materials by vacuum-assisted deposition. After the deposition process, the amount of λ-MnO_2 remaining on the fabrics and the electrospun mat was measured and compared. In addition, the filter paper was placed under the fabrics and electrospun mat to see the remaining λ-MnO_2 in decantate passing through on their surfaces. The images of fabrics, electrospun mat, and filter papers after deposition are shown in Figure 4.14. The fabrics could not hold all λ-MnO_2 on their surfaces. The amount of λ-MnO_2 on fabrics and electrospun was measured as 30 (Figure 4.14a), 50 (Figure 4.14c), and 100 mg (Figure 4.14e), respectively. While the electrospun mat accumulated all λ-MnO_2, common fabrics could only accumulate a part of λ-MnO_2. As seen in the SEM images, the observed larger interstice spaces in the fabrics could be attributed to this phenomenon.

4.4. Characterization of λ-MnO_2 Deposited PU Electrospun Mats

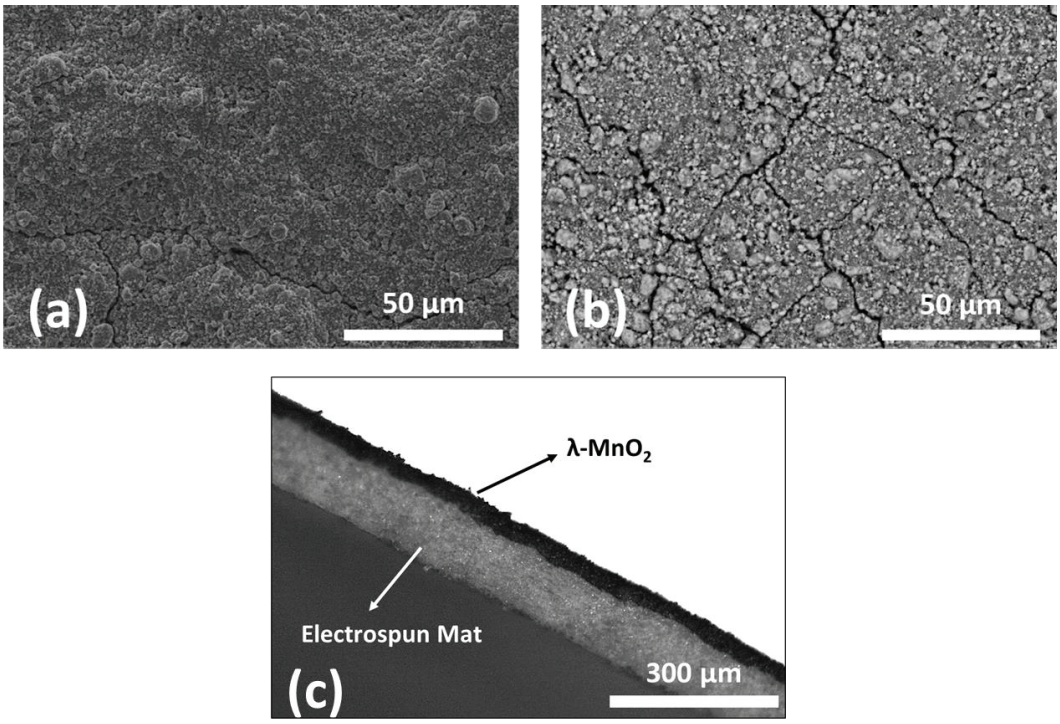

Figure 4.15. SEM images of λ-MnO_2 deposited mats at (a) secondary electron and (b) backscattered electron detector. (c) Cross-section image of the mat.

The λ-MnO_2 deposited PU electrospun mat was examined by SEM using a secondary electron and a backscattered electron detector (Figure 4.15a,b). The SEM images reveal that the particles completely cover the surface of the electrospun mats. The λ-MnO_2 layer formed on the electrospun mat was also clearly observed in the cross-section image (Figure 4.15c). Although larger particles were agglomerated in some parts, the nanoparticles are generally homogeneously distributed on the surface. Moreover, cracks formed on the surface of the dried λ-MnO_2 powder after the vacuum-assisted deposition.

TGA and DSC analysis were made to study the thermal properties of the neat PU electrospun mat and the λ-MnO_2 deposited mat. Figure 4.16 presents the thermogravimetric analysis of the PU electrospun mat and λ-MnO_2 deposited PU electrospun mat performed between room temperature and 610 °C. The weight and derivative of weight are represented on the left and right axes, respectively.

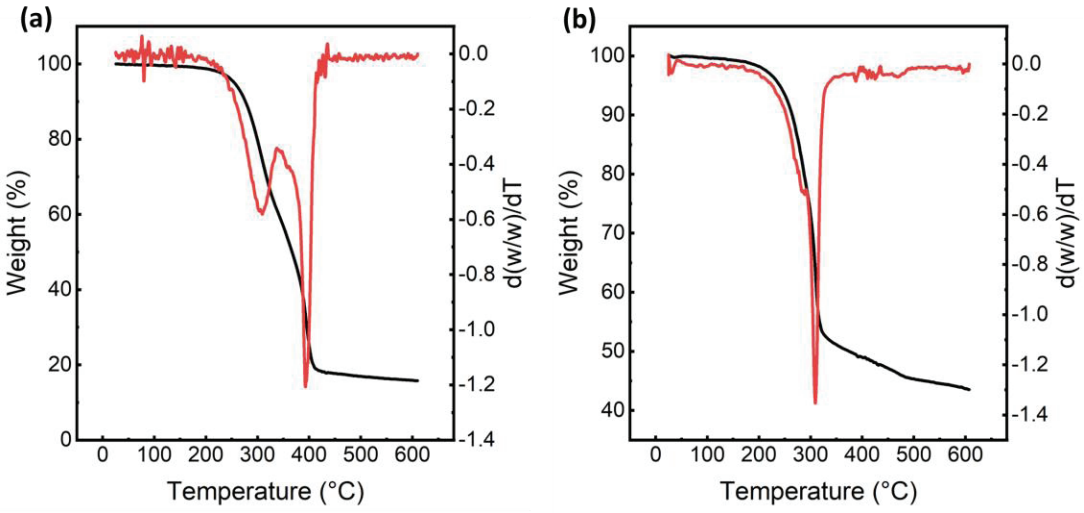

Figure 4.16. Weight (black) and derivative of weight (red) of the (a) PU mat and (b) λ-MnO_2 deposited mat with TGA.

As depicted in Figure 4.16a, a significant drop in the thermogravimetric curve of the neat TPU mat was observed when the temperature reached approximately 250°C, indicating the onset of decomposition for the TPU at this temperature. The DTG curve exhibits two distinct weight losses occurring at different temperatures, suggesting that the

decomposition of the material takes place in two separate stages. The first step of thermal decomposition is the cleavage of urethane bonds at 300 °C, and the second step is the decomposition of soft segments of PU at about 400 °C. These values are consistent with the literature.[133,134] The TGA curve of the λ-MnO_2 deposited PU mat also exhibited the onset of decomposition around 250°C, similar to that observed in the PU mat (Figure 4.16b). However, only one peak at around 300 °C in the DTG curve of λ-MnO_2 deposited TPU nanofiber formed. The addition of λ-MnO_2 affects the decomposition behavior of TPU, possibly causing a change in the decomposition mechanism or altering the material's thermal stability. Moreover, comparing weight losses, the PU mat exhibited 85% weight loss, while λ-MnO_2 deposited mat exhibited 55%.

Differential scanning calorimetry (DSC) analysis was made with PU electrospun mat and λ-MnO_2 deposited mat to verify the phase separation behavior of TPU. The thermograms (Figure 4.17) of the PU mat and λ-MnO_2 deposited mat revealed two distinct glass transition points at -40 °C ($T_{g,SS}$) and at 75 °C ($T_{g,HS}$) of the TPU attributed to soft and hard segments, respectively.

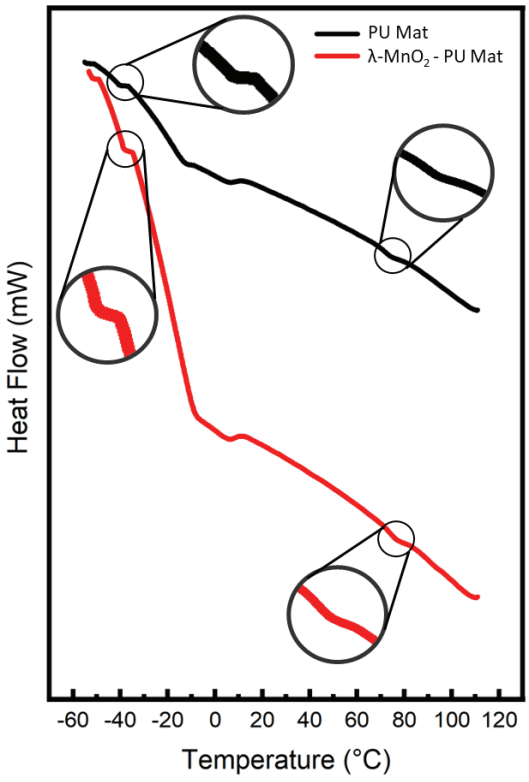

Figure 4.17. DSC thermogram of the PU electrospun mat (black) and λ-MnO_2 deposited mat (red).

The obtained glass transition values are consistent with those reported in the study of Yahiaoui et al.[135] Moreover, it was observed that there was a different signal at about 5 °C on the thermogram. This observation can be linked to the melting temperature of the TPU's soft segment, as reported in the research of Silva et al.[136] On the other hand, this peak may have originated from impurity or from the evaporation of residual solvent trapped within the fibers.

4.5. Lithium Extraction Experiments

4.5.1. Effect of λ-MnO_2 Amount

The effect of the amount of λ-MnO_2 deposited on the PU mats on the lithium extraction performance is given in Figure 4.18.

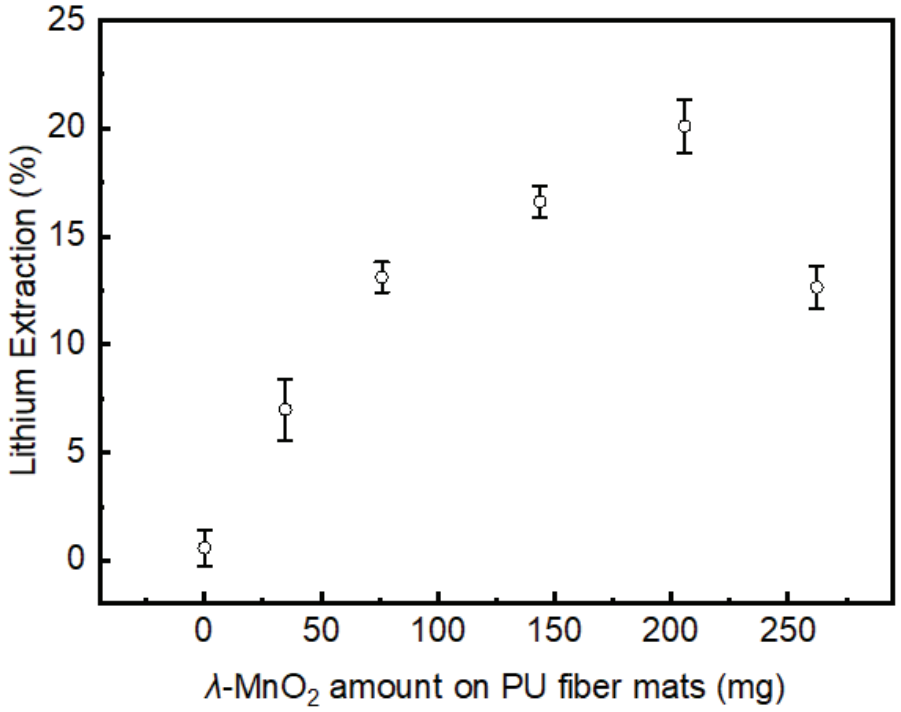

Figure 4.18. λ-MnO_2 amount on PU mats vs. Li^+ extraction (C_0=200 mg/L, pH=12 at RT).

Based on the experimental results, an increase in the adsorbent amount on the PU mat from 35 mg to 200 mg resulted in an enhancement of Li^+ extraction from the solution by up to 20.1%. However, it was noted that the Li^+ extraction declined as the amount of adsorbent was further increased. Initially, raising the amount of λ-MnO_2 on the electrospun mats may have led to an increase in the surface area for lithium adsorption. This can have enhanced the lithium extraction efficiency as more active sites were exposed to the solution. The decline in lithium extraction performance observed with adding more λ-MnO_2 may be attributed to a threshold point where the increased amount of λ-MnO_2 starts hindering the accessibility of lithium ions to the active sites. Furthermore, excessive deposition can form a densely packed layer or agglomerates, which can hinder the diffusion of lithium ions between the adsorbent materials. Consequently, extraction efficiency is reduced. Simultaneously, it was seen that the PU mat without λ-MnO_2 deposition did not exhibit any lithium extraction.

4.5.2. Effect of Initial Li^+ Concentration

The relationship between the initial Li^+ concentration of the solution and the lithium extraction efficiency of λ-MnO_2 deposited PU mats is depicted in Figure 4.19. The lithium extraction exhibited an upward trend as the Li^+ concentration of the filtered solution increased. The lithium extraction achieved a maximum value of 22.3% at a concentration of 250 mg/L. More lithium ions are present in the solution for adsorption with a higher initial Li^+ concentration. This means that a more significant number of adsorption sites on the surface of the adsorbent material can be occupied by lithium ions, leading to increased lithium extraction. These findings align with the results reported in a previous study. An increasing trend in lithium extraction with increasing initial Li^+ concentration was also seen in the study of Özmal and Erdoğan[137]. The explanation for this phenomenon lies in the two-step sorption process of ion sieves, which involves boundary layer diffusion and intraparticle diffusion. When the initial concentration of lithium is increased, the surface of the ion sieve comes into contact with a greater amount of lithium. This is attributed to the enhanced diffusion of Li^+ through the boundary layer within a given unit of time.[137]

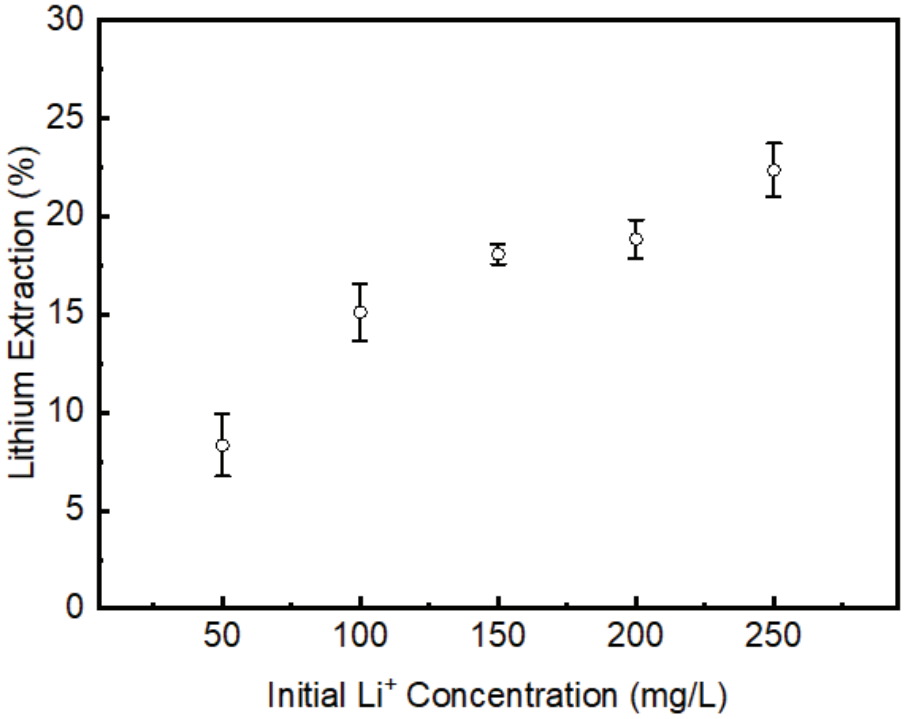

Figure 4.19. Initial Li^+ concentration vs. Li^+ extraction (pH=12 at RT).

4.5.3. Effect of Solution pH

Figure 4.20 shows the lithium extraction performance of the λ-MnO_2 deposited PU mats at various pH of the solution. As the pH value of the Li^+ solution used in the filtration process increased, a significant increase was observed in the extraction of lithium. The highest lithium extraction for λ-MnO_2 deposited PU mat was achieved at pH 12 with a value of 20.5%. It has been observed in the zeta potential measurements that the λ-MnO_2 adsorbent became more negatively charged due to the deprotonation of surface functional groups as the pH increased. Thus, an increase in negative charge can enhance the electrostatic attraction between the negatively charged λ-MnO_2 surface and the positively charged Li^+ ions in the solution, facilitating their adsorption. The stronger electrostatic interactions at high pH values can provide to enhance lithium extraction performance. The results obtained are consistent with the results in the literature. For example, the study of Shi et al.[138] observed that the adsorption performance of lithium ion-sieves increased in highly alkaline solutions.

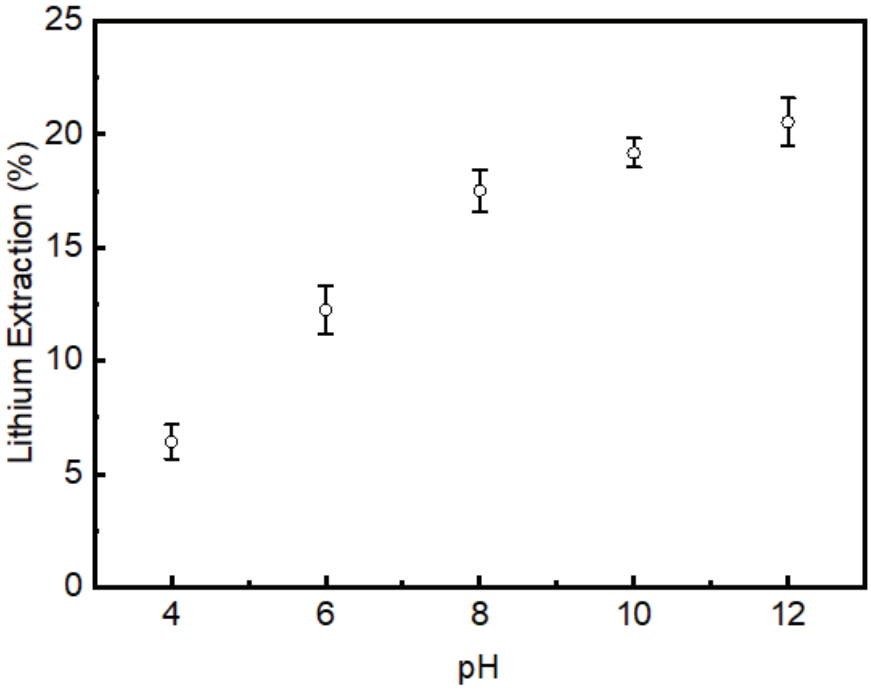

Figure 4.20. Solution pH vs. Li^+ extraction (C_0=200 mg/L at RT).

4.5.4. Effect of Fiber Diameter

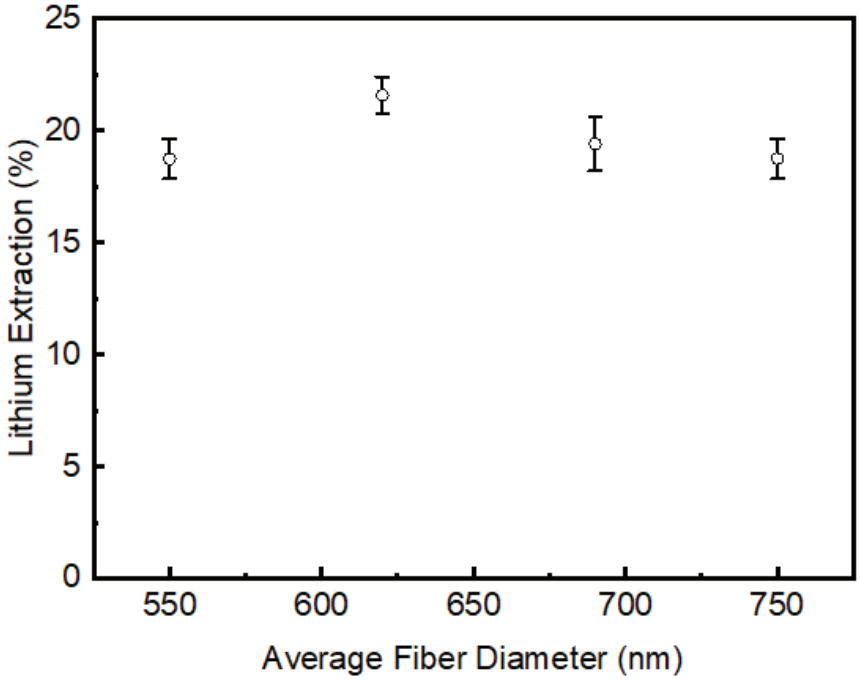

Figure 4.21. AFD vs. Li^+ extraction (C_0=200 mg/L, pH=12 at RT).

The effect of the average fiber diameter of the λ-MnO_2 deposited PU mats on the lithium extraction performance is given in Figure 4.21. The experiments revealed that the AFD of the λ-MnO_2 deposited PU mats did not significantly impact the lithium extraction. The deposition of λ-MnO_2 on the PU mats may exhibit a uniform distribution regardless of the fiber, as observed in the SEM images. It was expected that the fiber diameter did not strongly affect the lithium extraction performance when the particles were evenly coated on the electrospinning mat surface. This uniform deposition may allow for consistent interaction between the manganese oxide particles and lithium ions, resulting in similar lithium extraction efficiency.

4.5.5. Stacked λ-MnO_2 Deposited PU Electrospun Mats

Figure 4.22 demonstrates the lithium extraction change as the layer number of stacked λ-MnO_2 deposited PU mats was increased.

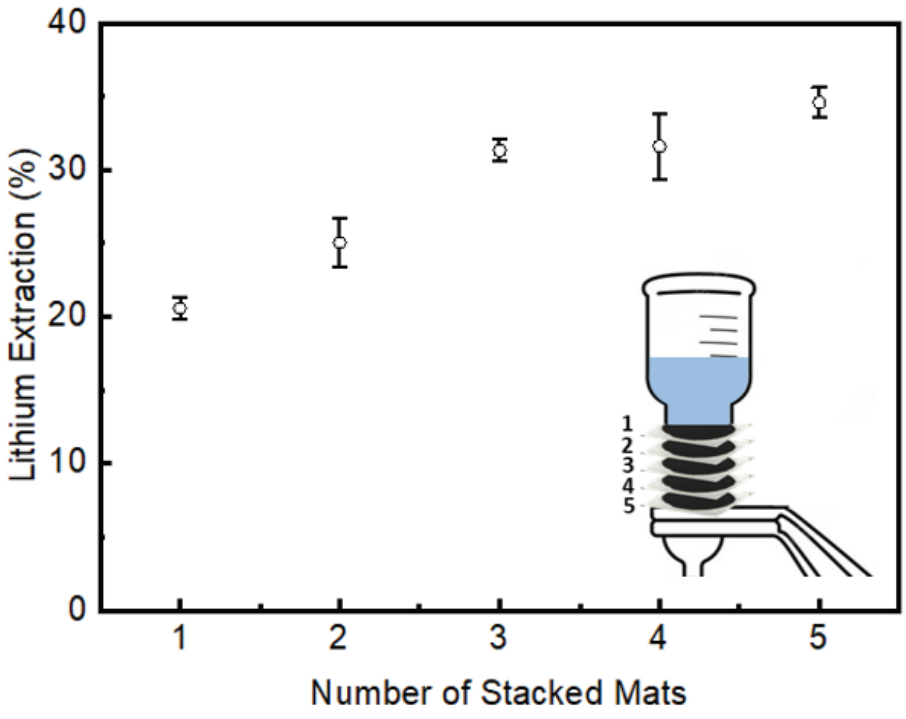

Figure 4.22. Number of stacked PU mats vs. Li^+ extraction (C_0=200 mg/L, pH=12 at RT).

As the number of layers stacked enhanced, improvement was observed in the extraction of lithium. The lithium extraction, which was 20.6% when a single λ-MnO_2 deposited PU mat was used, reached 34.6% when five λ-MnO_2 deposited PU mats were stacked. However, this upward trend did not occur proportionally, and lithium extraction did not increase as much as expected. This may have been due to interference between adjacent mats when multiple mats are stacked. Thus, the solution's access to the adsorption sites can be limited. Moreover, increasing the number of layers can create channels or paths through which the aqueous Li^+ solution can bypass some layers of the electrospun mats. This can cause incomplete contact between solution and λ-MnO_2 particles, reducing the overall efficiency of lithium extraction.

4.5.6. Multi-Stage Filtration

The variation of cumulative lithium extraction of the λ-MnO_2 deposited PU mats when a multi-stage filtration process was applied is shown in Figure 4.23. The cumulative lithium extraction increased significantly at each filtration step. At the end of the 5^{th} filtration stage, the cumulative lithium extraction reached a value of 56.2%. As the lithium solution passed through each stage of the filtration process, it came into contact with a fresh surface of the manganese oxide deposited electrospun mat. This may have ensured that the adsorption sites on the mats were efficiently utilized since they were not saturated from exposure to the lithium solution. Therefore, the adsorption sites on each mat may have efficiently captured and eliminated lithium ions by employing multiple stages. This has resulted in enhanced cumulative lithium extraction performance. On the other hand, as lithium ions were removed from the solution at each step, the concentration of the solution decreased. This reduction made lithium extraction more difficult at each stage. Therefore, less lithium was removed at each step, although cumulative lithium extraction increased at each step. At some point, the cumulative lithium extraction may not increase noticeably due to the paucity of lithium in the solution and may reach a plateau. The experiment was repeated by increasing the number of stages to see this plateau. The cumulative lithium extraction was aimed to be raised by using solutions with different initial lithium concentrations.

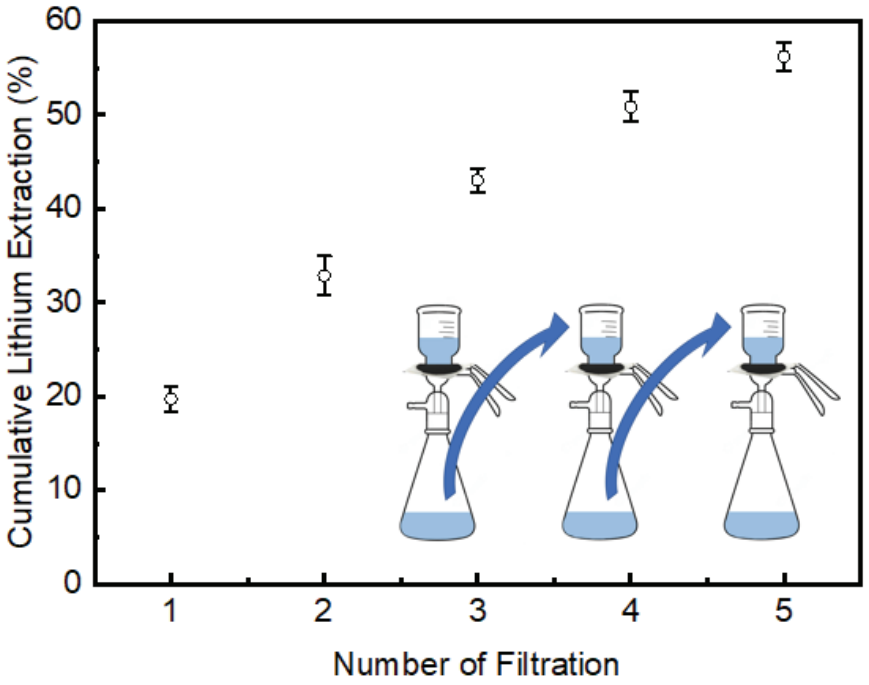

Figure 4.23. Number of filtrations vs. Cumulative Li^+ extraction (C_0=200 mg/L, pH=12 at RT).

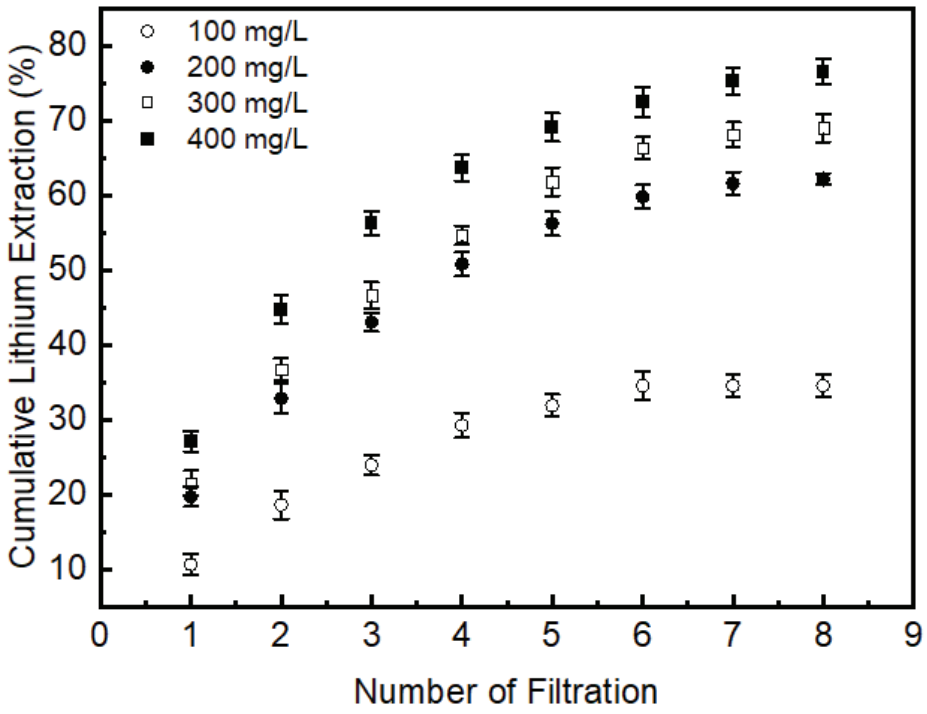

Figure 4.24. Number of filtrations vs. Cumulative Li^+ extraction with various initial Li^+ concentrations (pH=12 at RT).

Figure 4.24 illustrates the relationship between the initial Li^+ concentration and the cumulative lithium extraction of the λ-MnO_2 deposited PU mats during the multi-stage filtration process. As expected, the cumulative lithium extraction reached higher values when the initial Li^+ concentration was increased. At the end of the 8th filtration, cumulative lithium extraction had reached 34.6%, 56.2%, 68.9%, and 76.6% for initial Li^+ concentration of 100, 200, 300, and 400 mg/L, respectively. At the initial concentration of 100 mg/L, the lithium concentration reduction occurred earlier than other solutions, resulting in no change of cumulative lithium extraction after the 6th stage. Furthermore, the higher initial concentrations of lithium provide a larger number of available Li^+ ions for adsorption. Therefore, as the filtration progresses through multiple stages, the cumulative extraction of lithium continues to increase without reaching a plateau.

4.5.7. Salt Lake Brine

The initial concentrations of some ions in salt lake brine were measured before filtration experiments were performed, shown in Table 4.1.

Table 4.1. Elemental composition of salt lake brine

Elements	**Concentration (mg/L)**
Sodium	110,260
Magnesium	18,000
Potassium	10,240
Calcium	1,290
Lithium	210
Strontium	60

Sodium is the main component of sodium chloride and is naturally abundant in salt lake environments. Therefore, as expected, brine has a relatively high sodium concentration. In addition, brine is rich in magnesium and potassium ions. The

concentration of lithium in salt lake brine, which was measured as 210 mg/L, can be considered a moderate value. Apart from lithium, strontium, which is one of the critical raw materials, is also present in the system with a concentration of 60 mg/L.

The effect of the amount of λ-MnO_2 deposited on the PU mats on the lithium extraction performance in salt lake brine is given in Figure 4.25. The lithium extraction exhibited an upward trend as the adsorbent amount on the PU mat increased, as in the experiment made with synthetic Li^+ solution. However, lithium extraction in the synthetic solution was 20.1% when the adsorbent amount on the PU mat was 200 mg, while it was 13.8% in natural brine.

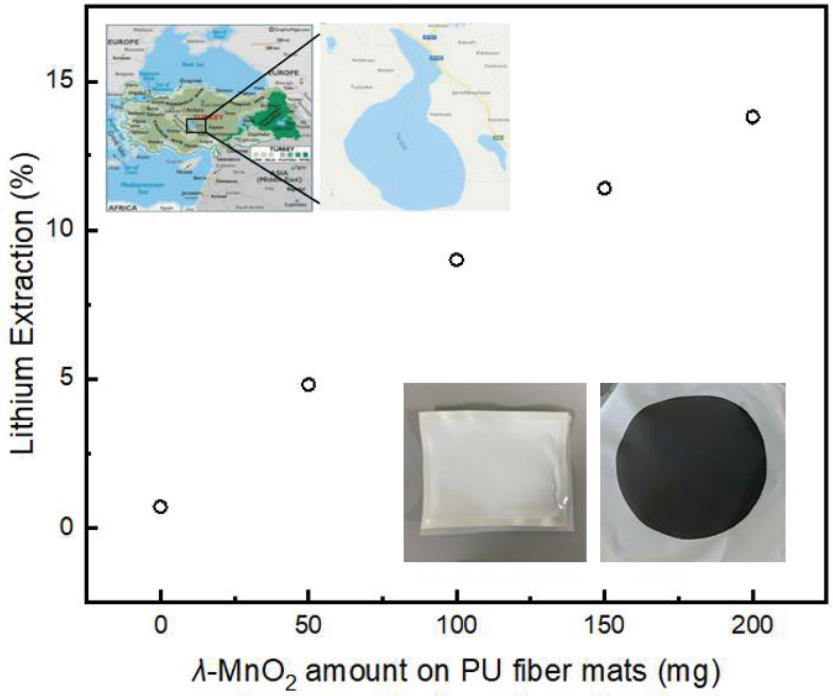

Figure 4.25. λ-MnO_2 amount on PU mats vs. Li^+ extraction (C_0=210 mg/L, pH=7.5 at RT) using natural brine obtained from Lake Tuz.

One possible reason for less lithium extraction is the presence of other ions in the salt lake brine. The high concentration of various ions (Na^+, Mg^{2+}, Ca^{2+}, K^+) in the salt lake brine may hinder the adsorption of lithium ions, leading to a lower extraction efficiency than the synthetic solutions. The concentration of Na^+, Mg^{2+}, Ca^{2+}, and K^+ in the salt lake brine is relatively high, so they can outcompete lithium ions for available

adsorption sites, reducing the overall lithium extraction percentage. Especially magnesium ions, which have a similar chemical composition and ionic radius to lithium ions, pose challenges to the adsorption process.[81] The salt lake brine used in the experiment had an Mg^{2+}/Li^{+} ratio of 85, so this extraction reduction is consistent with the literature. Moreover, Wang et al.[139] conducted experiments on selective lithium recovery from geothermal water using λ-MnO_2. They found that the adsorption performance was favorable in synthetic lithium solutions. However, when tested against real geothermal brines, the adsorption capacity of λ-MnO_2 decreased.

CHAPTER 5

CONCLUSIONS

Lithium is used in many fields, especially rechargeable batteries, due to its high energy density and unique electrochemical properties. There has been a substantial increase in demand for lithium in the market recently, with the use of electric vehicles expected to increase further. To meet this increasing demand, obtaining lithium quickly and efficiently from lithium sources is necessary. Lithium extraction by mining from lithium reserves is both an environmentally harmful and unsustainable process, as the reserves will be depleted. For this reason, research on lithium recovery from natural water resources has increased in recent years. The adsorption method is the most widely used and promising method for lithium recovery from water sources. Among adsorbents, spinel-type manganese oxides (λ-MnO_2) are extremely attractive due to their high affinity for lithium. However, it has been observed that the powder structure of the adsorbent material is not suitable for industrial use. Using adsorbent materials together with a polymeric substrate or binder materials instead of using them in powder form can eliminate this disadvantage. Nanofibers are unique materials widely used as substrates in various applications, with high porosity, high surface area, good permeability, high encapsulation efficiency, high chemical and thermal stability, controllable morphology, and enhanced physical and mechanical properties. Electrospinning is a method for creating polymer nanofibers with sizes between nanometers and micrometers. It has the capacity to work with a wide range of polymers, control processability, and generate nanofibers with high surface area and controllable pore structure.

In this thesis, it was aimed to fabricate flexible and free-standing electrospun mat substrates and combine them with λ-MnO_2 to extract lithium from aqueous systems. TPU has been used to produce electrospun mats due to its good spinnability, water resistance, and flexibility. First, PU solutions were prepared at various concentrations in solvents of DMF and/or THF and DMF:THF ratios to observe the effect of concentration and solvent ratio on the structure of electrospun fibers and determine the optimal conditions. The characterization of fabricated electrospun fibers was carried out using SEM, and a phase diagram of PU fiber morphology due to both parameters was designed. The optimal

conditions for bead-free and smooth fibers with AFD of 729±23 nm were determined as a 1:2 solvent ratio by volume (DMF:THF = 1:2) at 30 wt% PU concentrations. In addition, the effects of concentration, flow rate, and TCD on AFD were also examined. As the concentration increased, there was an observed increase in AFD. However, AFD decreased as the flow rate and electric field increased.

In the second part, the characterizations of λ-MnO_2 and λ-MnO_2 deposited PU mats were carried out. The XRD analysis of the λ-MnO_2 powder indicated that the observed reflections correspond to the crystalline structure of spinel type λ-MnO_2 ion-sieve. Moreover, zeta potential measurements showed that an increase in pH led to a rise in the negative charge of the particles. The λ-MnO_2 powder retention performance of electrospun mats was investigated by deposition of λ-MnO_2 by vacuum vacuum-assisted deposition. Electrospun mat accumulated all adsorbent due to their dense and small interfibrillar spaces. TGA and DSC analysis were made to investigate the thermal properties of the neat PU electrospun mat and the λ-MnO_2 deposited mat. It was observed that the addition of λ-MnO_2 affected the decomposition behavior of TPU, possibly causing a change in the decomposition mechanism. The phase separation behavior of TPU was verified by finding two distinct glass transition points at -40 °C and 75 °C of the TPU attributed to soft and hard segments, respectively.

In the last part of the study, lithium extraction experiments of λ-MnO_2 deposited PU electrospun mats using synthetic lithium solutions and salt lake brine. The effect of the amount of λ-MnO_2 deposited on the PU mats on the lithium extraction performance was investigated in the range of 35-265 mg and it was observed that Li^+ extraction reached 20.1% when the adsorbent amount was 200 mg. When the effect of the initial concentration of Li^+ was investigated, the lithium extraction exhibited an upward trend as the Li^+ concentration of the filtered solution increased with the lithium extraction of 22.3% at a concentration of 250 mg/L. In the pH study, the lithium extraction of the λ-MnO_2 deposited PU mats increased with increasing pH due to the deprotonation of the surface hydroxyl groups, and the lithium extraction of 20.5% was obtained at pH 12. The effect of AFD of the λ-MnO_2 deposited PU mats on lithium extraction was also studied, but it was revealed that it had no significant impact. To improve the lithium extraction performance of λ-MnO_2 deposited PU mats, they were used separately as stacked layer by layer and in multi-stage filtration. While the lithium extraction reached 34.6% when five layers of mats were stacked, the cumulative lithium extraction reached a value of 56.2% at the end of the 5^{th} filtration stage in multi-stage filtration. Moreover, when the

initial concentration of Li^+ solution increased to 400 mg/L, cumulative lithium extraction reached 76.6% at the end of the 8th filtration. Finally, lithium extraction experiments with salt lake brine containing various ions (Na^+, Mg^{2+}, Ca^{2+}, K^+) in high concentrations showed that these ions reduced the lithium extraction percentage of λ-MnO_2 deposited PU mats. Lithium extraction has been found as 13.8%.

As a result of the studies, the PU electrospun mats as a substrate for λ-MnO_2 powder were found as a promising candidate for practical use in lithium extraction from aqueous systems with its flexibility, free-standing structure, and water resistivity. Lithium extraction performance can be improved in the next step of the studies by increasing the amount of λ-MnO_2 powder that electrospun mats can retain or by arranging a different experimental design.

REFERENCES

(1) Stringfellow, W. T.; Dobson, P. F. Technology for the Recovery of Lithium from Geothermal Brines. *Energies*. 2021. https://doi.org/10.3390/en14206805.

(2) Swain, B. Recovery and Recycling of Lithium: A Review. *Separation and Purification Technology*. 2017. https://doi.org/10.1016/j.seppur.2016.08.031.

(3) Xu, P.; Hong, J.; Qian, X.; Xu, Z.; Xia, H.; Tao, X.; Xu, Z.; Ni, Q. Q. Materials for Lithium Recovery from Salt Lake Brine. *Journal of Materials Science*. 2021. https://doi.org/10.1007/s10853-020-05019-1.

(4) Liu, G.; Zhao, Z.; Ghahreman, A. Novel Approaches for Lithium Extraction from Salt-Lake Brines: A Review. *Hydrometallurgy* **2019**, *187*. https://doi.org/10.1016/j.hydromet.2019.05.005.

(5) Ambrose, H.; Kendall, A. Understanding the Future of Lithium: Part 1, Resource Model. *J Ind Ecol* **2020**, *24* (1). https://doi.org/10.1111/jiec.12949.

(6) Khalil, A.; Mohammed, S.; Hashaikeh, R.; Hilal, N. Lithium Recovery from Brine: Recent Developments and Challenges. *Desalination*. 2022. https://doi.org/10.1016/j.desal.2022.115611.

(7) Murodjon, S.; Yu, X.; Li, M.; Duo, J.; Deng, T. Lithium Recovery from Brines Including Seawater, Salt Lake Brine, Underground Water and Geothermal Water. In *Thermodynamics and Energy Engineering*; 2020. https://doi.org/10.5772/intechopen.90371.

(8) Chitrakar, R.; Kanoh, H.; Miyai, Y.; Ooi, K. Recovery of Lithium from Seawater Using Manganese Oxide Adsorbent (H1.6Mn1.6O4) Derived from Li1.6Mn1.6O4. *Ind Eng Chem Res* **2001**, *40* (9). https://doi.org/10.1021/ie000911h.

(9) Weng, D.; Duan, H.; Hou, Y.; Huo, J.; Chen, L.; Zhang, F.; Wang, J. Introduction of Manganese Based Lithium-Ion Sieve-A Review. *Progress in Natural Science: Materials International*. 2020. https://doi.org/10.1016/j.pnsc.2020.01.017.

(10) Emad Abdoluosefi, H.; Honarasa, G. Fabrication of Polyurethane and Thermoplastic Polyurethane Nanofiber by Controlling the Electrospinning Parameters. *Mater Res Express* **2017**, *4* (10). https://doi.org/10.1088/2053-1591/aa9191.

(11) Lou, L.; Osemwegie, O.; Ramkumar, S. S. Functional Nanofibers and Their Applications. *Ind Eng Chem Res* **2020**, *59* (13). https://doi.org/10.1021/acs.iecr.9b07066.

(12) Anusiya, G.; Jaiganesh, R. A Review on Fabrication Methods of Nanofibers and a Special Focus on Application of Cellulose Nanofibers. *Carbohydrate Polymer Technologies and Applications* **2022**, *4*, 100262. https://doi.org/10.1016/j.carpta.2022.100262.

(13) Jin, S.; Xin, B.; Kan, C. W. Electrospun Nanofibers and Applications: A Review. *AATCC Journal of Research*. 2020. https://doi.org/10.14504/ajr.7.3.4.

(14) Demir, M. M.; Yilgor, I.; Yilgor, E.; Erman, B. Electrospinning of Polyurethane Fibers. *Polymer (Guildf)* **2002**, *43* (11). https://doi.org/10.1016/S0032-3861(02)00136-2.

(15) Bhardwaj, N.; Kundu, S. C. Electrospinning: A Fascinating Fiber Fabrication Technique. *Biotechnology Advances*. 2010. https://doi.org/10.1016/j.biotechadv.2010.01.004.

(16) Çelik, A.; Topçu, G.; Isik, T.; Baba, A.; Horzum, N.; Demir, M. M. Investigation of Lithium Sorption Efficiency Using Swcnt Functionalized Electrospun Fiber Mats from the Hypersaline Geothermal Brine. In *Materials Science Forum*; 2018; Vol. 915. https://doi.org/10.4028/www.scientific.net/MSF.915.121.

(17) Acik, G. A Comprehensive Study on Electrospinning of Poly (Vinyl Alcohol): Effects of the TCD, Applied Voltage, Flow Rate and Solution Concentration. *Journal of the Turkish Chemical Society Section A: Chemistry* **2020**. https://doi.org/10.18596/jotcsa.741452.

(18) Chew, S.; Wen, Y.; Dzenis, Y.; Leong, K. The Role of Electrospinning in the Emerging Field of Nanomedicine. *Curr Pharm Des* **2006**, *12* (36). https://doi.org/10.2174/138161206779026326.

(19) Long, Y. Z.; Yan, X.; Wang, X. X.; Zhang, J.; Yu, M. Electrospinning: The Setup and Procedure. *Electrospinning: Nanofabrication and Applications* **2019**.

(20) Rahei, S.; Maghsoodloo, S.; Saberi, M.; Lotfi, S.; Motaghttalab, V.; Noroozi, B.; Haghi, A. K. New Horizons in Modeling and Simulation of Electrospun Nanofibers: A Detailed Review. *Cellulose Chemistry and Technology*. 2014.

(21) Duan, Y.; Kalluri, L.; Satpathy, M.; Duan, Y. Effect of Electrospinning Parameters on the Fiber Diameter and Morphology of PLGA Nanofibers. *Dental Oral Biology and Craniofacial Research* **2021**. https://doi.org/10.31487/j.dobcr.2021.02.04.

(22) Beachley, V.; Wen, X. Effect of Electrospinning Parameters on the Nanofiber Diameter and Length. *Materials Science and Engineering C* **2009**, *29* (3). https://doi.org/10.1016/j.msec.2008.10.037.

(23) Ki, C. S.; Baek, D. H.; Gang, K. D.; Lee, K. H.; Um, I. C.; Park, Y. H. Characterization of Gelatin Nanofiber Prepared from Gelatin-Formic Acid Solution. *Polymer (Guildf)* **2005**, *46* (14). https://doi.org/10.1016/j.polymer.2005.04.040.

(24) Chong, E. J.; Phan, T. T.; Lim, I. J.; Zhang, Y. Z.; Bay, B. H.; Ramakrishna, S.; Lim, C. T. Evaluation of Electrospun PCL/Gelatin Nanofibrous Scaffold for Wound Healing and Layered Dermal Reconstitution. *Acta Biomater* **2007**, *3* (3 SPEC. ISS.). https://doi.org/10.1016/j.actbio.2007.01.002.

(25) Van-Pham, D. T.; Thi Bich Quyen, T.; van Toan, P.; Nguyen, C. N.; Ho, M. H.; van Hong Thien, D. Temperature Effects on Electrospun Chitosan Nanofibers. *Green Processing and Synthesis* **2020**, *9* (1). https://doi.org/10.1515/gps-2020-0050.

(26) Park, B. K.; Um, I. C. Effect of Relative Humidity on the Electrospinning Performance of Regenerated Silk Solution. *Polymers (Basel)* **2021**, *13* (15). https://doi.org/10.3390/polym13152479.

(27) de Vrieze, S.; van Camp, T.; Nelvig, A.; Hagström, B.; Westbroek, P.; de Clerck, K. The Effect of Temperature and Humidity on Electrospinning. *J Mater Sci* **2009**, *44* (5). https://doi.org/10.1007/s10853-008-3010-6.

(28) Yang, G. Z.; Li, H. P.; Yang, J. H.; Wan, J.; Yu, D. G. Influence of Working Temperature on The Formation of Electrospun Polymer Nanofibers. *Nanoscale Res Lett* **2017**, *12* (1). https://doi.org/10.1186/s11671-016-1824-8.

(29) Haider, A.; Haider, S.; Kang, I. K. A Comprehensive Review Summarizing the Effect of Electrospinning Parameters and Potential Applications of Nanofibers in Biomedical and Biotechnology. *Arabian Journal of Chemistry*. 2018. https://doi.org/10.1016/j.arabjc.2015.11.015.

(30) Isık, T.; Demir, M. M. Tailored Electrospun Fibers from Waste Polystyrene for High Oil Adsorption. *Sustainable Materials and Technologies* **2018**, *18*. https://doi.org/10.1016/j.susmat.2018.e00084.

(31) Rwei, S. P.; Huang, C. C. Electrospinning PVA Solution-Rheology and Morphology Analyses. *Fibers and Polymers* **2012**, *13* (1). https://doi.org/10.1007/s12221-012-0044-9.

(32) Liu, W.; Huang, C.; Jin, X. Electrospinning of Grooved Polystyrene Fibers: Effect of Solvent Systems. *Nanoscale Res Lett* **2015**, *10* (1). https://doi.org/10.1186/s11671-015-0949-5.

(33) Uyar, T.; Besenbacher, F. Electrospinning of Uniform Polystyrene Fibers: The Effect of Solvent Conductivity. *Polymer (Guildf)* **2008**, *49* (24). https://doi.org/10.1016/j.polymer.2008.09.025.

(34) Lin, J.; Ding, B.; Jianyong, Y.; Hsieh, Y. Direct Fabrication of Highly Nanoporous Polystyrene Fibers via Electrospinning. *ACS Appl Mater Interfaces* **2010**, *2* (2). https://doi.org/10.1021/am900736h.

(35) Zong, X.; Kim, K.; Fang, D.; Ran, S.; Hsiao, B. S.; Chu, B. Structure and Process Relationship of Electrospun Bioabsorbable Nanofiber Membranes. *Polymer (Guildf)* **2002**, *43* (16). https://doi.org/10.1016/S0032-3861(02)00275-6.

(36) Megelski, S.; Stephens, J. S.; Bruce Chase, D.; Rabolt, J. F. Micro- and Nanostructured Surface Morphology on Electrospun Polymer Fibers. *Macromolecules* **2002**, *35* (22). https://doi.org/10.1021/ma020444a.

(37) Akduman, C.; Kumbasar, E. P. A. Electrospun Polyurethane Nanofibers. In *Aspects of Polyurethanes*; 2017. https://doi.org/10.5772/intechopen.69937.

(38) Haghi, A. K.; Akbari, M. Trends in Electrospinning of Natural Nanofibers. In *Physica Status Solidi (A) Applications and Materials Science*; 2007; Vol. 204. https://doi.org/10.1002/pssa.200675301.

(39) Gupta, P.; Elkins, C.; Long, T. E.; Wilkes, G. L. Electrospinning of Linear Homopolymers of Poly(Methyl Methacrylate): Exploring Relationships between Fiber Formation, Viscosity, Molecular Weight and Concentration in a Good Solvent. *Polymer (Guildf)* **2005**, *46* (13). https://doi.org/10.1016/j.polymer.2005.04.021.

(40) Hohman, M. M.; Shin, M.; Rutledge, G.; Brenner, M. P. Electrospinning and Electrically Forced Jets. II. Applications. *Physics of Fluids* **2001**, *13* (8). https://doi.org/10.1063/1.1384013.

(41) Matabola, K. P.; Moutloali, R. M. The Influence of Electrospinning Parameters on the Morphology and Diameter of Poly(Vinyledene Fluoride) Nanofibers- Effect of Sodium Chloride. *J Mater Sci* **2013**, *48* (16). https://doi.org/10.1007/s10853-013-7341-6.

(42) Zhang, C.; Yuan, X.; Wu, L.; Han, Y.; Sheng, J. Study on Morphology of Electrospun Poly(Vinyl Alcohol) Mats. *Eur Polym J* **2005**, *41* (3). https://doi.org/10.1016/j.eurpolymj.2004.10.027.

(43) Yuan, X. Y.; Zhang, Y. Y.; Dong, C.; Sheng, J. Morphology of Ultrafine Polysulfone Fibers Prepared by Electrospinning. *Polym Int* **2004**, *53* (11). https://doi.org/10.1002/pi.1538.

(44) Wannatong, L.; Sirivat, A.; Supaphol, P. Effects of Solvents on Electrospun Polymeric Fibers: Preliminary Study on Polystyrene. *Polym Int* **2004**, *53* (11). https://doi.org/10.1002/pi.1599.

(45) Zuo, W.; Zhu, M.; Yang, W.; Yu, H.; Chen, Y.; Zhang, Y. Experimental Study on Relationship between Jet Instability and Formation of Beaded Fibers during Electrospinning. *Polym Eng Sci* **2005**, *45* (5). https://doi.org/10.1002/pen.20304.

(46) Casper, C. L.; Stephens, J. S.; Tassi, N. G.; Chase, D. B.; Rabolt, J. F. Controlling Surface Morphology of Electrospun Polystyrene Fibers: Effect of Humidity and Molecular Weight in the Electrospinning Process. *Macromolecules* **2004**, *37* (2). https://doi.org/10.1021/ma0351975.

(47) Pelipenko, J.; Kristl, J.; Janković, B.; Baumgartner, S.; Kocbek, P. The Impact of Relative Humidity during Electrospinning on the Morphology and Mechanical Properties of Nanofibers. *Int J Pharm* **2013**, *456* (1). https://doi.org/10.1016/j.ijpharm.2013.07.078.

(48) Baumgarten, P. K. Electrostatic Spinning of Acrylic Microfibers. *J Colloid Interface Sci* **1971**, *36* (1). https://doi.org/10.1016/0021-9797(71)90241-4.

(49) Lannutti, J.; Reneker, D.; Ma, T.; Tomasko, D.; Farson, D. Electrospinning for Tissue Engineering Scaffolds. *Materials Science and Engineering C* **2007**, *27* (3). https://doi.org/10.1016/j.msec.2006.05.019.

(50) Sill, T. J.; von Recum, H. A. Electrospinning: Applications in Drug Delivery and Tissue Engineering. *Biomaterials*. 2008. https://doi.org/10.1016/j.biomaterials.2008.01.011.

(51) Jarusuwannapoom, T.; Hongrojjanawiwat, W.; Jitjaicham, S.; Wannatong, L.; Nithitanakul, M.; Pattamaprom, C.; Koombhongse, P.; Rangkupan, R.; Supaphol, P. Effect of Solvents on Electro-Spinnability of Polystyrene Solutions and Morphological Appearance of Resulting Electrospun Polystyrene Fibers. *Eur Polym J* **2005**, *41* (3). https://doi.org/10.1016/j.eurpolymj.2004.10.010.

(52) Mendes, A. C.; Stephansen, K.; Chronakis, I. S. Electrospinning of Food Proteins and Polysaccharides. *Food Hydrocoll* **2017**, *68*. https://doi.org/10.1016/j.foodhyd.2016.10.022.

(53) Akhmetova, A.; Heinz, A. Electrospinning Proteins for Wound Healing Purposes: Opportunities and Challenges. *Pharmaceutics*. 2021. https://doi.org/10.3390/pharmaceutics13010004.

(54) Juncos Bombin, A. D.; Dunne, N. J.; McCarthy, H. O. Electrospinning of Natural Polymers for the Production of Nanofibres for Wound Healing Applications. *Materials Science and Engineering C*. 2020. https://doi.org/10.1016/j.msec.2020.110994.

(55) Mele, E. Electrospinning of Natural Polymers for Advanced Wound Care: Towards Responsive and Adaptive Dressings. *Journal of Materials Chemistry B*. 2016. https://doi.org/10.1039/c6tb00804f.

(56) Yang, L.; Fitié, C. F. C.; van der Werf, K. O.; Bennink, M. L.; Dijkstra, P. J.; Feijen, J. Mechanical Properties of Single Electrospun Collagen Type I Fibers. *Biomaterials* **2008**, *29* (8). https://doi.org/10.1016/j.biomaterials.2007.10.058.

(57) Zhuo, H.; Hu, J.; Chen, S.; Yeung, L. Preparation of Polyurethane Nanofibers by Electrospinning. *J Appl Polym Sci* **2008**, *109* (1). https://doi.org/10.1002/app.28067.

(58) Ulrich, H. Polyurethanes. In *Encyclopedia of Polymer Science and Technology*; 2003. https://doi.org/10.1002/0471440264.

(59) Burger, C.; Hsiao, B. S.; Chu, B. Nanofibrous Materials and Their Applications. *Annual Review of Materials Research*. 2006. https://doi.org/10.1146/annurev.matsci.36.011205.123537.

(60) Li, C. J.; Li, Y. J.; Wang, J. N.; Cheng, J. PA6@FexOy Nanofibrous Membrane Preparation and Its Strong Cr (VI)-Removal Performance. *Chemical Engineering Journal* **2013**, *220*. https://doi.org/10.1016/j.cej.2013.01.060.

(61) Nasreen, S. A. A. N.; Sundarrajan, S.; Nizar, S. A. S.; Balamurugan, R.; Ramakrishna, S. Advancement in Electrospun Nanofibrous Membranes Modification and Their Application in Water Treatment. *Membranes*. 2013. https://doi.org/10.3390/membranes3040266.

(62) Taha, A. A.; Wu, Y. na; Wang, H.; Li, F. Preparation and Application of Functionalized Cellulose Acetate/Silica Composite Nanofibrous Membrane via

Electrospinning for Cr(VI) Ion Removal from Aqueous Solution. *J Environ Manage* **2012**, *112*. https://doi.org/10.1016/j.jenvman.2012.05.031.

(63) Alharbi, H. F.; Haddad, M. Y.; Aijaz, M. O.; Assaifan, A. K.; Karim, M. R. Electrospun Bilayer PAN/Chitosan Nanofiber Membranes Incorporated with Metal Oxide Nanoparticles for Heavy Metal Ion Adsorption. *Coatings* **2020**, *10* (3). https://doi.org/10.3390/coatings10030285.

(64) Kallem, P.; Gaur, R.; Pandey, R. P.; Hasan, S. W.; Choi, H.; Banat, F. Thin Film Composite Forward Osmosis Membranes Based on Thermally Treated PAN Hydrophilized PVDF Electrospun Nanofiber Substrates for Improved Performance. *J Environ Chem Eng* **2021**, *9* (5). https://doi.org/10.1016/j.jece.2021.106240.

(65) Yoon, B.; Lee, S. Designing Waterproof Breathable Materials Based on Electrospun Nanofibers and Assessing the Performance Characteristics. *Fibers and Polymers* **2011**, *12* (1). https://doi.org/10.1007/s12221-011-0057-9.

(66) Qin, D.; Zhang, R.; Cao, B.; Li, P. Fabrication of High-Performance Composite Membranes Based on Hierarchically Structured Electrospun Nanofiber Substrates for Pervaporation Desalination. *J Memb Sci* **2021**, *638*. https://doi.org/10.1016/j.memsci.2021.119672.

(67) Xu, X.; Chen, Y.; Wan, P.; Gasem, K.; Wang, K.; He, T.; Adidharma, H.; Fan, M. Extraction of Lithium with Functionalized Lithium Ion-Sieves. *Progress in Materials Science*. 2016. https://doi.org/10.1016/j.pmatsci.2016.09.004.

(68) Orooji, Y.; Nezafat, Z.; Nasrollahzadeh, M.; Shafiei, N.; Afsari, M.; Pakzad, K.; Razmjou, A. Recent Advances in Nanomaterial Development for Lithium Ion-Sieving Technologies. *Desalination*. 2022. https://doi.org/10.1016/j.desal.2022.115624.

(69) Commission, E. Critical Raw Materials Resilience: Charting a Path towards Greater Security and Sustainability. In *Critical Raw Materials Resilience: Charting a Path towards greater Security and Sustainability.*; 2020.

(70) Hund, K.; La Porta, D.; Fabregas, T.; Laing, T.; Drexhage, J. Minerals for Climate Action: The Mineral Intensity of the Clean Energy Transition. *World Bank Publications* **2020**.

(71) Zhu, P.; Gastol, D.; Marshall, J.; Sommerville, R.; Goodship, V.; Kendrick, E. A Review of Current Collectors for Lithium-Ion Batteries. *Journal of Power Sources*. 2021. https://doi.org/10.1016/j.jpowsour.2020.229321.

(72) Hannan, M. A.; Hoque, M. M.; Hussain, A.; Yusof, Y.; Ker, P. J. State-of-the-Art and Energy Management System of Lithium-Ion Batteries in Electric Vehicle Applications: Issues and Recommendations. *IEEE Access*. 2018. https://doi.org/10.1109/ACCESS.2018.2817655.

(73) Chagnes, A.; Swiatowska, J. *Lithium Process Chemistry: Resources, Extraction, Batteries, and Recycling*; 2015. https://doi.org/10.1016/C2013-0-19081-2.

(74) Martin, G.; Rentsch, L.; Höck, M.; Bertau, M. Lithium Market Research – Global Supply, Future Demand and Price Development. *Energy Storage Mater* **2017**, *6*. https://doi.org/10.1016/j.ensm.2016.11.004.

(75) Garrett, D. E. *Handbook of Lithium and Natural Calcium Chloride*; 2004. https://doi.org/10.1016/B978-0-12-276152-2.X5035-X.

(76) U.S. Geological Survey. *Mineral Commodity Summaries 2022*; 2022.

(77) Vikström, H.; Davidsson, S.; Höök, M. Lithium Availability and Future Production Outlooks. *Appl Energy* **2013**, *110*. https://doi.org/10.1016/j.apenergy.2013.04.005.

(78) Choubey, P. K.; Kim, M. S.; Srivastava, R. R.; Lee, J. C.; Lee, J. Y. Advance Review on the Exploitation of the Prominent Energy-Storage Element: Lithium. Part I: From Mineral and Brine Resources. *Minerals Engineering*. 2016. https://doi.org/10.1016/j.mineng.2016.01.010.

(79) Munk, L. A.; Hynek, S. A.; Bradley, D. C.; Boutt, D.; Labay, K.; Jochens, H. Lithium Brines: A Global Perspective. In *Rare Earth and Critical Elements in Ore Deposits*; 2016; Vol. 18.

(80) Li, L.; Deshmane, V. G.; Paranthaman, M. P.; Bhave, R.; Moyer, B. A.; Harrison, S. Lithium Recovery from Aqueous Resources and Batteries: A Brief Review. *Johnson Matthey Technology Review*. 2018. https://doi.org/10.1595/205651317X696676.

(81) Liu, X.; Chen, X.; He, L.; Zhao, Z. Study on Extraction of Lithium from Salt Lake Brine by Membrane Electrolysis. *Desalination* **2015**, *376*. https://doi.org/10.1016/j.desal.2015.08.013.

(82) Ji, Z. yong; Chen, Q. bai; Yuan, J. sheng; Liu, J.; Zhao, Y. ying; Feng, W. xian. Preliminary Study on Recovering Lithium from High Mg2+/Li+ Ratio Brines by Electrodialysis. *Sep Purif Technol* **2017**, *172*. https://doi.org/10.1016/j.seppur.2016.08.006.

(83) Cetiner, Z. S.; Doğan, Ö.; Özdilek, G.; Erdoğan, P. Ö. Toward Utilising Geothermal Waters for Cleaner and Sustainable Production: Potential of Li Recovery from Geothermal Brines in Turkey. *International Journal of Global Warming* **2015**, *7* (4), 439. https://doi.org/10.1504/IJGW.2015.070045.

(84) Zhang, Y.; Hu, Y.; Wang, L.; Sun, W. Systematic Review of Lithium Extraction from Salt-Lake Brines via Precipitation Approaches. *Minerals Engineering*. 2019. https://doi.org/10.1016/j.mineng.2019.105868.

(85) An, J. W.; Kang, D. J.; Tran, K. T.; Kim, M. J.; Lim, T.; Tran, T. Recovery of Lithium from Uyuni Salar Brine. *Hydrometallurgy* **2012**, *117–118*. https://doi.org/10.1016/j.hydromet.2012.02.008.

(86) Reich, R.; Slunitschek, K.; Danisi, R. M.; Eiche, E.; Kolb, J. Lithium Extraction Techniques and the Application Potential of Different Sorbents for Lithium Recovery from Brines. *Mineral Processing and Extractive Metallurgy Review*. 2022. https://doi.org/10.1080/08827508.2022.2047041.

(87) Peerawattuk, I.; Bobicki, E. R. Lithium Extraction and Utilization: A Historical Perspective; 2018. https://doi.org/10.1007/978-3-319-95022-8_186.

(88) Flexer, V.; Baspineiro, C. F.; Galli, C. I. Lithium Recovery from Brines: A Vital Raw Material for Green Energies with a Potential Environmental Impact in Its Mining and Processing. *Science of the Total Environment*. 2018. https://doi.org/10.1016/j.scitotenv.2018.05.223.

(89) Epstein, J. A.; Feist, E. M.; Zmora, J.; Marcus, Y. Extraction of Lithium from the Dead Sea. *Hydrometallurgy* **1981**, *6* (3–4). https://doi.org/10.1016/0304-386X(81)90044-X.

(90) Dave, R. H.; Ghosh, P. K. Enrichment of Bromine in Sea-Bittern with Recovery of Other Marine Chemicals. *Ind Eng Chem Res* **2005**, *44* (9). https://doi.org/10.1021/ie049130x.

(91) Yang, H.; Li, B.; Chai, X.; Li, W. Studies on the Interaction Mechanism between Lithium Chloride and Amorphous Al(OH)3. In *Advanced Materials Research*; 2013; Vol. 634–638. https://doi.org/10.4028/www.scientific.net/AMR.634-638.126.

(92) Heidari, N.; Momeni, P. Selective Adsorption of Lithium Ions from Urmia Lake onto Aluminum Hydroxide. *Environ Earth Sci* **2017**, *76* (16). https://doi.org/10.1007/s12665-017-6885-1.

(93) Zhu, S.; Piao, X.; Gou, Z. Extraction of Lithium from Brine with Neutral Organo-Phosphorous Solvents. *Qinghua Daxue Xuebao/Journal of Tsinghua University* **2000**, *40* (10).

(94) Harvianto, G. R.; Kim, S. H.; Ju, C. S. Solvent Extraction and Stripping of Lithium Ion from Aqueous Solution and Its Application to Seawater. *Rare Metals* **2016**, *35* (12). https://doi.org/10.1007/s12598-015-0453-1.

(95) Shi, D.; Cui, B.; Li, L.; Xu, M.; Zhang, Y.; Peng, X.; Zhang, L.; Song, F.; Ji, L. Removal of Calcium and Magnesium from Lithium Concentrated Solution by Solvent Extraction Method Using D2EHPA. *Desalination* **2020**, *479*. https://doi.org/10.1016/j.desal.2019.114306.

(96) Li, X.; Mo, Y.; Qing, W.; Shao, S.; Tang, C. Y.; Li, J. Membrane-Based Technologies for Lithium Recovery from Water Lithium Resources: A Review. *Journal of Membrane Science*. 2019. https://doi.org/10.1016/j.memsci.2019.117317.

(97) Nesterenko, P. N.; Zhukova, O. S.; Shpigun, O. A.; Jones, P. Synthesis and Ion-Exchange Properties of Silica Chemically Modified with Aminophosphonic Acid. *J Chromatogr A* **1998**, *813* (1). https://doi.org/10.1016/S0021-9673(98)00196-4.

(98) Hérès, X.; Blet, V.; Di Natale, P.; Ouaattou, A.; Mazouz, H.; Dhiba, D.; Cuer, F. Selective Extraction of Rare Earth Elements from Phosphoric Acid by Ion Exchange Resins. *Metals (Basel)* **2018**, *8* (9). https://doi.org/10.3390/met8090682.

(99) Chakraborty, R.; Asthana, A.; Singh, A. K.; Jain, B.; Susan, A. B. H. Adsorption of Heavy Metal Ions by Various Low-Cost Adsorbents: A Review. *International Journal of Environmental Analytical Chemistry*. 2022. https://doi.org/10.1080/03067319.2020.1722811.

(100) Quist-Jensen, C. A.; Ali, A.; Drioli, E.; Macedonio, F. Perspectives on Mining from Sea and Other Alternative Strategies for Minerals and Water Recovery – The Development of Novel Membrane Operations. *J Taiwan Inst Chem Eng* **2019**, *94*. https://doi.org/10.1016/j.jtice.2018.02.002.

(101) Yang, G.; Shi, H.; Liu, W.; Xing, W.; Xu, N. Investigation of Mg2+/Li+ Separation by Nanofiltration. *Chin J Chem Eng* **2011**, *19* (4). https://doi.org/10.1016/S1004-9541(11)60026-8.

(102) Wen, X.; Ma, P.; Zhu, C.; He, Q.; Deng, X. Preliminary Study on Recovering Lithium Chloride from Lithium-Containing Waters by Nanofiltration. *Sep Purif Technol* **2006**, *49* (3). https://doi.org/10.1016/j.seppur.2005.10.004.

(103) Gaikwad, R. W.; Gupta, D. V. Review on Removal of Heavy Metals from Acid Mine Drainage. *Applied Ecology and Environmental Research*. 2008. https://doi.org/10.15666/aeer/0603_081098.

(104) Somrani, A.; Hamzaoui, A. H.; Pontie, M. Study on Lithium Separation from Salt Lake Brines by Nanofiltration (NF) and Low Pressure Reverse Osmosis (LPRO). *Desalination* **2013**, *317*. https://doi.org/10.1016/j.desal.2013.03.009.

(105) Song, J. F.; Nghiem, L. D.; Li, X. M.; He, T. Lithium Extraction from Chinese Salt-Lake Brines: Opportunities, Challenges, and Future Outlook. *Environmental Science: Water Research and Technology*. 2017. https://doi.org/10.1039/c7ew00020k.

(106) Sun, S. Y.; Cai, L. J.; Nie, X. Y.; Song, X.; Yu, J. G. Separation of Magnesium and Lithium from Brine Using a Desal Nanofiltration Membrane. *Journal of Water Process Engineering* **2015**, *7*. https://doi.org/10.1016/j.jwpe.2015.06.012.

(107) Nie, X. Y.; Sun, S. Y.; Song, X.; Yu, J. G. Further Investigation into Lithium Recovery from Salt Lake Brines with Different Feed Characteristics by Electrodialysis. *J Memb Sci* **2017**, *530*. https://doi.org/10.1016/j.memsci.2017.02.020.

(108) Zhao, Z.; Si, X.; Liu, X.; He, L.; Liang, X. Li Extraction from High Mg/Li Ratio Brine with LiFePO4/FePO 4 as Electrode Materials. *Hydrometallurgy* **2013**, *133*. https://doi.org/10.1016/j.hydromet.2012.11.013.

(109) El-Baz, A.; Hendy, I.; Dohdoh, A.; Srour, M. Adsorption Technique for Pollutants Removal; Current New Trends and Future Challenges – A Review. *Egyptian Journal for Engineering Sciences and Technology* **2020**, *32* (1). https://doi.org/10.21608/eijest.2020.45536.1015.

(110) Sulyman, M.; Namiesnik, J.; Gierak, A. Low-Cost Adsorbents Derived from Agricultural by-Products/Wastes for Enhancing Contaminant Uptakes from Wastewater: A Review. *Polish Journal of Environmental Studies*. 2017. https://doi.org/10.15244/pjoes/66769.

(111) Ohashi, F.; Tai, Y. Lithium Adsorption from Natural Brine Using Surface-Modified Manganese Oxide Adsorbents. *Mater Lett* **2019**, *251*. https://doi.org/10.1016/j.matlet.2019.05.064.

(112) Marthi, R.; Smith, Y. R. Application and Limitations of a H2TiO3 – Diatomaceous Earth Composite Synthesized from Titania Slag as a Selective Lithium Adsorbent. *Sep Purif Technol* **2021**, *254*. https://doi.org/10.1016/j.seppur.2020.117580.

(113) Julien, C. M.; Mauger, A. Nanostructured MnO2 as Electrode Materials for Energy Storage. *Nanomaterials*. 2017. https://doi.org/10.3390/nano7110396.

(114) Zou, W.; Zhang, J.; Li, K.; Han, P.; Han, R. Characterization of Manganese Oxide and the Adsorption of Copper(II) and Lead(II) Ions from Aqueous Solutions. *Adsorption Science and Technology* **2009**, *27* (6). https://doi.org/10.1260/0263-6174.27.6.549.

(115) Shin, J.; Seo, J. K.; Yaylian, R.; Huang, A.; Meng, Y. S. A Review on Mechanistic Understanding of MnO2 in Aqueous Electrolyte for Electrical Energy Storage Systems. *International Materials Reviews* **2020**, *65* (6). https://doi.org/10.1080/09506608.2019.1653520.

(116) Feng, Q.; Kanoh, H.; Ooi, K. Manganese Oxide Porous Crystals. *Journal of Materials Chemistry*. 1999. https://doi.org/10.1039/a805369c.

(117) Zhang, Q. H.; Li, S. P.; Sun, S. Y.; Yin, X. S.; Yu, J. G. Lithium Selective Adsorption on 1-D MnO2 Nanostructure Ion-Sieve. *Advanced Powder Technology* **2009**, *20* (5). https://doi.org/10.1016/j.apt.2009.02.008.

(118) Zhang, Q. H.; Sun, S.; Li, S.; Jiang, H.; Yu, J. G. Adsorption of Lithium Ions on Novel Nanocrystal MnO2. *Chem Eng Sci* **2007**, *62* (18–20). https://doi.org/10.1016/j.ces.2007.01.016.

(119) Ooi, K.; Miyai, Y.; Katoh, S. Lithium-Ion Sieve Property of ≫-Type Manganese Oxide. *Solvent Extraction and Ion Exchange* **1987**, *5* (3). https://doi.org/10.1080/07366298708918581.

(120) Lei, J. H.; Chen, Y. X.; Gong, Q. X.; Sun, Y. Bin; Zhao, J.; Yuan, Q. H. Preparation of λ-MnO2 by Column Method and Its Ion-Sieve Property. *Journal Wuhan University of Technology, Materials Science Edition* **2002**, *17* (4). https://doi.org/10.1007/bf02838406.

(121) Yang, F.; Chen, S.; Shi, C.; Xue, F.; Zhang, X.; Ju, S.; Xing, W. A Facile Synthesis of Hexagonal Spinel λ-MnO2 Ion-Sieves for Highly Selective Li+ Adsorption. *Processes* **2018**, *6* (5). https://doi.org/10.3390/pr6050059.

(122) He, G.; Zhang, L.; Zhou, D.; Zou, Y.; Wang, F. The Optimal Condition for H2TiO3–Lithium Adsorbent Preparation and Li+ Adsorption Confirmed by an Orthogonal Test Design. *Ionics (Kiel)* **2015**, *21* (8). https://doi.org/10.1007/s11581-015-1393-3.

(123) Zandvakili, S.; Ranjbar, M. Preparation and Characterisation of Lithium Ion Exchange Composite for the Recovery of Lithium from Brine. *Mineral Processing*

and Extractive Metallurgy: Transactions of the Institute of Mining and Metallurgy **2018**, *127* (3). https://doi.org/10.1080/03719553.2017.1334983.

(124) Kanjanapongkul, K.; Wongsasulak, S.; Yoovidhya, T. Investigation and Prevention of Clogging during Electrospinning of Zein Solution. *J Appl Polym Sci* **2010**, *118* (3). https://doi.org/10.1002/app.32499.

(125) Augustine, R.; Kalarikkal, N.; Thomas, S. Clogging-Free Electrospinning of Polycaprolactone Using Acetic Acid/Acetone Mixture. *Polymer - Plastics Technology and Engineering* **2016**, *55* (5). https://doi.org/10.1080/03602559.2015.1036451.

(126) Jun, Z.; Hou, H.; Schaper, A.; Wendorff, J. H.; Greiner, A. Poly-L-Lactide Nanofibers by Electrospinning - Influence of Solution Viscosity and Electrical Conductivity on Fiber Diameter and Fiber Morphology. *E-Polymers* **2003**, *3* (1). https://doi.org/10.1515/epoly.2003.3.1.102.

(127) Wang, T.; Kumar, S. Electrospinning of Polyacrylonitrile Nanofibers. *J Appl Polym Sci* **2006**, *102* (2). https://doi.org/10.1002/app.24123.

(128) Demir, M. M.; Soyal, D.; Ünlü, C.; Kuş, M.; Özçelik, S. Controlling Spontaneous Emission of CdSe Nanoparticles Dispersed in Electrospun Fibers of Polycarbonate Urethane. *Journal of Physical Chemistry C* **2009**, *113* (26). https://doi.org/10.1021/jp903899s.

(129) Terban, M. W.; Seidel, K.; Poselt, E.; Malfois, M.; Baumann, R. P.; Sander, R.; Paulus, D.; Hinrichsen, B.; Dinnebier, R. E. Cross-Examining Polyurethane Nanodomain Formation and Internal Structure. *Macromolecules* **2020**, *53* (20). https://doi.org/10.1021/acs.macromol.0c01557.

(130) Noerochim, L.; Satriawangsa, G. A.; Widodo, A. Recovery of Lithium from Geothermal Fluid at Lumpur Sidoarjo by Adsorption Method. *Journal of Engineering and Technological Sciences* **2016**, *48* (2). https://doi.org/10.5614/j.eng.technol.sci.2016.48.2.6.

(131) Li, L.; Qu, W.; Liu, F.; Zhao, T.; Zhang, X.; Chen, R.; Wu, F. Surface Modification of Spinel λ-MnO 2 and Its Lithium Adsorption Properties from Spent Lithium Ion Batteries. *Appl Surf Sci* **2014**, *315* (1). https://doi.org/10.1016/j.apsusc.2014.07.090.

(132) Zhang, H.; Wu, A.; Fu, H.; Zhang, L.; Liu, H.; Zheng, S.; Wan, H.; Xu, Z. Efficient Removal of Pb(II) Ions Using Manganese Oxides: The Role of Crystal Structure. *RSC Adv* **2017**, *7* (65). https://doi.org/10.1039/c7ra05955h.

(133) Wang, J.; Yang, B.; Lin, X.; Gao, L.; Liu, T.; Lu, Y.; Wang, R. Research of TPU Materials for 3D Printing Aiming at Non-Pneumatic Tires by FDM Method. *Polymers (Basel)* **2020**, *12* (11). https://doi.org/10.3390/polym12112492.

(134) Liu, H.; Huang, W.; Yang, X.; Dai, K.; Zheng, G.; Liu, C.; Shen, C.; Yan, X.; Guo, J.; Guo, Z. Organic Vapor Sensing Behaviors of Conductive Thermoplastic Polyurethane-Graphene Nanocomposites. *J Mater Chem C Mater* **2016**, *4* (20). https://doi.org/10.1039/c6tc00987e.

(135) Yahiaoui, M.; Denape, J.; Paris, J. Y.; Ural, A. G.; Alcalá, N.; Martínez, F. J. Wear Dynamics of a TPU/Steel Contact under Reciprocal Sliding. *Wear* **2014**, *315* (1–2). https://doi.org/10.1016/j.wear.2014.04.005.

(136) Silva, G. G.; Calado, H. D. R.; Musumeci, A. W.; Martens, W.; Waclawik, E. R.; Frost, R. L.; George, G. A. Polymer Nanocomposites Based on P3OT, TPU and SWNT: Preparation and Characterization. In *Proceedings of the 2006 International Conference on Nanoscience and Nanotechnology, ICONN*; 2006. https://doi.org/10.1109/ICONN.2006.340581.

(137) Özmal, F.; Erdoğan, Y. Li+ Adsorption/Desorption Properties of Lithium Ion-Sieves in Aqueous Solution and Recovery of Lithium from Borogypsum. *J Environ Chem Eng* **2015**, *3* (4). https://doi.org/10.1016/j.jece.2015.09.024.

(138) Shi, X.; Zhou, D.; Zhang, Z.; Yu, L.; Xu, H.; Chen, B.; Yang, X. Synthesis and Properties of Li1.6Mn1.6O4 and Its Adsorption Application. *Hydrometallurgy* **2011**, *110* (1–4). https://doi.org/10.1016/j.hydromet.2011.09.004.

(139) Wang, H.; Cui, J.; Li, M.; Guo, Y.; Deng, T.; Yu, X. Selective Recovery of Lithium from Geothermal Water by EGDE Cross-Linked Spherical CTS/LMO. *Chemical Engineering Journal* **2020**, *389*. https://doi.org/10.1016/j.cej.2020.124410.